

1 **The contribution of plasma sheet bubbles to stormtime**
2 **ring current buildup and evolution of the energy**
3 **composition**

4 **A. Sciola¹, V.G. Merkin¹, K. Sorathia¹, M. Gkioulidou¹, S. Bao², F.**
5 **Toffoletto², K. Pham³, D. Lin³, A. Michael¹, M. Wiltberger³, A. Ukhorskiy¹**

6 ¹Johns Hopkins University Applied Physics Laboratory

7 ²Rice University

8 ³NCAR High Altitude Observatory

9 **Key Points:**

- 10 • Global geospace model shows that bubbles contribute at least half of the total ring
11 current energy during the March 17, 2013 storm.
- 12 • The model accurately reproduces the observed ring current intensity and spatial
13 distribution across a broad energy range (10-100 keV).
- 14 • The evolution of the modeled ring current ion energy composition is due to both
15 an evolving source population and energy-dependent losses.

Abstract

The formation of the stormtime ring current is a result of the inward transport and energization of plasma sheet ions. Previous studies have demonstrated that a significant fraction of the total inward plasma sheet transport takes place in the form of bursty bulk flows (BBFs), known theoretically as flux tube entropy-depleted “bubbles.” However, it remains an open question to what extent bubbles contribute to the buildup of the stormtime ring current. Using the Multiscale Atmosphere Geospace Environment (MAGE) Model, we present a case study of the March 17, 2013 storm, including a quantitative analysis of the contribution of plasma transported by bubbles to the ring current. We show that bubbles are responsible for at least 50% of the plasma energy enhancement within $6 R_E$ during this strong geomagnetic storm. The bubbles that penetrate within $6 R_E$ transport energy primarily in the form of enthalpy flux, followed by Poynting flux and relatively little as bulk kinetic flux. Return flows can transport outwards a significant fraction of the plasma energy being transported by inward flows, and therefore must be considered when quantifying the net contribution of bubbles to the energy buildup. Data-model comparison with proton intensities observed by the Van Allen Probes show that the model accurately reproduces both the bulk and spectral properties of the stormtime ring current. The evolution of the ring current energy spectra throughout the modeled storm is driven by both inward transport of an evolving plasma sheet population and by charge exchange with Earth’s geocorona.

Plain Language Summary

The formation of the ring current is one of the defining features of the near-Earth space response to solar storms. While it is known that the plasma that constitutes the ring current originates from Earth’s magnetic tail, the relative roles of different transport mechanisms remains unclear. In this study, we utilize numerical modeling to investigate ring current buildup for a specific solar storm, and find that flows that are medium-scale relative to the system size and referred to as plasma “bubbles”, are responsible for at least half of the total buildup of ring current plasma. Our analysis also shows that the bubbles displace some of the background plasma on their way Earthward, which is important when calculating their net contribution to the ring current. The modeled ring current energy spectrum is in good agreement with spacecraft observations, and the evolution of the energy spectrum is driven by both an evolving plasma population in the tail and by energy-dependent charge exchange. The ability to accurately model the complex interactions between the ring current and Earth’s geospace system is critical for understanding the full impacts of solar storms.

1 Introduction

The formation of the ring current is a defining characteristic of geomagnetic storms (Chapman, 1962; Daglis et al., 1999; M. W. Chen et al., 1997; Jordanova et al., 2020). The ring current is the result of the accumulation of substantial plasma pressure within the inner magnetosphere and as such it is one of the major energy sinks of the solar wind-magnetosphere interaction (Baker, 2008). This dominant stormtime magnetospheric current distorts the global magnetic field greatly, accounting for roughly half of the total stormtime magnetic field disturbance at Earth’s surface (Hamilton et al., 1988; Roeder et al., 1996; N. E. Turner et al., 2001). The gradients of the pressure also drive the Region 2 field-aligned current (FAC) system (Vasyliunas, 1970; Iijima & Potemra, 1976; Ganushkina et al., 2018) which partly controls current closure and convection in the ionosphere, including the shielding of lower latitudes from the high-latitude electric field (Gurnett, 1970; Jaggi & Wolf, 1973; Toffoletto et al., 2003). The energy spectrum of the ring current ions controls their charge exchange with the neutral geocorona (Smith & Bewtra,

1978) which in turn greatly impacts the recovery rate of the storm (Dessler & Parker, 1959; Kistler et al., 1989; Fok et al., 1993; Jordanova et al., 1998).

It is well-accepted that the ring current is created via inward transport of the plasma sheet particles (Liemohn & Khazanov, 2005; Wing et al., 2014; Kistler, 2020). However, to what extent nightside transport at different spatial and temporal scales contributes to ring current buildup remains an outstanding question of magnetospheric physics. Transport by quasi-steady global-scale convection enforced by a dawn-to-dusk electric field that becomes enhanced during storms was proposed originally (Axford, 1969). Erickson and Wolf (1980), however, noted that steady, global convection through the tail would result in unrealistically high pressures in the inner magnetosphere, and hypothesized that time-dependent ejection of excess plasma in the form of substorms could provide a solution to this “pressure crisis.” The model of time-variable but global-scale convection has since been the most widely accepted explanation for stormtime ring current formation (e.g., Daglis, 2006).

However, the existence of a stormtime enhancement in the global-scale cross-tail electric field was challenged by statistical measurements of the electric field in the plasma sheet. It was found from CRRES measurements between 7.5 and 8.5 R_E (Rowland & Wygant, 1998) and Geotail measurements between 5 and 15 R_E (Hori et al., 2005) that the large-scale field remained relatively weak during heightened activity. There were instead many instances of large-amplitude (several to tens of mV/m) electric fields highly fluctuating on minutes-long timescales. Hori et al. (2005) noted that the azimuthal width of the convection channels corresponding to the fluctuating field should be considered, as these enhancements may be caused by narrow-width bursty flows (Angelopoulos et al., 1997). Such “bursty bulk flows” (BBFs; Angelopoulos et al., 1992; Baumjohann, 1990) are indeed estimated to be responsible for a significant amount (>60%) of the total inward transport of magnetic flux and plasma mass and energy transport in the magnetotail (15-22 R_E ; Angelopoulos et al., 1994). BBFs are observed as short-lived (~ 10 s), high-speed (>400 km/s) Earthward flows that typically contain a significant enhancement in magnetic flux, referred to as a “dipolarizing flux bundle” (DFB; Liu et al., 2013), and an enhancement of hot plasma, observed as an injection (Sergeev et al., 2005; Runov et al., 2011; Gabrielse et al., 2012, 2014; Liu et al., 2016). With a cross-tail size of $\lesssim 3 R_E$ (Angelopoulos et al., 1997; Nakamura et al., 2004), they are often referred to as “mesoscale” flows since their scale size is much smaller than the global magnetotail size yet much larger than the kinetic scale. C. X. Chen and Wolf (1993) suggested that BBFs provide an alternative solution to the pressure crisis as described by Erickson and Wolf (1980) if they account for at least 40-55% of the total inward plasma transport in the magnetotail, introducing the possibility that BBFs play a significant role in ring current buildup.

However, BBF transport within the plasma sheet does not directly correspond to contribution to the ring current, since the majority of these flows do not penetrate to within geosynchronous orbit (GEO; Ohtani et al., 2006; Takada et al., 2006). The best predictor of BBF penetration depth is not the flow velocity or magnetic field strength within the structure, but rather the flux tube entropy (FTE; Dubyagin et al., 2011), defined as $S = pV^{5/3}$, where p is the average plasma pressure along the flux tube and $V = \int 1/B ds$ is the flux tube volume (Pontius & Wolf, 1990; Birn et al., 2009). Plasma stability results in a distribution of magnetospheric flux tubes such that the FTE increases with radial distance from the Earth. High-magnetic flux, low-entropy “bubbles” introduced in the magnetotail are interchange unstable and are transported inwards (where they may be observed as BBFs) until they reach a location with comparable background FTE (Pontius & Wolf, 1990; Wolf et al., 2009).

The question of the relative contribution of BBFs/bubbles to stormtime ring current buildup has been notoriously difficult to answer conclusively because of the lack of multipoint measurements with sufficient coverage and resolution. Gkioulidou et al. (2014), using sub-GEO injections observed by the Van Allen Probes (RBSP), estimated that for

118 the 17 March 2013 storm BBFs transported around 30% of the total plasma energy to
 119 the ring current. However, this result required assumptions about the azimuthal distri-
 120 bution of GEO-penetrating injections and the occurrence rate of injections throughout
 121 the storm extrapolated from the number observed by RBSP alone. While observations
 122 from multiple spacecraft somewhat reduce this uncertainty, studies that have utilized large
 123 conjunctions of spacecraft still have difficulty determining whether spacecraft at differ-
 124 ing radial and azimuthal locations are observing the same BBF (e.g., Gabrielse et al.,
 125 2014; D. L. Turner et al., 2017). They also may not be capturing all BBFs that might
 126 be traversing the plasma sheet across different MLTs at any given time. Hence, more com-
 127 plete in situ coverage is required to conclusively address the problem. Energetic neutral
 128 atom (ENA) imaging has recently been used to detect temperature enhancements as-
 129 sociated with BBFs (Keesee et al., 2021) and has the prospect of helping to quantify plasma
 130 energy transported by BBFs with the advantage of observing the entire tail at once. How-
 131 ever, due to low sensitivity of the ENA camera onboard the TWINS spacecraft (due to
 132 a very small geometric factor and duty cycle; McComas et al., 2009), only limited en-
 133 ergies can be used (2–32 keV), assuming a Maxwellian distribution, to retrieve those tem-
 134 peratures.

135 Because of the current observational limitations, numerical modeling has been used
 136 extensively to study inner magnetosphere transport and ring current formation, and has
 137 increasingly found that bubbles play an important role in both cases. Inner magneto-
 138 sphere models that have an outer boundary around 6–9 R_E , and apply a global-scale elec-
 139 tric field there, have found that such convection can build up a ring current and repro-
 140 duce observed trends in Dst (e.g., M. W. Chen et al., 1993; Jordanova et al., 1996; Kozyra
 141 et al., 1998; Ebihara & Ejiri, 2000; Jordanova et al., 2014; Fok et al., 2014). Using the
 142 Rice Convection Model - Equilibrium (RCM-E) with a boundary at GEO, Yang et al.
 143 (2016) showed that driving their simulation with an electric field both with and with-
 144 out the presence of bubbles produced similar ring currents. However, both Yang et al.
 145 (2016) and Lemon et al. (2004) found that when the nightside boundary was instead placed
 146 at 15 R_E , driving their simulation with a strong global-scale electric field produced a pres-
 147 sure enhancement outside of 6 R_E , which prevented further convection inwards and sub-
 148 sequent buildup of the ring current. In both studies, when entropy-depleted bubbles were
 149 introduced along the 15 R_E boundary, a substantial ring current formed, indicating that
 150 the presence of bubbles in the plasma sheet plays a role in ring current buildup. Cramer
 151 et al. (2017), utilizing the Open Geospace General Circulation Model (OpenGGCM) mag-
 152 netohydrodynamic (MHD) code coupled with RCM, found that bubbles were responsi-
 153 ble for 65–85% of the total inward plasma transport to below GEO, depending on storm
 154 intensity. Sorathia et al. (2021), using the stand-alone version of the Grid Agnostic MHD
 155 for Extended Research Application (GAMERA) global MHD model (Zhang et al., 2019;
 156 Sorathia et al., 2020) and test particle tracing (Ukhorskiy et al., 2018; Sorathia et al.,
 157 2018), concluded that Earthward-propagating bubbles in the plasma sheet accounted for
 158 roughly half of the total plasma energy transport while making up only 15% of the plasma
 159 population. The studies by Cramer et al. (2017) and Sorathia et al. (2021) provided quan-
 160 titative evidence of the importance of bubbles in plasma mass and energy transport in
 161 the magnetosphere. However, the contribution of bubbles to the ring current energy con-
 162 tent was not directly examined.

163 The study presented in this paper is the first to quantify the contribution of bub-
 164 bles to the stormtime ring current using a coupled global and inner magnetosphere model.
 165 This work builds off of that of Yang et al. (2015), which investigated this question us-
 166 ing RCM-E and found that up to 60% of the total inner magnetosphere pressure came
 167 from plasma introduced by bubbles along the 15 R_E nightside boundary. We expand on
 168 this topic through use of GAMERA two-way coupled with RCM, which has the advan-
 169 tage of capturing the dynamics of the global system and generating bubbles more self-
 170 consistently. GAMERA, as well as its predecessor, the LFM global MHD model (Lyon
 171 et al., 2004), has a history of accurately reproducing the statistical properties of BBFs

(Wiltberger et al., 2015; Sorathia et al., 2021), and with the addition of RCM coupling is overall well-suited to address this fundamental question of magnetospheric physics.

The goal of understanding ring current buildup must also consider the evolution of its energy composition over time. Observations have found that during quiet times, protons above ~ 100 keV are the dominant contributors to the ring current pressure, while during storms the main contributors to the enhanced pressure are ions with energies between several to tens of keV (e.g., Krimigis et al., 1985; Korth et al., 2000; Zhao et al., 2015; Keika et al., 2018; Gkioulidou et al., 2016). There have been a number of proposed mechanisms for this energy evolution, including the penetration of different plasma sheet populations throughout the storm (Keika et al., 2005; Lui, 1993), adiabatic effects due to localized changes in the magnetic field strength (Lyons, 1977; Lyons & Williams, 1976), radial diffusion (Lyons & Schulz, 1989; Sheldon & Hamilton, 1993; Jordanova & Miyoshi, 2005) and charge exchange (e.g., Kistler et al., 1989; Fok et al., 1993; Jordanova et al., 1998). However, similarly to investigations of bubble contribution to the ring current, the nature of in situ observations makes it challenging to make conclusive statements about which processes are ultimately responsible for the observed evolution. Reproducing this behavior in first-principle geospace models is necessary in order to self-consistently model the ring current's coupling with the ionosphere and exosphere, and as a result more accurately capture the recovery phase. In turn, such model capabilities help to inform to what extent certain processes influence the evolution of the energy spectra during storms.

In this study, we present a comprehensive picture of the contribution of bubbles to the buildup of the stormtime ring current, investigate the evolution of the ring current energy spectra throughout the storm, and examine the contributors to this evolution. This is done via a case study of the March 17th, 2013 geomagnetic storm simulated with the Multiscale Atmosphere-Geospace Environment (MAGE) model, which includes two-way coupling between GAMERA and RCM. Section 2 provides an overview of the storm, the numerical model, and the data used for data-model comparisons. Section 3 presents our results, including a quantitative analysis of BBF/bubble contribution to the inner magnetosphere energy content, data-model comparison of proton intensities, and an analysis of the contributors to the evolving ring current energy spectra. In section 4, we discuss the findings and caveats of the study, and in section 5 we present our conclusions.

2 Methodology

2.1 Event Description

For this study we simulate the March 17th 2013 storm, one of the major storms of the Van Allen Probes era. This storm was caused by a coronal mass ejection (CME), and had the sudden storm commencement (SSC) at about 06:00 UT on 03/17/2013 and a minimum Dst of approximately -140 nT. In this study we begin the simulation at 00:00 UT that day and, since we are focusing on ring current buildup, we only examine main phase out to 19:00 UT, which saw a minimum Dst of about -100 nT (see the Sym-H panel in Figure 1). Additional solar wind parameters are provided in Supplemental Figure 1. This storm featured many injections observed by the Van Allen Probes within geosynchronous orbit (Gkioulidou et al., 2014), providing an ideal opportunity to study the role of injections in the buildup of Earth's stormtime ring current. This storm has been studied extensively, including modeling (e.g., Yu et al., 2014, 2015; Raeder et al., 2016; Wiltberger et al., 2017; M. W. Chen et al., 2019; Lin et al., 2021) and observational studies (e.g., Gkioulidou et al., 2014; Lyons et al., 2016; Tang et al., 2016; Yue et al., 2016; Menz et al., 2017; Dang et al., 2019).

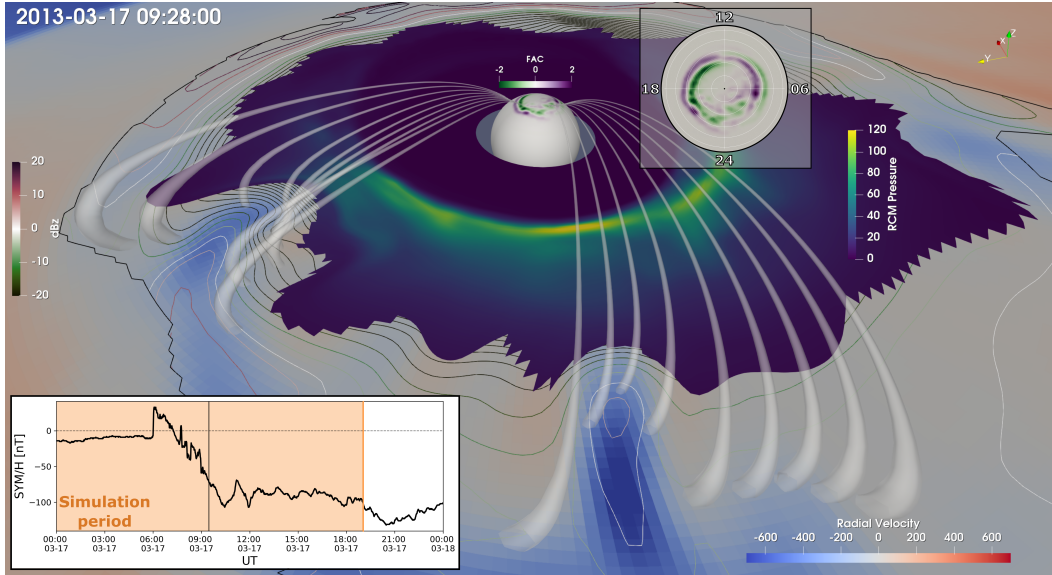


Figure 1. 3D view of the simulation at 09:28 UT. The radial velocity is shown as red and blue color contours in the equatorial plane. On the same surface, ΔB_z is shown as colored contour lines in 5 nT intervals, and the open/closed field boundary is shown as a black line. Overplotted in the equatorial plane is the RCM pressure within the RCM active domain. Field lines, seeded along constant latitudes near Earth, are shown as translucent tubes, with a cross-section scaled by $|B|^{-1}$. The field lines terminate at the GAMERA inner boundary at $2 R_E$. On the Earth's surface, downward and upward ionospheric field-aligned currents (FACs) are shown as purple and green color contours, respectively. Overlaid to the right of the Earth is another view of the northern ionosphere FACs from a perspective along SM-Z. Overlaid in the bottom left is a timeseries of the observed Sym-H, where the period of the storm that is simulated is shaded in orange, and the black vertical line is 09:28 UT, the time shown in the 3D view.

220

2.2 Data

221

222

223

224

225

The solar wind data source is primarily Modified High Resolution OMNI (HRO) data. For this time period, the HRO data is based on ACE observations, which contains a 45 minute data gap around the SSC. We fill any 5-minute or longer data gaps with the propagated and KP-despiked Wind dataset available on OMNIWeb. This method produces a significantly sharper SSC than interpolating across the 45-minute data gap.

226

227

228

229

230

231

232

233

234

235

236

237

Proton data from the RBSPICE instrument aboard Van Allen Probe B (RBSP-B) is used for comparison with our model. During this storm, the RBSPICE instrument aboard Probe A was not fully operational and so its data is not used here. Because spacecraft charging can lead to bad data below 10 keV (Menz et al., 2017), we choose this as our lower energy limit. We choose an upper limit of 200 keV as this is about the maximum energy in this simulation that our inner magnetosphere model (see section 2.3) covers throughout the entirety of the RBSP-B orbit. This energy range is fully covered using the combination of the Time-of-Flight by Pulse Height (TOFxPH) data product for proton energies between 10-50 keV and the Time-of-flight by Energy (TOFxE) data product for 50 keV protons and upwards (Mitchell et al., 2013). The Level-3 omnidirectional flux data product from both of these instruments was used. This data was retrieved from cdaweb (<https://cdaweb.gsfc.nasa.gov>) via the cdasws python package (<https://pypi.org/project/cdasws/>).

238

2.3 Model Description

239

240

241

242

243

244

245

246

247

248

249

250

251

252

253

254

255

256

257

258

The Multiscale Atmosphere-Geospace Environment (MAGE) model, developed at the NASA DRIVE Science Center for Geospace Storms, is a coupled geospace model designed to enable the investigation of multiscale phenomena, from the global magnetosphere to the ionosphere and thermosphere, during geomagnetic storms. A visual overview of the simulation at 09:28 UT on 03/17/2013 is given in Figure 1 which highlights the components of MAGE used in this study. The primary physics module is the Grid Agnostic MHD for Extended Research Application (GAMERA) 3D global MHD model (Zhang et al., 2019; Sorathia et al., 2020). GAMERA is a reinvention of the well-known LFM model (Lyon et al., 2004), preserving the original high-order, non-diffusive numerics. Minimizing numerical diffusion between the low-entropy bubble with the surrounding background plasma is critical, as this enables better representation of the bubble penetration depth. GAMERA is coupled with the REMIX ionospheric potential solver, which is a rewrite of the Magnetosphere-Ionosphere Coupler/Solver (MIX) model (Merkin & Lyon, 2010). GAMERA and REMIX are also two-way coupled with the Rice Convection Model (RCM), a flux tube-averaged inner magnetosphere model that resolves energy-dependent gradient-curvature drifts (Toffoletto et al., 2003; Wolf et al., 2016). The GAMERA inner boundary for this simulation is at a radius of $2 R_E$, where field-aligned currents (FACs) and the ionospheric electric fields are mapped to/from the ionosphere using a dipole field. Self-consistently calculated mono-energetic and diffuse electron precipitation is included in the calculation of ionospheric conductance (Lin et al., 2021).

259

260

261

262

263

264

265

266

267

268

269

270

271

272

There is a “spin-up” phase, lasting several hours, where only GAMERA and REMIX are advanced using the solar wind conditions at time $T=0$ (00:00 UT on 03/17/2013, in this case), with the interplanetary magnetic field (IMF) set to zero, as a constant driver. At $T=0$, the full solar wind time-series is used, and the RCM starter ring current is initialized using an analytic pressure distribution described in Liemohn (2003), specifically the L-dependent profile in the nominal case where the pressure peak is centered at $L=4$ and $\Delta L=0.625$. The pressure distribution is scaled such that its total contribution to the Dst , as calculated via the DPS- Dst relation, makes up the difference between the observed Dst and that calculated by GAMERA at $T=0$. An ad-hoc temperature of 30 keV is used in combination with the pressure profile to calculate the density profile, assuming a Maxwellian distribution. Beyond $10 R_E$, the plasma sheet is initialized using the empirical model described in Tsyganenko and Mukai (2003). For the solar wind conditions preceding this storm, this resulted in an average plasma sheet temperature of around 10 keV.

273

274

275

276

277

278

279

280

281

282

283

284

285

286

287

288

289

290

The coupling between GAMERA and RCM enables the model to resolve energy-dependent drifts, precipitation, and charge exchange within the inner magnetosphere. The high-level coupling procedure is similar to that implemented in LFM-RCM (Pembroke et al., 2012), with several important improvements. In LFM-RCM, the active RCM domain was not only confined to the region of closed field lines, but also first to an ellipse that encompassed as much of the closed domain as possible, and was further confined to regions where the plasma $\beta \leq 1$. This ensured the active domain was limited to regions that were magnetically dominated, consistent with the assumptions within RCM. The plasma β limiter was introduced to exclude fast flows, which may break the validity of the flux-tube averaged approximations. In GAMERA-RCM, the ellipse is more conservatively confined to be no closer than 4 radial grid cells to the open/closed boundary, and is further confined to regions where the Alfvén speed is sufficiently fast to communicate information along the field line relative to its evolution time-scale, such that the field-line averaged approximation is reasonably valid. We found this limiting of the active RCM domain to be more effective in excluding fast flows. Its implications in the context of the trapping/leaking of plasma from bubbles are discussed in section 4. For this study, the MHD density and pressure are mapped to RCM energy invariant channels along its outer boundary via a Kappa distribution, defined as in Eq. 3.12 of Livadiotis

291 and McComas (2013), with a kappa value of 6. This resulted in better agreement between
 292 the simulated and observed proton intensities compared to mapping using a Maxwellian
 293 distribution. A dynamic plasmasphere is also modeled via a zero-energy channel in RCM.
 294 This channel is initialized using the Kp-dependent plasmasphere model given in Gallagher
 295 et al. (2000) and evolves self-consistently using the combined electrostatic potential from
 296 REMIX and corotation. Energy-dependent charge exchange losses are applied to the RCM
 297 protons using the empirical geocorona density profile from Østgaard et al. (2003) and
 298 cross-sections provided by Lindsay and Stebbings (2005). At each coupling time step (ev-
 299 ery 15s) the plasma moments from the RCM hot plasma and plasmasphere channels are
 300 ingested by GAMERA as a single fluid.

301 3 Results

302 3.1 Simulation Overview

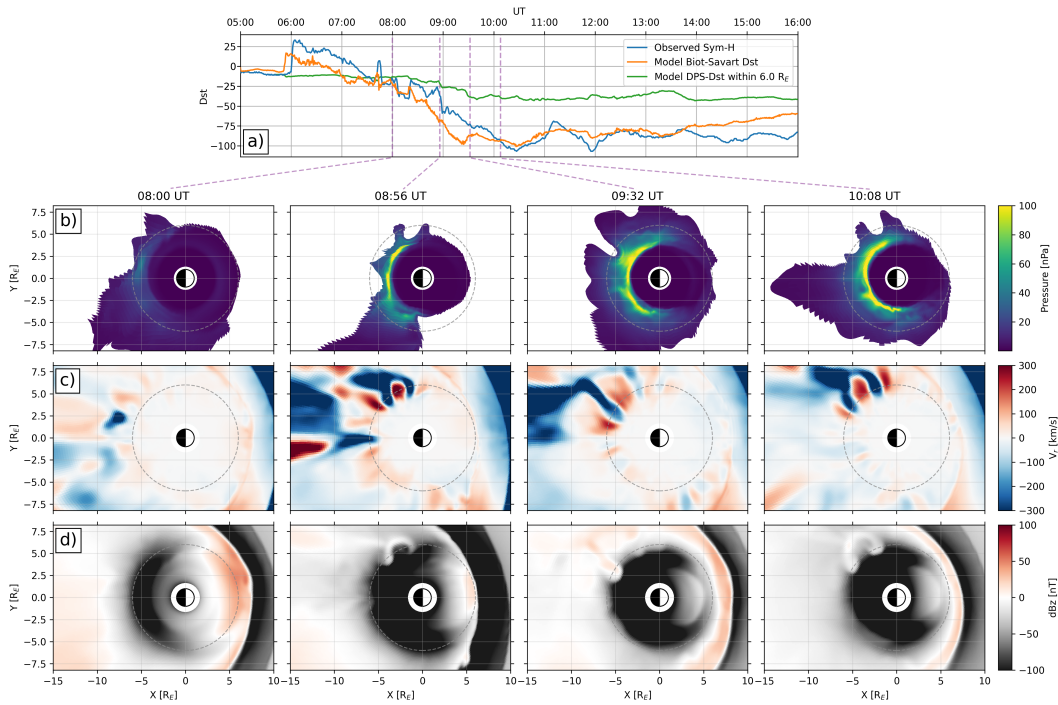


Figure 2. (a) Time-series of the observed Sym-H, the simulation Dst calculated using Biot-Savart evaluated at the center of Earth, and the DPS-*Dst* for all closed field lines within 6 R_E. Equatorial view of the inner magnetosphere pressure (row b), v_r (row c), and ΔB_z (row d) at four select times corresponding to the purple dashed lines in (a). The gray dashed circle with a radius of 6 R_E is included for reference.

303 Figure 2a shows, in addition to the observed and simulated *Dst* values, the Dessler-
 304 Parker-Sckopke *Dst* (DPS-*Dst*; Dessler and Parker (1959); Sckopke (1966)) evaluated
 305 for all closed field lines with an equatorial extent within 6 R_E. The DPS relation, as-
 306 suming a dipole field, relates the total plasma energy within a defined volume (*E*) with
 307 the magnetic perturbation it causes at Earth's surface (ΔB_z), given by

$$\frac{\Delta B_z}{B_0} = -\frac{2E}{E_m} \quad (1)$$

308 where B_0 is Earth's surface magnetic field and E_m is the total energy of the magnetic
 309 field external to the Earth. Thus, a decrease in the plotted DPS- Dst directly corresponds
 310 to the increase in plasma energy within $6 R_E$. It can be seen in Figure 2a that the DPS-
 311 Dst stays relatively constant through the SSC, then decreases at a fairly steady rate start-
 312 ing around 8:30 UT, and then levels off again around 9:30 UT and reaches its absolute
 313 minimum around 10:30 UT. Therefore most of the ring current buildup in this simula-
 314 tion occurred within just two hours (08:30-10:30 UT). The DPS- Dst is roughly half the
 315 value of the total simulated Dst , in agreement with the estimates of Hamilton et al. (1988)
 316 and N. E. Turner et al. (2001).

317 The plots in Figure 2b show the plasma pressure within the inner magnetosphere
 318 in the equatorial plane, as calculated by RCM, for 4 times between 8:00-10:08 UT. The
 319 (c) and (d) rows show the radial velocity (V_r) and vertical component of the magnetic
 320 field with the dipole subtracted out (ΔB_z) from GAMERA. Evident in the V_r panels are
 321 highly localized inward flow bursts (FBs), which are accompanied by dipolarizations (DFBs,
 322 visible in the ΔB_z panels) and particle flux enhancements (not shown). Per the coupling
 323 algorithm described in section 2.3, the RCM domain does not include the region con-
 324 taining these structures until the fast flow has subsided, causing the finger-like incursions
 325 of the outer boundary on the RCM active domain (row b).

326 The ring current pressure reaches a peak of 140 nPa around 9:15 UT and is located
 327 at a radial distance of just under $4 R_E$. Over time, the pressure peak is smeared out az-
 328 imuthally as plasmas of different energies gradient-curvature drift at varying velocities.
 329 However, the total plasma energy within the inner magnetosphere remains fairly con-
 330 stant, as indicated by the DPS- Dst curve in Figure 2a.

331 Within MHD, the change in total plasma energy within a volume enclosed by a sur-
 332 face is given by the enthalpy flux through that surface (Birn & Hesse, 2005). Figure 3
 333 presents a keogram-like view of several quantities evaluated along a 180° arc across the
 334 nightside with a radius of $6 R_E$ from the origin at Earth. Figure 3a shows the radial com-
 335 ponent of the enthalpy flux (H) perpendicular to the magnetic field direction, defined
 336 as

$$(H_\perp)_r = 5/2p(\mathbf{v}_\perp)_r \quad (2)$$

337 where p is the plasma pressure and $\mathbf{v}_{\perp,r}$ is the radial component of the bulk velocity per-
 338 pendicular to the magnetic field vector. We denote inward/Earthward flux as positive,
 339 so that it corresponds to an increase in the plasma energy within $6 R_E$. The structure
 340 of the inward enthalpy flux is highly localized in MLT extent. Keeping in mind that at
 341 $6 R_E$, an arc spanning 1 MLT is roughly $1.6 R_E$ in length, the azimuthal extent of these
 342 flows are similar to the scale-size of BBFs observed further in the plasma sheet (15-19
 343 R_E ; Nakamura et al., 2004). Nearly each instance of enhanced inward enthalpy flux is
 344 accompanied by magnetic dipolarizations (Fig. 3b) and a depletion in flux tube entropy
 345 (Fig. 3c), indicating that these flows are indeed bubbles penetrating below $6 R_E$. There
 346 are several notable exceptions in the 03-06 MLT range between 10:00 and 10:30 UT where
 347 the entropy instead appears to increase with the arrival of the enhanced enthalpy flux.
 348 These features are indicators of bubbles that did not reach $6 R_E$ before reaching their
 349 equilibrium position, but compressed the magnetic flux Earthward of them, increasing
 350 the concentration of magnetic flux and pushing higher-entropy flux tubes to a lower L
 351 shell.

352 The bubbles in Figure 3 originate from the middle to distant plasma sheet and prop-
 353 agate to below GEO. Indeed, Figure 4 visualizes the flows associated with several bub-
 354 ble features during the 09:27:00 - 09:31:30 UT period. The figure shows several spher-
 355 ical slices through the magnetotail, centered in Z on the equatorial plane, with the ra-
 356 dial component of the bulk flow perpendicular to the magnetic field ($v_{\perp,r}$) displayed as
 357 color contours on each. The inner slice has a radius of $6 R_E$, equal to that of the night-
 358 side arc shown in Figure 3. While not shown in the figure, field lines have been traced

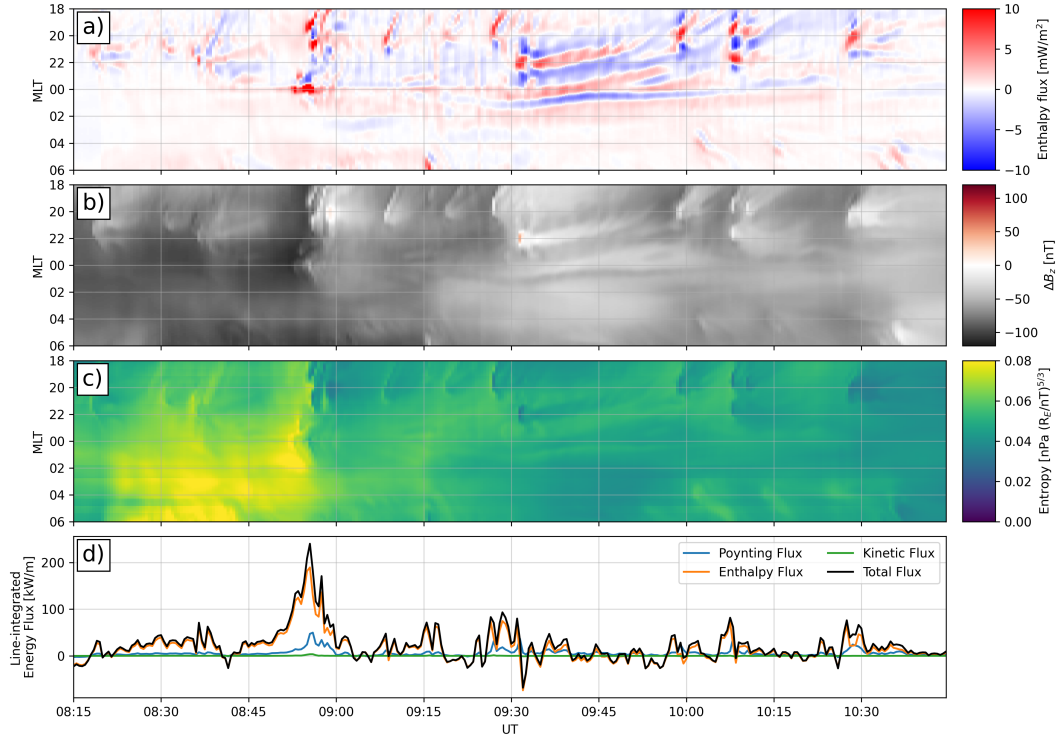


Figure 3. Simulated quantities evaluated along a 180° arc across the nightside with a radius of $6 R_E$, including: (a) The radial component of the enthalpy flux, (b) ΔB_z , and (c) flux tube entropy. In the enthalpy flux panel, positive values indicate radially inward flux, and negative values indicate radially outward flux. (d) Line-integral of the radial component of the enthalpy, Poynting, bulk kinetic, and total energy flux across the entire arc.

359 from each grid point at each point in time, so the magnetic topology of the domain is
 360 known. Regions of each slice that are connected to non-closed field lines (i.e. open or IMF
 361 lines) have been darkened to convey the 3D topology and help to visualize the stretch-
 362 ing of the tail. An animation of this figure is provided in Supplemental Video 1. Figure
 363 4a shows a snapshot at 09:27 UT, where it can be seen on the furthest 2 slices, at 12 and
 364 $14 R_E$, that the tail is stretched and that fast flows are emerging within the current sheet.
 365 A large flow burst has an origin beyond $14 R_E$ and penetrates through the $6 R_E$ slice;
 366 this corresponds to the bubble feature shown in Figure 3 at 20 MLT at the same time.
 367 We note here that in this snapshot it may appear that there is a single large-scale in-
 368 ward flow spanning roughly 21-24 MLT at $12 R_E$, however it is clearer in Supplemental
 369 Video 1 that these are two distinct inward flows. Return flows can also be seen on
 370 either side of the most duskward bubble, spanning at least $2 R_E$ in radial extent. In Fig-
 371 ure 4b, a flow burst that does not penetrate $6 R_E$ is highlighted. Figure 4c shows the
 372 strongest flow/bubble captured by the simulation, which reached $6 R_E$ around 09:31 UT
 373 and also generated strong return flows. The shaded regions behind the flow's origin sug-
 374 gest this bubble was initiated by reconnection inside of $14 R_E$. This example demonstrates
 375 that not all bubbles in the simulation propagate in from the more distant central plasma
 376 sheet, and that they may not all be strictly BBFs by definition (Angelopoulos et al., 1992,
 377 which observed them between 9-19 R_E), but this is a byproduct of the strong storm con-
 378 ditions limiting the closed tail region within relatively close distances to Earth. In order
 379 to avoid any confusion due to terminology, going forward we will refer to these struc-
 380 tures simply as bubbles, with the understanding that they all possess an inward flow,

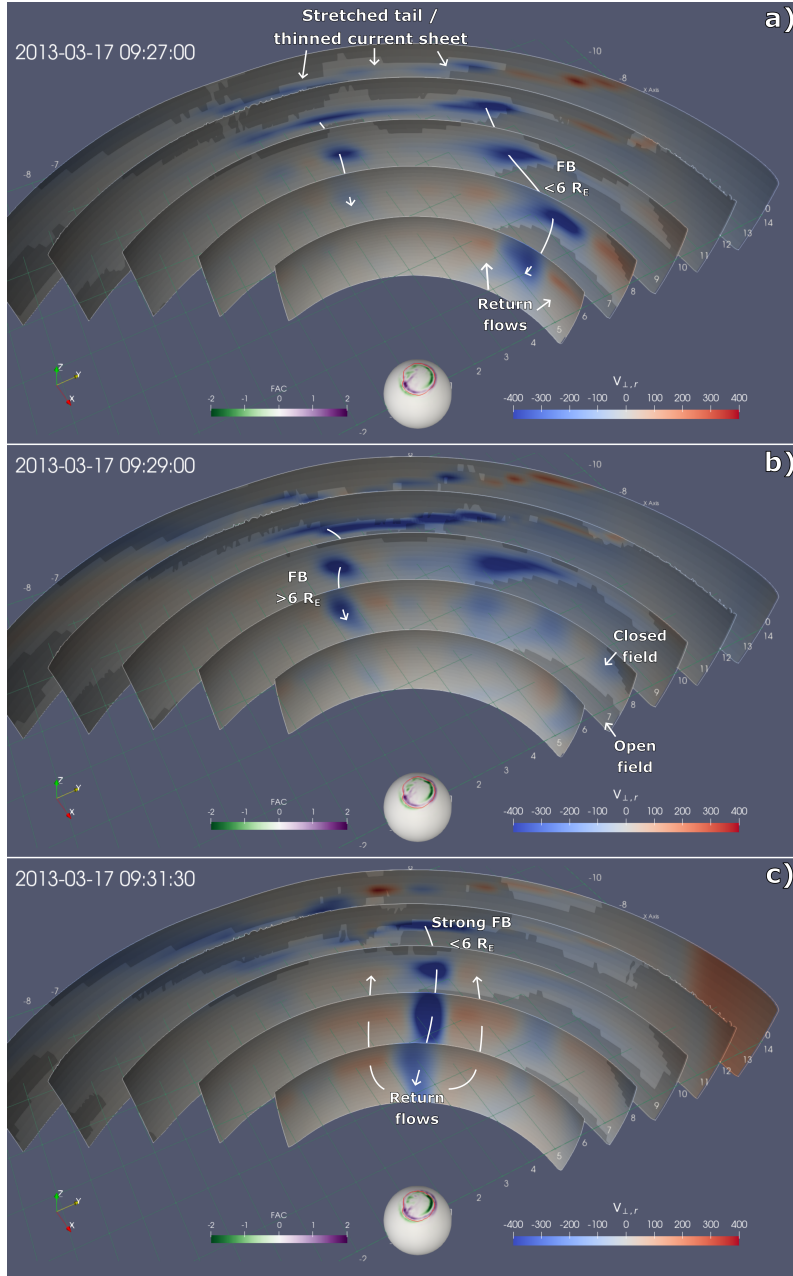


Figure 4. Spherical slices through the MHD solution of the dusk-to-midnight sector at three select times spanning 4.5 minutes. The slices span $6\text{--}14 R_E$, spaced $2 R_E$ apart, and are centered in Z on the XY -plane. The color contours on the slices show the radial component of the bulk velocity perpendicular to the magnetic field ($v_{\perp,r}$). The darker regions on the slices denote regions that are on non-closed field lines (either open or fully IMF field). Each panel is marked to show flow paths through the slices. Flow vectors have been included in the animated version of this figure (see Supplemental Video 1). The Earth is also shown, with the inward/outward field-aligned currents shown in purple and green, respectively. The red line in the ionosphere marks the open-closed boundary determined via field line tracing.

381 transport of plasma mass and energy as well as dipolarizing flux, and have a lower flux
 382 tube entropy relative to the local background, as shown in Figure 3.

383 Tailward vortical flows are observed on either side of almost every Earthward flow.
 384 Since the sign of the enthalpy flux is indicative of the flow direction, the return flows are
 385 evident from the regions of negative flux shown in Figure 3a. Such tailward flows have
 386 been identified previously in both numerical models (Birn et al., 2011; Merkin et al., 2019;
 387 Yang et al., 2019) and observationally (Panov et al., 2010). These tailward flows clearly
 388 transport a significant amount of plasma energy outwards and thus must be considered
 389 when quantifying the net contribution of bubbles to the buildup of the ring current en-
 390 ergy, as is done in section 3.2.

391 Fig. 3d shows a time-series of the radial component of the enthalpy, Poynting and
 392 kinetic flux, as well as their sum, integrated along the nightside arc. The Poynting flux
 393 in this panel is defined as $\mu_0^{-1}(\mathbf{v}_\perp \times \mathbf{B}) \times \mathbf{B}$, and the kinetic flux as $1/2\rho v^2 \mathbf{v}_\perp$. It can
 394 be qualitatively seen that enhancements in the total energy flux correlate well with the
 395 timing of bubbles passing through the arc (a more quantitative analysis follows in sec-
 396 tion 3.2). The enhancements in enthalpy flux are always accompanied by enhancements
 397 in the transported magnetic flux. However, the flows that reach $6 R_E$ transport energy
 398 largely in the form of plasma energy rather than magnetic or bulk kinetic energy.

399 A prominent feature in the enthalpy flux panel is the standing structure of mul-
 400 tiple inward/outward flows between 09:30 and 10:00 UT. The structure is initiated by
 401 the previously-examined strong flow that arrives at 22 MLT, which kicks off a standing
 402 vortical pattern across several MLT that slowly drifts westward. The vortices are local-
 403 ized to just a couple of R_E in the radial direction and do not contribute to continuous
 404 pumping of new energy from the tail. While this is an interesting feature, because it does
 405 not contribute to the net transport of plasma (seen more quantitatively later in Fig. 5),
 406 we do not investigate it further as a part of this study.

407 3.2 Quantification of Plasma Energy Transport to the Ring Current

408 In order to quantify the contribution of bubbles to the buildup of the ring current
 409 energy content, we first construct a simple method of systematically detecting them. We
 410 define the quantity ΔB_τ , which is calculated by subtracting the average B_z value for the
 411 preceding τ minutes from the instantaneous B_z value:

$$\Delta B_\tau(l, t) = B(l, t) - \frac{1}{\tau} \int_{t-\tau}^t B(l, t') dt' \quad (3)$$

412 where τ is a chosen time interval and l is the azimuthal position along the nightside arc.
 413 With a τ on the order of minutes, this metric effectively picks out rapid enhancements
 414 of the magnetic field strength while filtering out longer timescale variations due to global
 415 dipolarization events. At the same time, this method also performs better at identify-
 416 ing dipolarization fronts than selection via a dB_z/dt threshold, as the latter is more sus-
 417 ceptible to fluctuations in B_z that are not associated with bubbles. We find that the com-
 418 bined criteria of $\Delta B_\tau > 10$ nT with $\tau = 2$ minutes and $V_r < 0$ (i.e. inward radial ve-
 419 locity), similar to the criteria used by Runov et al. (2021) to identify many dipolariza-
 420 tion events within THEMIS observations, performs well in systematically selecting bub-
 421 bles along the $6 R_E$ arc within our simulation. For every point that meets this criteria,
 422 we also flag all points within $l \pm 1 R_E$ arc-length of the point as being caused by bubbles
 423 in order to account for the return flows brought on by the Earthward flow. Because we
 424 are triggering off of enhancements in B_z , we also extend this flagged area out to 1 minute
 425 before the time of the triggered feature in order to include any enthalpy flux enhance-
 426 ments due to compression ahead of the bubble.

427 The black boxed regions in Figure 5a mark the regions selected as being influenced
 428 by bubbles given the above criteria, overplotted on the enthalpy flux keogram identical

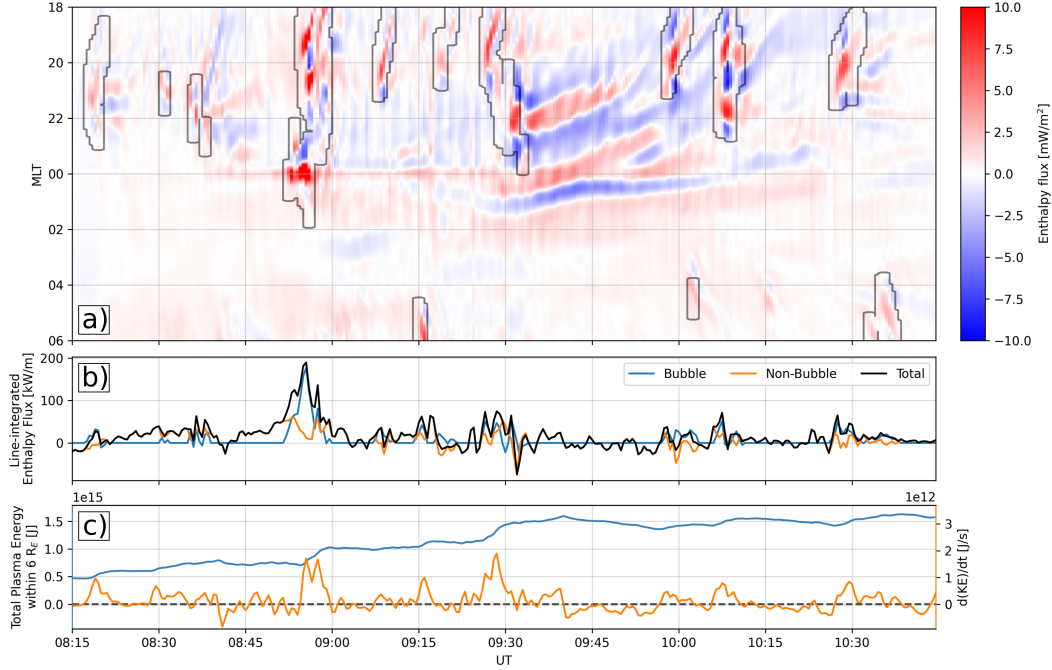


Figure 5. Time-series analysis of energy flux through a 180° arc across the nightside hemisphere at $6 R_E$: (a) Radial component of the enthalpy flux through the nightside arc, the same as in Fig. 3a. Black boxes outline the regions determined to contain bubbles; (b) Line-integrated enthalpy flux from bubbles, outside of bubbles, and in total; (c) The instantaneous value (blue line) and time-derivative (orange line) of the total plasma energy contained on all closed flux tubes within $6 R_E$.

429 to that in Figure 3a. This algorithm successfully picks out the most obvious instances
 430 of bubbles and their accompanying return flows. It is also made clearer here that a bub-
 431 ble at 09:30 UT and 22 MLT initiated the standing vortical structure, and that the stand-
 432 ing structure is not a result of a continuous flow from the tail. In Figure 5b is the line
 433 intergral of the enthalpy flux within regions flagged as being caused by bubbles vs. those
 434 that were not. Interestingly, while there are several bubbles throughout the initial peri-
 435 od between 08:15-08:45 UT, inward plasma energy transport occurred mostly outside
 436 of these flows. There is even a surge of large-scale transport starting at 8:44 UT that leads
 437 to the greatest enthalpy flux enhancement at 08:55 UT. At this point, however, several
 438 bubbles arrive at $6 R_E$ simultaneously and are the major contributors to this enhance-
 439 ment. Beyond this period, there are many instances where net inward flux is dominated
 440 by mesoscale flows rather than by global-scale convection. We also note here that trans-
 441 port outside of bubbles is not uniformly inward across the tail.

442 Fig. 5c shows the value (blue) and time derivative (orange) of the total plasma energy
 443 on all closed field lines within $6 R_E$ across all MLTs. The greatest peaks in the time
 444 derivative correlate well with the peaks in net enthalpy flux 5b), indicating that the flows
 445 through the nightside arc are the main contributors to the increase of plasma energy within
 446 $6 R_E$, and thus the buildup of the ring current.

447 Separately summing up the net enthalpy flux within and outside of the boxed re-
 448 gions throughout the primary period of ring current buildup in the model (08:15-10:45
 449 UT), we find that 50% of the net inward enthalpy flux through the $6 R_E$ arc is caused
 450 by bubbles. We emphasize here that this is not the same as saying “bubbles contribute

50% of the total plasma energy to the ring current," as this analysis is only quantifying bubbles that penetrated as deeply as $6 R_E$. Excluded from this calculation is the consideration of plasma that ultimately made it to below $6 R_E$, but was only transported part of the way by bubbles. In other words, the 50% estimate serves as a lower bound on the total contribution of bubbles to the ring current energy for this simulated storm. This point is discussed in further detail in section 4.

This result is not directly comparable to, but complements, those in Cramer et al. (2017). Firstly, Cramer et al. (2017) quantified the number density flux whereas we are examining the transport of plasma energy, which is more directly linked to the ring current pressure. Secondly, Cramer et al. (2017) examined only the inward flux, and therefore did not account for the net transport due to return flows. In the presented simulation, for all of the plasma energy transported inwards by BBFs through the nightside arc, the return flows transported, on average, 40% of that amount outwards. Therefore we also conclude that the effects of return flows must be accounted for when quantifying the net contribution of bubbles to ring current buildup. However, we emphasize that this fraction was derived from this specific storm simulation, and should not be interpreted as a statement about the effect of return flows in general.

3.3 Evolution of the Ring Current Energy Spectra

We have considered, above, the processes that contribute to the buildup of the ring current through nightside transport. However, a deeper understanding of the stormtime ring current requires also an understanding of the buildup and evolution of the constituent particles across a broad range of energies. In this section we present an analysis of the proton energy spectra within the ring current region, beginning with a data-model comparison between the RCM proton intensities and that observed by RBSP-B, with the purpose of providing an in-depth understanding of which physical processes the model is accurately reproducing and those it is not. This is followed by an analysis of the evolution of the simulated proton energy spectra and the drivers of this evolution, including contribution from the source population, localized adiabatic heating, and losses due to charge exchange.

3.3.1 Data-Model Comparison: Proton Intensities

In this section, the proton intensities as observed by RBSP-B and calculated by the model are compared along the satellite trajectory. This is presented in Figures 6 and 7. Figure 6 shows the comparison for ten energies between 10 and 100 keV, the energy range that constitutes the majority of the ring current pressure (Smith & Hoffman, 1973; Williams, 1985; Krimigis et al., 1985). Note that the range of the vertical axes of each panel are different in order to better resolve the comparison for each plot. A 5-minute smoothing window has been applied to the RCM intensities to remove noise. The comparison begins when RBSP-B is at apogee of the orbit during which the SSC occurs. We refer to this orbit as Orbit 1, and the following orbits as Orbits 2 and 3. Included in Figure 6 are annotations denoting the phase of the orbit and azimuthal location of the spacecraft at that time. Figure 7a,b shows a comparison of the observed and simulated proton intensities for the continuous energy spectra between 10 and 200 keV. Figure 7c is a *Dst* plot equivalent to that in Figure 1a. Figure 7d shows the RCM pressure in the equatorial plane, as well as the spacecraft trajectory over the duration of the simulation, and its current location at 10:09 UT. Note that the trajectory is not a perfectly elliptic orbit; this is because the trajectory is represented by the spacecraft's 3D position mapped to the equator along the field lines traced through the model magnetic field. Vertical lines in the other panels correspond to the time shown in the top right corner of the Figure 7d. This figure is a snapshot of the animation provided as Supplemental Video 2.

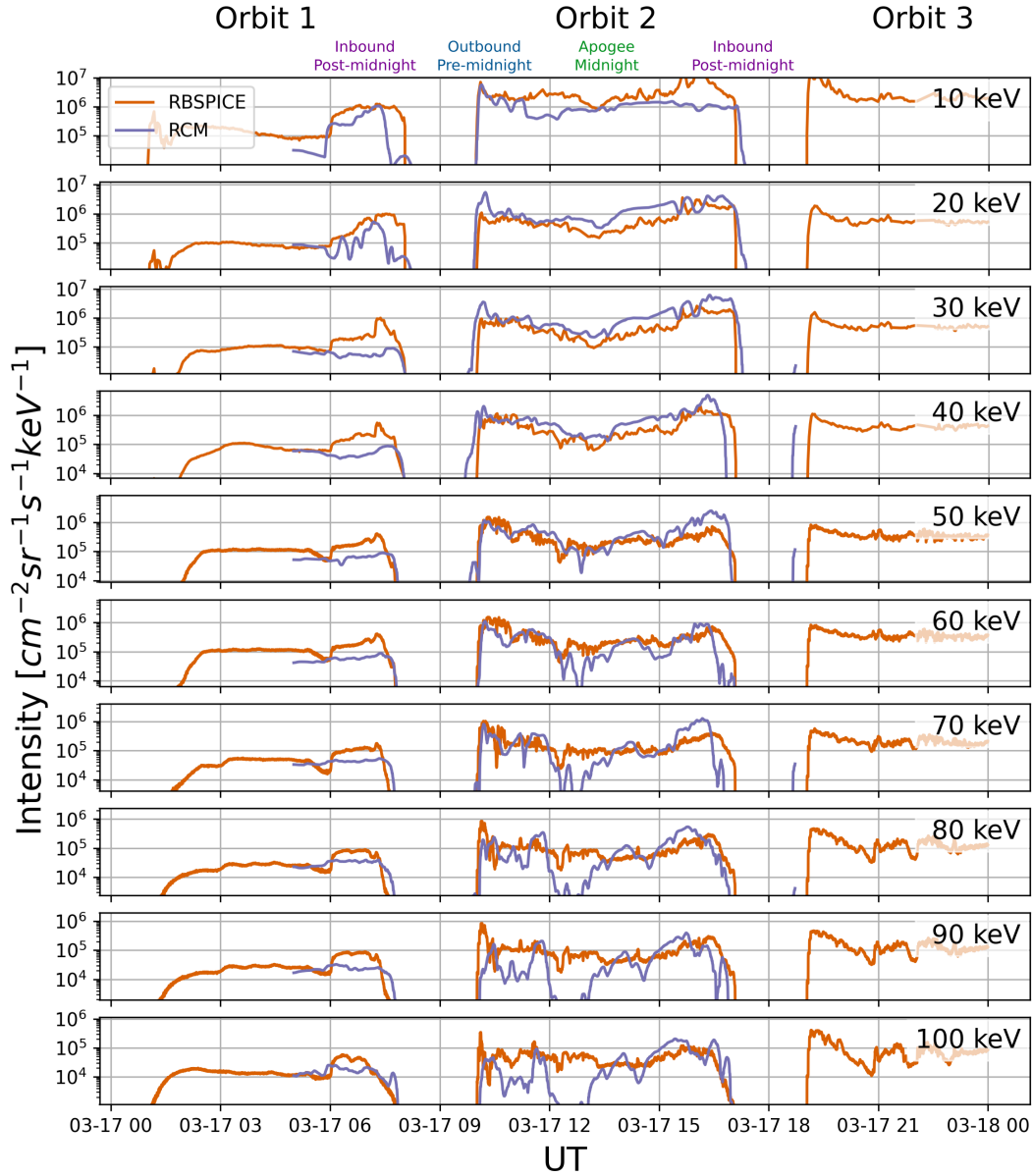


Figure 6. Comparison of the proton intensities during the March 17, 2013 storm between the RBSP-B's RBSPICE instrument measurements (orange) and the MAGE simulation, as calculated by RCM (purple). The ten panels show a comparison, each at a fixed energy denoted in the top right corner of the corresponding panel, between 10 and 100 keV. The comparison begins at 4:00 UT and ends at 19:00 UT. The RCM intensities have been smoothed over 5 minutes.

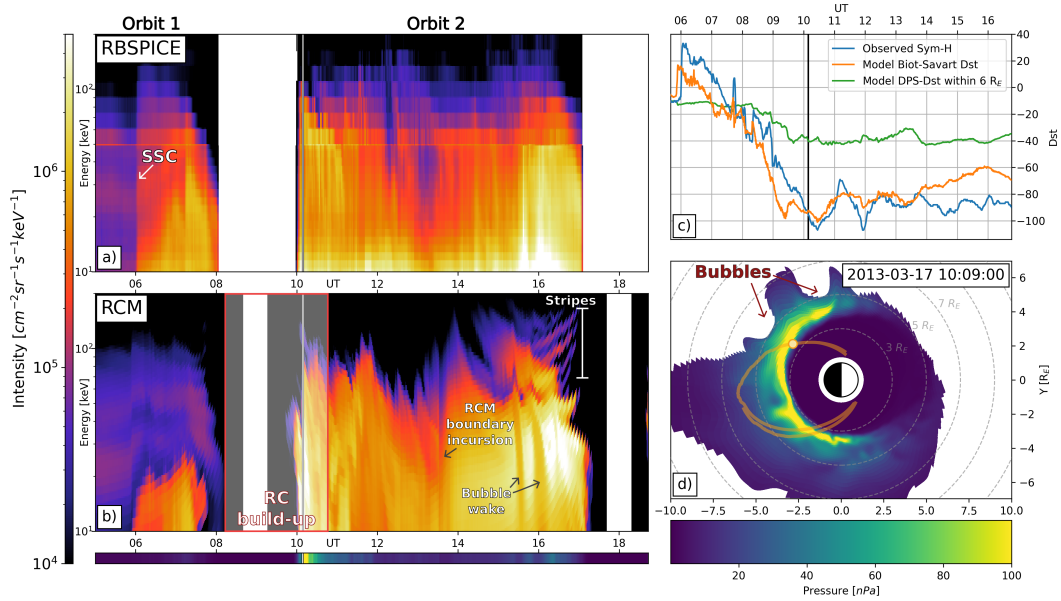


Figure 7. Comparison between RBSPICE (a) and RCM (b) proton intensities for the full energy spectra between 10 and 200 keV. (c) Comparison between the Observed Sym-H (blue), that calculated from the simulation (orange), and the DPS-*Dst* evaluated in the model within $6 R_E$ (green), the same as in Figure 1. (d) RCM pressure and RBSP-B's full trajectory (orange line) and current position (white circle with orange border) mapped along field lines to the equatorial plane. The vertical lines in panels (a), (b), and (c), and pressure and spacecraft location in panel (d), all correspond to the time indicated in panel (d). The thin colored bar below panel (b) shows the RCM pressure at the spacecraft location for a given time, with the same colorbar as panel (d).

500 Starting with Orbit 1, we observe that while the initial RCM population is rela-
 501 tively similar to that measured by RBSP-B, there are significant differences. SSC occurs
 502 during the inbound pass of this orbit (highlighted in Figure 7a). The intensity enhance-
 503 ment due to SSC compression is underestimated in the model, which can be attributed
 504 to a number of factors, including the initial energy spectrum in the model (constructed
 505 as described in section 2.3) being at a variance with the observed spectrum, limitations
 506 in the solar wind reconstruction (section 2.1) at producing the SSC shock (Figure 7c),
 507 and the uncertainty in the propagation of the upstream solar wind. As will be clear in
 508 the following analysis of the evolution of the energy spectra (section 3.3.2), the pre-storm
 509 plasma in this region contributed relatively little energy to the final ring current. How-
 510 ever, this initial population is still important because it influences the degree of stretch-
 511 ing in the tail which in turn affects where the initial reconnection will occur, and also
 512 sets the background entropy profile that the initial bubbles must penetrate through. This
 513 is discussed further in section 4.

514 As discussed above, the initial ring current buildup occurred between 08:15 and 10:45
 515 UT. Figure 7b indicates that, for almost the entirety of this period, RBSP-B was in the
 516 perigee phase of its orbit, where the spacecraft was below $3 R_E$ and RBSPICE was not
 517 taking time-of-flight measurements due to the high voltage mode being turned off. High-
 518 lighted in Figure 7d are two Earthward penetrating bubbles that manifest in this plot
 519 as two deformations of the RCM active domain due to their fast flow speeds (see the dis-
 520 cussion of the coupling algorithm in section 2.3). The radial velocity and magnetic field
 521 dipolarization within these bubbles are visible in Figure 2c and Figure 2d, and the en-
 522 thalpy flux and depleted entropy components are visible in Figure 3a and Figure 3c. These
 523 are the only bubbles during the initial buildup phase that the virtual spacecraft has a
 524 chance of observing as an injection, however it occurs just as the spacecraft encounters
 525 the inner edge of the ring current, masking their signatures.

526 However, throughout the outbound pass of Orbit 2 (between 10-14 UT as the space-
 527 craft passes from ~ 21 MLT to just past 00 MLT), the observed and simulated proton
 528 intensities are in strong agreement. This is manifested in the timing of RCM and RBSP-
 529 B's observation of the ring current along the outbound pass and indicates that the model
 530 is capturing the location of the peak ring current quite well for this storm. The inten-
 531 sities at this leading edge are in good agreement in general (Figure 6), though there is
 532 an overestimate at 20 and 30 keV, and an underestimate above 80 keV. Throughout the
 533 remainder of the Orbit 2 outbound pass, the intensities agree especially well between 30-
 534 70 keV, the best agreement being at 50 keV with a maximum ratio between the mod-
 535 eled and observed intensity of 5.2, and an average ratio of 1.3. Qualitatively, injection-
 536 like features in the observations are also present in the simulated spectra throughout the
 537 10-14 UT period, although inspection of Supplemental Video 2 shows that not all of these
 538 features are unambiguously caused by bubbles. Visible in the 60-90 keV range in Fig-
 539 ure 6 is a drop-out in intensity near Orbit 2 apogee. It is clearer in Figure 7 that there
 540 is a general lack of a $\sim 5 \times 10^4 \text{ cm}^{-2} \text{ sr}^{-1} \text{ s}^{-1} \text{ keV}^{-1}$ intensity background above 50 keV
 541 as seen in the data. A number of factors may contribute to the model missing this pop-
 542 ulation, such as the initial plasma sheet being too cold, the model not including non-adiabatic
 543 processes, or a "boundary shadowing" effect, whereby particles of the relevant energies
 544 drift out of the RCM domain, which is located a few R_E inward of the magnetopause.
 545 These particles are lost from the simulated ring current, whereas in reality they would
 546 have stayed trapped within the inner magnetosphere.

547 While the intensities at individual energies are still in good agreement for the in-
 548 bound half of Orbit 2, there is a major change in the structure of the modeled energy
 549 spectra starting just before 14:00 UT (highlighted in Figure 7b). At this time, reconnec-
 550 tion occurs close to $-10 R_E$ across the tail in the simulation, restricting the active RCM
 551 domain to below $6 R_E$ (visible in Supplemental Video 2). As the RCM active domain
 552 moves back out, it re-populates its plasma population with a fresh Kappa distribution

553 using the MHD moments at these locations (section 2.3), resulting in the smoothed en-
 554 ergy spectra seen for most of the inbound pass.

555 At 16:00, there are two strong injection signatures in the data, whereas the model
 556 shows two depletions in intensity at this time. It can be seen in Supplemental Video
 557 2 that these depletion signatures are from the virtual spacecraft passing through the wake
 558 of two bubbles that have already penetrated to a lower radial distance. There is also a
 559 stripe-like feature in the modeled intensities around 60-150 keV near the end of Orbit
 560 2. This is due to the injection related to the bubble that passed 6 R_E at 10:30 UT around
 561 20 MLT (see Figure 3) that has become significantly dispersed, so much so that it has
 562 wrapped around the Earth several times by 16:00 UT. In nature, this would not remain
 563 as such a coherent structure, as drift shell splitting would separate the different pitch
 564 angles over time (Roederer, 1967), whereas the isotropic approximation in RCM does
 565 not capture this effect.

566 At the end of the inbound pass of Orbit 2, the spacecraft passes through the ring
 567 current again around 3 MLT. (Figure 6) The model computes a greater local maximum
 568 in intensity for 40-80 keV protons in the 15 to 17 UT range, but also a dropoff in inten-
 569 sity earlier in the orbit than is observed. This implies that the modeled ring current within
 570 the post-midnight sector is stronger but also further from Earth than in reality. The pro-
 571 ton population in this region is dependent on a number of interacting factors, including:
 572 the location and energy of the source population of ring current protons; the competi-
 573 tion between Eastward $\mathbf{E} \times \mathbf{B}$ (i.e. convection and co-rotation) drifts and energy-dependent
 574 Westward gradient-curvature drifts; and the properties of the ring current itself that con-
 575 tribute to the ionospheric potential through shielding via Region 2 currents and the con-
 576 ductance profile via electron precipitation. Because of these interdependent complexi-
 577 ties, the divergence of the model from observations in this region is not unexpected, but
 578 the comparison yields key insights about the model's ability to capture these different
 579 factors.

580 3.3.2 Energy Spectra Evolution

581 Having discussed the data-model comparisons, we now turn to a more detailed in-
 582 vestigation of the ring current energy spectra in the model. Figure 8 shows the cumu-
 583 lative pressure as a function of energy and time at three stationary points indicated in
 584 panels (d-g). The first point (at 3.8 R_E and 21 MLT) marks the peak ring current pres-
 585 sure which occurred at 09:15 UT. The second and third points are located at 4.3 and 4.8
 586 R_E at the same MLT in order to sample the outer extent of the ring current. The white
 587 lines in Figure 8(a-c) denote the median and quartile energies of the cumulative pres-
 588 sure fraction, i.e. the proton energies lower than the 50% line collectively contribute half
 589 of the total pressure at that point and time. For ease of reference, we refer to this en-
 590 ergy as the "median energy." The cumulative pressure value at the top of Figures 8(a-
 591 c) is the total pressure for each point in time. Figures 8(d-g) show the total RCM pres-
 592 sure in the equatorial plane for four select times throughout the plotted period indicated
 593 by cyan vertical lines in Figures 8(a-c).

594 Preceding the main period of ring current buildup (before 9:00 UT, see Figure 5),
 595 the median energy at 4.3 and 4.8 R_E drops from 60 and 30 keV, respectively, to 20 keV.
 596 This is best explained by convection of the pre-existing plasma sheet (recall from Fig-
 597 ure 5 that prior to about 08:50 UT, inward transport was dominated by convection with
 598 only several bubbles present). However, only at 09:00 UT, just after significant trans-
 599 port via bubbles commences, does new plasma reach the 3.8 R_E probe point, where the
 600 drop to a median energy of 20 keV is accompanied by the greatest ring current pressure
 601 captured by the model. Over the course of many hours, the median energy increases to
 602 70-85 keV, depending on the location, while the total pressure at each location decreases

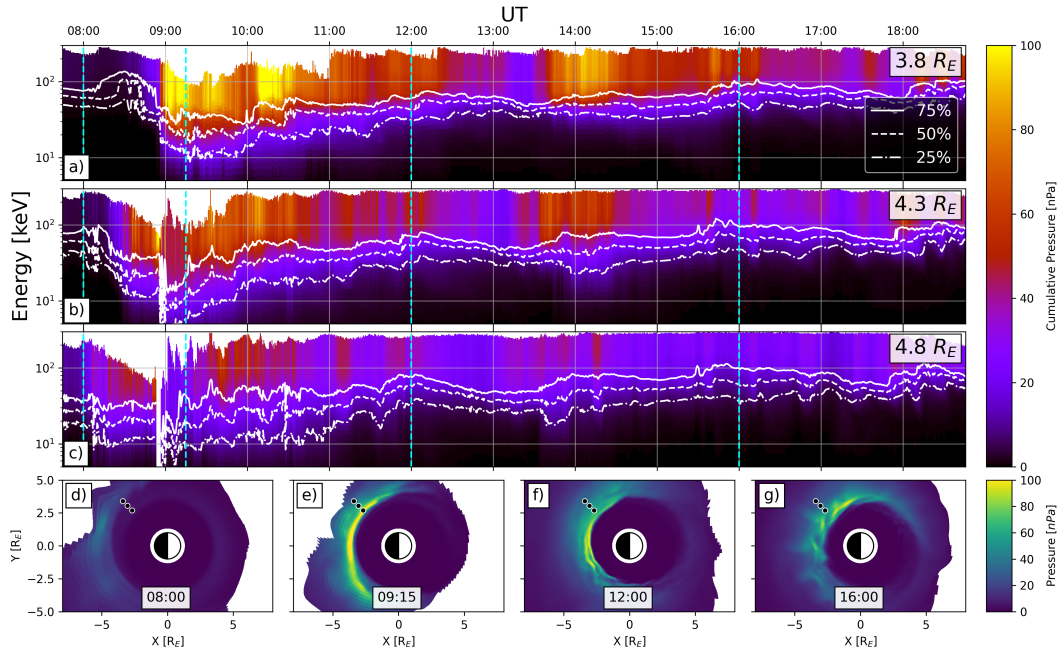


Figure 8. (a-c) RCM cumulative pressure as a function of energy and time at three stationary radial distances, denoted in the top right in each panel, along 21 MLT. The white lines denote the median and quartile values of the cumulative pressure fraction. The cyan lines correspond to the four times shown in panels (d-g). (d-g) equatorial views of the RCM total pressure at four select times. The three dots denote the locations at which the pressure in panels (a-c) is evaluated.

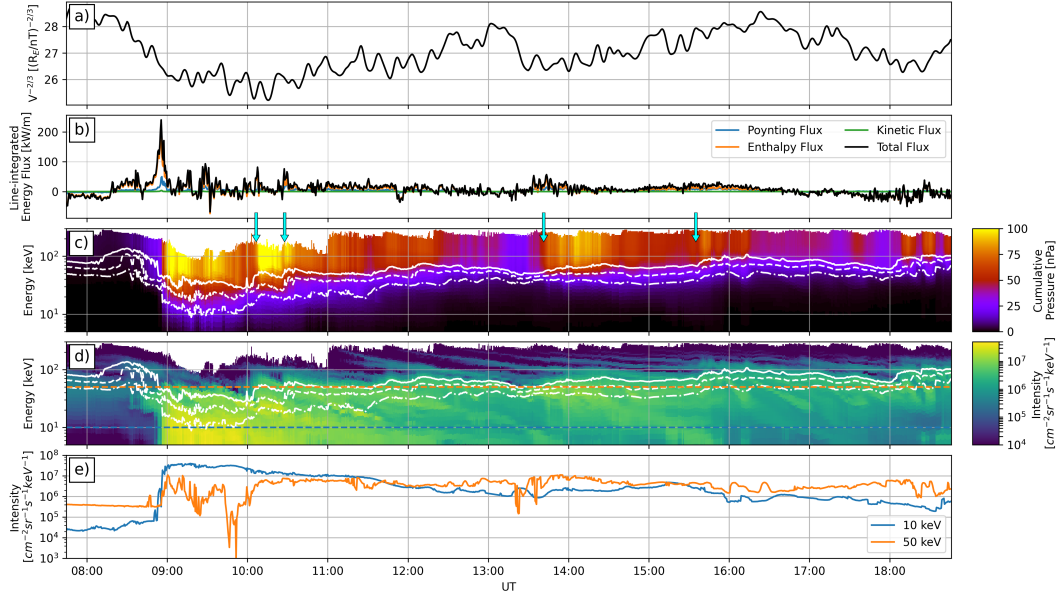


Figure 9. (a) Time-series of the quantity $V^{-2/3}$. (b) Time-series of the net energy flux through the nightside $6 R_E$ arc, identical to Figure 3d but over a longer period of time. (c) Cumulative pressure as a function of energy and time, identical to that in Figure 8a. (d) Proton intensity as a function of energy and time. (e) Time-series of proton intensities at 10 and 50 keV. Cyan arrows denote instances of sharp increases in the median energy and/or the total pressure.

603 on average. However, the relatively constant DPS- Dst value throughout this time indi-
 604 cates that the total energy content within $6 R_E$ is not appreciably changing.

605 We now focus our attention on the evolution of the median energy from <20 to 85
 606 keV between 09:00 and 19:00 UT at the $3.8 R_E$ probe location. This evolution may be
 607 caused by a localized heating of the already-present plasma population via adiabatic en-
 608 ergization (i.e. betatron acceleration due to magnetic field enhancements), the introduc-
 609 tion of hotter plasma from the tail later into the storm, and/or by energy-dependent loss
 610 processes. Figure 9 examines each of these processes. Figure 9a shows a time-series of
 611 the value $V^{-2/3}$, where V is the flux tube volume, evaluated at the $3.8 R_E$ probe loca-
 612 tion. Given the equation $W = \lambda V^{-2/3}$, where W is the kinetic energy and λ is the isotropic
 613 energy invariant (Wolf et al., 2009), changes in $V^{-2/3}$ are directly proportional to en-
 614 ergization via localized adiabatic heating. Figure 9b shows the energy flux through the
 615 nightside $6 R_E$ arc, identical to that in Figure 3d but extended in time. Figure 9d shows
 616 the proton intensity as a function of time and energy, and 9e shows a time-series of the
 617 proton intensity for the select energies of 10 and 50 keV, both evaluated at the $3.8 R_E$
 618 probe location. Note the log scale on the y axis.

619 After the initial ring current buildup, the value of $V^{-2/3}$ (Figure 9a) is fairly noisy
 620 but gradually increases by less than 10%. Therefore it contributes minimally to ener-
 621 gization over time. The initial buildup of the ring current (cumulative pressure in Fig-
 622 ure 9c at 09:00 UT) expectedly correlates well with the period of enhanced inward plasma
 623 transport examined in section 3.2. Just after 10:00 UT there is an enhancement in the
 624 total pressure as well as a jump in the median energy from 20 to 35 keV, and at 10:30
 625 UT there is another jump to 40 keV (denoted with cyan arrows in Figure 9c). There are
 626 two other notable periods of enhanced transport. One is around 13:40 UT and is related
 627 to the close-in reconnection event discussed in section 3.3.1, that results in an increase

in pressure but does not notably alter the energy spectra. The other, starting around 15:00 UT, results in a lesser increase in pressure but more appreciable increase to the median energy. These instances of enhancements to the median energy and/or pressure at the 3.8 R_E probe point all correlate well with periods of enhanced inward transport, implying that these changes in the energy spectra are related to transport of hotter plasma from the plasma sheet.

The intensity of the 50 keV protons (Figure 9d,e) remained relatively constant after the initial buildup at 09:00 UT, whereas the 10 keV population steadily decreases over time. Using the Østgaard et al. (2003) geocorona model and Lindsay and Stebbings (2005) proton cross sections (as implemented in RCM, see section 2.3), 10 keV protons with a 45° pitch angle at 3.8 R_E have a decay timescale of roughly 1.6 hours. Thus, charge exchange is capable of depleting the 10 keV protons by a factor of more than 250 over the nine hour period after the initial ring current buildup, whereas the 50 keV protons are expected to decay by a factor of 13 over the same period. According to Figure 9e, the 10 keV protons decreased by a factor of 200 and the 50 keV protons by a factor of 13 between their max value near 09 UT and their minimum value after 18 UT, consistent with the charge exchange decay rates. In total, the evolution of the median energy from 20 to 85 keV over the course of 9 hours is best explained by a combination of impulsive adjustments due to the transport of hotter plasma from the plasma sheet and a steady increase in the median energy due to energy-dependent charge exchange with the exosphere neutrals.

4 Discussion

While previous modeling studies have provided important insights in transport and ring current buildup via bubbles (e.g., Yang et al., 2015; Cramer et al., 2017; Sorathia et al., 2021), this paper is the first to target directly the quantification of the buildup of the ring current plasma energy content via bubbles generated self-consistently within a global geospace model. A major difference between the simulation in this study and those of Yang et al. (2015) is that in RCM-E, bubbles are generated via a reduction in pressure along a fixed outer boundary, with properties constrained by observations, whereas in this study the bubbles' generation location, pressure, flux tube volume, and flow speed are produced self-consistently by reconnection in the magnetotail (e.g. Wiltberger et al., 2015). Nevertheless, the 60% contribution from bubbles found by Yang et al. (2015) is quite similar to the lower bound of 50% calculated in this study. We emphasize again that the inclusion of the return flows in the calculation of the net transport via bubbles is crucial, as they transport a considerable amount of plasma energy outwards. A caveat to the results presented here is that the occurrence rate of highly-depleted bubbles is known to increase as grid resolution increases, up to a resolution higher than that used in this study (2x finer resolution in each dimension; Sorathia et al., 2021). It is possible that at a higher resolution, our estimate of a lower bound of 50% contribution from bubbles would be even higher. Also, this estimate is derived for this specific storm, and how this estimate changes based on specific storm characteristics is a matter for future multi-event study (c.f., Cramer et al., 2017).

Since fast flows are excluded from the RCM domain, and because GAMERA does not include heat flux on its own, the flux tube entropy of bubbles remain constant while they are being transported rapidly inwards. Particle tracing of ions (Ukhorskiy et al., 2018) and electrons (Gabrielse et al., 2017; Sorathia et al., 2018) within bubbles has demonstrated that their enhanced magnetic flux is capable of trapping relatively high-energy particles via gradient-curvature drifts whereas lower-energy particles may drift in and out of the bubble. This means that in reality the flux tube entropy is not a conserved quantity as the bubble is transported inwards. While the statistical properties of bubbles produced in GAMERA are in good agreement with observations (Sorathia et al., 2021), the interaction between the bubble and plasma at different energies is currently

680 not captured by the model. In addition to this, the fairly conservative constraint on the
 681 RCM active domain based on the distance to the open/closed field boundary also led to
 682 the boundary incursion on the RBSP orbit, resetting the energy spectrum to a smooth
 683 Kappa distribution (Figure 7b). While this did not greatly affect the intensities across
 684 the spectrum (inbound pass of Orbit 2 in Figure 6), it is unclear what effects this removal
 685 of structure may play on energy-dependent dynamics afterwards. These limitations arise
 686 from the fact that inner magnetosphere models do not appropriately handle fast flows,
 687 while the MHD model does not include gradient-curvature drifts in the bulk velocity. A
 688 model that is capable of handling both of these simultaneously is needed in order to un-
 689 derstand how the inclusion of these effects might alter bubble penetration depth and its
 690 implications on particle injections.

691 The peak ring current in the simulation (at $3.8 R_E$, Figure 8a) was composed of
 692 protons with a median energy of about 20 keV, consistent with the median energy seen
 693 earlier at 4.8 and $4.3 R_E$, whose origin is primarily the pre-storm plasma sheet popu-
 694 lation that has been transported inwards. After the peak ring current around 09:15 UT
 695 followed a series of impulsive increases to the median energy caused by injections of hot-
 696 ter plasma. A multi-phase evolution of the energy spectra has been observed for a num-
 697 ber of storms (e.g., Zhao et al., 2015; Goldstein et al., 2017; Keika et al., 2018). Keika
 698 et al. (2018), in their analysis of the 17 March 2015 storm, similarly attributed the ini-
 699 tial stormtime ring current population to the inward transport of the pre-storm plasma
 700 sheet, with the later increases in median energy being caused by the transport of a hot,
 701 dense plasma sheet population. Given the importance of the pre-storm plasma sheet pop-
 702 ulation to the initial ring current energy spectra, it is clear that the proper “pre-conditioning”
 703 of the simulation, i.e. setting the pre-storm magnetosphere state including the config-
 704 uration of the magnetotail and the population within the magnetosphere, is essential to
 705 capturing observed stormtime dynamics. As briefly mentioned above, properly model-
 706 ing bubble penetration relies both on capturing the background entropy profile right and
 707 on the bubble’s entropy. The pre-conditioning method employed in this simulation has
 708 performed well in reproducing the observed intensities in general, but the overestimate
 709 in the 20-30 keV range and underestimate in the 80-100 keV range (Figure 6) suggests
 710 that the method could be improved. This can be achieved e.g. by constraining with space-
 711 craft that traverse the outer plasma sheet such as THEMIS or by running the simula-
 712 tion for an even longer period before the storm onset to allow for a more self-consistent
 713 plasma sheet population to form. The question of the origin of the hotter plasma that
 714 was transported inwards at the later stage of the storm is beyond the scope of this pa-
 715 per but can be investigated with our model in the future (c.f., Keika et al., 2018, for the
 716 March 2015 storm). The median energy was also strongly influenced by charge exchange
 717 with the exosphere. This study used the Østgaard et al. (2003) geocorona model to cal-
 718 culate charge exchange rates. However, it is known that the decay rate is highly depen-
 719 dent on not only the choice of exosphere model (Ilie et al., 2013), but also on the vari-
 720 ation of the neutral density profile over the duration of geomagnetic storms (Cucho-Padin
 721 & Waldrop, 2019). The relative role of the transport of an evolving plasma sheet ver-
 722 sus charge exchange on the evolution of the ring current energy distribution is highly de-
 723 pendent on these factors, and is likely to change on a storm-by-storm basis.

724 Using the HOPE and RBSPICE instruments aboard the Van Allen Probes, Menz
 725 et al. (2017) found that during Orbit 2, O^+ contributed about 65% to the total ring cur-
 726 rent pressure in the $L = 3-4$ range, and decreased to a 50% contribution by $L = 5$. In-
 727 clusion of O^+ in our simulation could affect both the buildup and decay of the ring cur-
 728 rent. For the latter, we would not expect the model without O^+ to reproduce the ob-
 729 served recovery rate due to the much faster charge exchange rate of O^+ relative to H^+
 730 (Smith & Bewtra, 1978; Lindsay & Stebbings, 2005). It is less clear how O^+ would in-
 731 fluence the relative contribution of bubbles to ring current buildup, which was the fo-
 732 cus of this study. The effect of O^+ outflow on ring current buildup has been studied pre-
 733 viously using global MHD models coupled to ionospheric O^+ outflow and inner magne-

734 tosphere models (e.g., Welling et al., 2011). However, Sorathia et al. (2021) used test-
 735 particle simulations to demonstrate that plasma sheet flows do not transport O^+ as ef-
 736 ficiently as they do lighter ions because of significant non-adiabatic effects for the heavy
 737 species. This resulted in shallower penetration depths of O^+ than if these particles were
 738 constrained to adiabatic, guiding-center motion. Because the study did not include feed-
 739 back from the test particles on the MHD solution, it remains unclear to what extent non-
 740 adiabatic O^+ may in turn affect transport by bubbles in general. Therefore the inter-
 741 action between O^+ and bubbles, and the resulting impact it has on ring current buildup
 742 and evolution, would most appropriately be explored with a global magnetosphere model
 743 that is not only coupled with an ionospheric outflow model (e.g., Glocer et al., 2009; Var-
 744 ney et al., 2016), but one that also includes feedback from non-adiabatic O^+ .

745 With the above caveats in mind, our answer to the question, “how much of the plasma
 746 energy transport through $6 R_E$ is in the form of bubbles?” is $\sim 50\%$ for this simulation.
 747 However, we note that this question is different from asking, “what is the relative con-
 748 tribution of bubbles to ring current buildup compared to large-scale convection?” In a
 749 quantitative sense, it is up for interpretation how much a bubble “contributed” to ring
 750 current buildup in the case where plasma ultimately makes it to the ring current but was
 751 only transported part of the way by a bubble. Yang et al. (2015) seeded test particles
 752 in the final state of each of their simulations, back-traced them to the boundary, and de-
 753 termined if it entered the simulation within a bubble or through the global-scale flow.
 754 In this analysis, a bubble was considered to have contributed to the ring current even
 755 if it transported plasma only a short distance into the simulation domain, so long as the
 756 plasma remained in the domain by the end of the simulation. In this study, we exam-
 757 ined the net enthalpy flux due to bubbles through $6 R_E$, including the effects of com-
 758 pression ahead of the bubbles, which may have resulted in plasma at certain energies be-
 759 ing transported below their respective Alfvén layer, where they otherwise would have re-
 760 mained outside of it in the absence of the bubble. Because the bubbles examined in this
 761 study had a guaranteed and measurable contribution to the ring current energy content,
 762 and because it did not include the complexities of bubble contribution outside of $6 R_E$,
 763 this analysis definitively calculates a lower bound to bubble contribution, in the context
 764 of this specific simulation. The overall role of bubbles in ring current buildup remains
 765 only partially understood, and further investigation requires not only more complex anal-
 766 ysis methods, such as fluid-element and particle tracing, but also a more deep understand-
 767 ing of the physics of particle transport from the plasma sheet to the ring current and the
 768 development of the appropriate physics-based models.

769 5 Conclusion

770 Via a case study of the March 17, 2013 storm, we examined the contribution of BBFs/entropy-
 771 depleted bubbles to the buildup of the stormtime ring current, and the evolution of the
 772 ring current energy spectra throughout the main phase of the storm. The primary con-
 773 clusions of this study are as follows:

- 774 1. Energy transport through $6 R_E$ in the simulation is primarily in the form of en-
 775 thalpy flux, followed by magnetic flux and finally by the bulk kinetic flux. In other
 776 words, by $6 R_E$ the energy transported by bubbles is primarily in the form of plasma
 777 energy.
- 778 2. At $6 R_E$, 50% of the net inward enthalpy flux is contained within bubbles. This
 779 serves as a lower bound to the total contribution of plasma transported by bub-
 780 bles to the buildup of the stormtime ring current, as it only considers bubbles that
 781 have penetrated to below $6 R_E$, which constitutes a fraction of the total number
 782 of bubbles produced by the model.
- 783 3. The return flows that accompany bubbles as a result of interchange transport out-
 784 wards an average of 40% of the plasma energy transported through $6 R_E$ by the

- bubbles, thus their effect must be considered when quantifying the net contribution of bubbles to inward energy transport.
4. The data-model comparison shows that the model is accurately capturing both the radial location and magnitude, as well as the spectral properties of the initial ring current well, implying that the model is accurately reproducing the process of ring current buildup. Possible explanations for discrepancies between the data and model include inaccuracy in the initial plasma sheet conditions, boundary shadowing of higher-energy protons as a result of a conservatively constrained RCM active domain, and the absence of O^+ outflow and its effects on plasma sheet composition and bubble penetration depth.
 5. The evolution of the ring current energy spectra is caused by a combination of impulsive adjustments due to transport of a gradually hotter plasma sheet population and a steady increase due to energy-dependent charge exchange.

The use of state-of-the-art geospace models in combination with in-situ data continues to be a powerful tool in gaining a deeper understanding of the role of bubbles in plasma and magnetic flux transport during periods of high geomagnetic activity. While this study contributes to better understanding the drivers of stormtime ring current formation, there are many outstanding questions, such as how these results are altered depending on the solar wind driver, the more general relationship between mesoscale and global scale transport in the magnetotail, and the evolution of the plasma sheet source throughout the storm and where and how heating occurs. Deep analysis of model results enables more thorough validation via comparison to observations, and in turn increases the physical insight that may be gained through modeling.

6 Open Research

The solar wind data source is primarily Modified High Resolution OMNI (HRO) data (https://omniweb.gsfc.nasa.gov/form/omni_min_def.html). Data gaps were filled with KP-despiked Wind data from OMNIWeb (<https://omniweb.gsfc.nasa.gov>). Proton data from RBSPICE instrument aboard the Van Allen Probe B spacecraft was retrieved from cdaweb (<https://cdaweb.gsfc.nasa.gov>) via the cdasws python package (<https://pypi.org/project/cdasws/>). The model data was produced with the Multiscale Atmosphere Geospace Environment (MAGE) model, under development by the NASA DRIVE Science Center for Geospace Storms (<https://cgs.jhuapl.edu>). Figures 1 and 3 were made using the ParaView visualization software (<https://www.paraview.org>). All other figures were made using Matplotlib (<https://matplotlib.org/>). A subset of the model output data has been made available (<https://doi.org/10.5281/zenodo.7921979>), which includes all information necessary to generate all Figures, except for the 3D field line data in Figure 1. The repository also includes a conda (<https://docs.conda.io>) requirements file which may be used to recreate the python environment used to make the Figures generated using Matplotlib, as well as an example plotting script.

Acknowledgments

This work was supported by the NASA DRIVE Science Center for Geospace Storms (CGS) under award 80NSSC22M0163, and by the NASA grant 80NSSC19K0241. V.G.M. acknowledges support from NASA grants 80NSSC19K0071 and 80NSSC19K0080. K.S. acknowledges support from NASA grant 80NSSC20K1833. We would like to acknowledge the use of computational resources (doi:10.5065/D6RX99HX) at the NCAR-Wyoming Supercomputing Center provided by the National Science Foundation and the State of Wyoming, and supported by NCAR's Computational and Information Systems Laboratory.

833 **References**

- 834 Angelopoulos, V., Baumjohann, W., Kennel, C. F., Coroniti, F. V., Kivelson,
 835 M. G., Pellat, R., ... Paschmann, G. (1992). Bursty bulk flows in
 836 the inner central plasma sheet. *Journal of Geophysical Research: Space*
 837 *Physics*, *97*(A4), 4027–4039. Retrieved 2022-10-11, from [https://](https://onlinelibrary.wiley.com/doi/abs/10.1029/91JA02701)
 838 onlinelibrary.wiley.com/doi/abs/10.1029/91JA02701 (_eprint:
 839 <https://onlinelibrary.wiley.com/doi/pdf/10.1029/91JA02701>) doi: 10.1029/
 840 91JA02701
- 841 Angelopoulos, V., Kennel, C. F., Coroniti, F. V., Pellat, R., Kivelson, M. G.,
 842 Walker, R. J., ... Gosling, J. T. (1994). Statistical characteristics
 843 of bursty bulk flow events. *Journal of Geophysical Research: Space*
 844 *Physics*, *99*(A11), 21257–21280. Retrieved 2022-12-07, from [https://](https://onlinelibrary.wiley.com/doi/abs/10.1029/94JA01263)
 845 onlinelibrary.wiley.com/doi/abs/10.1029/94JA01263 (_eprint:
 846 <https://onlinelibrary.wiley.com/doi/pdf/10.1029/94JA01263>) doi: 10.1029/
 847 94JA01263
- 848 Angelopoulos, V., Phan, T. D., Larson, D. E., Mozer, F. S., Lin, R. P., Tsu-
 849 ruda, K., ... Yumoto, K. (1997). Magnetotail flow bursts: Associ-
 850 ation to global magnetospheric circulation, relationship to ionospheric
 851 activity and direct evidence for localization. *Geophysical Research*
 852 *Letters*, *24*(18), 2271–2274. Retrieved 2023-04-27, from [https://](https://onlinelibrary.wiley.com/doi/abs/10.1029/97GL02355)
 853 onlinelibrary.wiley.com/doi/abs/10.1029/97GL02355 (_eprint:
 854 <https://onlinelibrary.wiley.com/doi/pdf/10.1029/97GL02355>) doi: 10.1029/
 855 97GL02355
- 856 Axford, W. I. (1969). Magnetospheric convection. *Reviews of Geo-*
 857 *physics*, *7*(1-2), 421–459. Retrieved 2022-11-02, from [https://](https://onlinelibrary.wiley.com/doi/abs/10.1029/RG007i001p00421)
 858 onlinelibrary.wiley.com/doi/abs/10.1029/RG007i001p00421 (_eprint:
 859 <https://onlinelibrary.wiley.com/doi/pdf/10.1029/RG007i001p00421>) doi:
 860 10.1029/RG007i001p00421
- 861 Baker, D. N. (2008, May). Substorms in the earth’s magnetosphere. *AIP Conference*
 862 *Proceedings*, *144*(1), 184. Retrieved 2023-01-26, from [https://](https://aip.scitation.org/doi/abs/10.1063/1.35655)
 863 aip.scitation.org/doi/abs/10.1063/1.35655 (Publisher: American Institute of Physic-
 864 sAIP) doi: 10.1063/1.35655
- 865 Baumjohann, W. (1990). Characteristics of high-speed ion flows in the
 866 plasma sheet. *Journal of Geophysical Research: Space Physics*, *95*(A4),
 867 3801–3809. Retrieved 2022-12-07, from [https://](https://onlinelibrary.wiley.com/doi/abs/10.1029/JA095iA04p03801)
 868 onlinelibrary.wiley.com/doi/abs/10.1029/JA095iA04p03801 (_eprint:
 869 <https://onlinelibrary.wiley.com/doi/pdf/10.1029/JA095iA04p03801>) doi:
 870 10.1029/JA095iA04p03801
- 871 Birn, J., & Hesse, M. (2005, November). Energy release and conversion by re-
 872 connection in the magnetotail. *Annales Geophysicae*, *23*(10), 3365–3373.
 873 Retrieved 2022-04-14, from [https://](https://angeo.copernicus.org/articles/23/3365/2005/angeo-23-3365-2005.html)
 874 [angeo.copernicus.org/articles/23/
 875 3365/2005/angeo-23-3365-2005.html](https://angeo.copernicus.org/articles/23/3365/2005/angeo-23-3365-2005.html) (Publisher: Copernicus GmbH) doi:
 876 10.5194/angeo-23-3365-2005
- 876 Birn, J., Hesse, M., Schindler, K., & Zaharia, S. (2009). Role of en-
 877 tropy in magnetotail dynamics. *Journal of Geophysical Research:*
 878 *Space Physics*, *114*(A9). Retrieved 2022-04-12, from [https://](https://onlinelibrary.wiley.com/doi/abs/10.1029/2008JA014015)
 879 onlinelibrary.wiley.com/doi/abs/10.1029/2008JA014015 (_eprint:
 880 <https://onlinelibrary.wiley.com/doi/pdf/10.1029/2008JA014015>) doi:
 881 10.1029/2008JA014015
- 882 Birn, J., Nakamura, R., Panov, E. V., & Hesse, M. (2011). Bursty bulk flows
 883 and dipolarization in MHD simulations of magnetotail reconnection. *Jour-*
 884 *nal of Geophysical Research: Space Physics*, *116*(A1). Retrieved 2022-11-28,
 885 from [https://](https://onlinelibrary.wiley.com/doi/abs/10.1029/2010JA016083)
 886 onlinelibrary.wiley.com/doi/abs/10.1029/2010JA016083
 887 (_eprint: <https://onlinelibrary.wiley.com/doi/pdf/10.1029/2010JA016083>) doi:
 888 10.1029/2010JA016083

- 888 Chapman, S. (1962). Earth storms: Retrospect and prospect. *Journal of the Physi-*
 889 *cal Society of Japan*, 17.
- 890 Chen, C. X., & Wolf, R. A. (1993). Interpretation of high-speed flows in
 891 the plasma sheet. *Journal of Geophysical Research: Space Physics*,
 892 98(A12), 21409–21419. Retrieved 2023-02-03, from [https://](https://onlinelibrary.wiley.com/doi/abs/10.1029/93JA02080)
 893 onlinelibrary.wiley.com/doi/abs/10.1029/93JA02080 (_eprint:
 894 <https://onlinelibrary.wiley.com/doi/pdf/10.1029/93JA02080>) doi: 10.1029/
 895 93JA02080
- 896 Chen, M. W., Lemon, C. L., Hecht, J., Sazykin, S., Wolf, R. A., Boyd, A.,
 897 & Valek, P. (2019). Diffuse Auroral Electron and Ion Precipita-
 898 tion Effects on RCM-E Comparisons With Satellite Data During the 17
 899 March 2013 Storm. *Journal of Geophysical Research: Space Physics*,
 900 124(6), 4194–4216. Retrieved 2020-07-06, from [https://](https://agupubs.onlinelibrary.wiley.com/doi/abs/10.1029/2019JA026545)
 901 [agupubs](https://agupubs.onlinelibrary.wiley.com/doi/abs/10.1029/2019JA026545)
 902 [.onlinelibrary.wiley.com/doi/abs/10.1029/2019JA026545](https://agupubs.onlinelibrary.wiley.com/doi/pdf/10.1029/2019JA026545) (_eprint:
 903 <https://agupubs.onlinelibrary.wiley.com/doi/pdf/10.1029/2019JA026545>) doi:
 904 10.1029/2019JA026545
- 904 Chen, M. W., Schulz, M., & Lyons, L. R. (1997). Modeling of Ring Cur-
 905 rent Formation and Decay: A Review. In *Magnetic Storms* (pp. 173–
 906 186). American Geophysical Union (AGU). Retrieved 2023-03-10, from
 907 <https://onlinelibrary.wiley.com/doi/abs/10.1029/GM098p0173>
 908 (_eprint: <https://onlinelibrary.wiley.com/doi/pdf/10.1029/GM098p0173>)
 909 doi: 10.1029/GM098p0173
- 910 Chen, M. W., Schulz, M., Lyons, L. R., & Gorney, D. J. (1993). Stormtime
 911 transport of ring current and radiation belt ions. *Journal of Geophysi-*
 912 *cal Research: Space Physics*, 98(A3), 3835–3849. Retrieved 2022-12-08,
 913 from <https://onlinelibrary.wiley.com/doi/abs/10.1029/92JA02608>
 914 (_eprint: <https://onlinelibrary.wiley.com/doi/pdf/10.1029/92JA02608>) doi:
 915 10.1029/92JA02608
- 916 Cramer, W. D., Raeder, J., Toffoletto, F. R., Gilson, M., & Hu, B. (2017).
 917 Plasma sheet injections into the inner magnetosphere: Two-way cou-
 918 pled OpenGGCM-RCM model results. *Journal of Geophysical Re-*
 919 *search: Space Physics*, 122(5), 5077–5091. Retrieved 2022-06-07, from
 920 <https://onlinelibrary.wiley.com/doi/abs/10.1002/2017JA024104>
 921 (_eprint: <https://onlinelibrary.wiley.com/doi/pdf/10.1002/2017JA024104>)
 922 doi: 10.1002/2017JA024104
- 923 Cucho-Padin, G., & Waldrop, L. (2019). Time-Dependent Response of the
 924 Terrestrial Exosphere to a Geomagnetic Storm. *Geophysical Research*
 925 *Letters*, 46(21), 11661–11670. Retrieved 2023-03-09, from [https://](https://onlinelibrary.wiley.com/doi/abs/10.1029/2019GL084327)
 926 onlinelibrary.wiley.com/doi/abs/10.1029/2019GL084327 (_eprint:
 927 <https://onlinelibrary.wiley.com/doi/pdf/10.1029/2019GL084327>) doi:
 928 10.1029/2019GL084327
- 929 Daglis, I. A. (2006, June). Ring Current Dynamics. *Space Science Reviews*, 124(1),
 930 183–202. Retrieved 2022-07-18, from [https://doi.org/10.1007/s11214-006-](https://doi.org/10.1007/s11214-006-9104-z)
 931 [-9104-z](https://doi.org/10.1007/s11214-006-9104-z) doi: 10.1007/s11214-006-9104-z
- 932 Daglis, I. A., Thorne, R. M., Baumjohann, W., & Orsini, S. (1999). The
 933 terrestrial ring current: Origin, formation, and decay. *Reviews of*
 934 *Geophysics*, 37(4), 407–438. Retrieved 2023-03-08, from [https://](https://onlinelibrary.wiley.com/doi/abs/10.1029/1999RG900009)
 935 onlinelibrary.wiley.com/doi/abs/10.1029/1999RG900009 (_eprint:
 936 <https://onlinelibrary.wiley.com/doi/pdf/10.1029/1999RG900009>) doi:
 937 10.1029/1999RG900009
- 938 Dang, T., Lei, J., Wang, W., Wang, B., Zhang, B., Liu, J., ... Nishimura,
 939 Y. (2019). Formation of Double Tongues of Ionization During the 17
 940 March 2013 Geomagnetic Storm. *Journal of Geophysical Research: Space*
 941 *Physics*, 124(12), 10619–10630. Retrieved 2023-03-01, from [https://](https://onlinelibrary.wiley.com/doi/abs/10.1029/2019JA027268)
 942 onlinelibrary.wiley.com/doi/abs/10.1029/2019JA027268 (_eprint:

- 943 <https://onlinelibrary.wiley.com/doi/pdf/10.1029/2019JA027268> doi:
944 10.1029/2019JA027268
- 945 Dessler, A. J., & Parker, E. N. (1959). Hydromagnetic theory of geomag-
946 netic storms. *Journal of Geophysical Research (1896-1977)*, 64(12),
947 2239–2252. Retrieved 2022-12-06, from [https://onlinelibrary](https://onlinelibrary.wiley.com/doi/abs/10.1029/JZ064i012p02239)
948 [.wiley.com/doi/abs/10.1029/JZ064i012p02239](https://onlinelibrary.wiley.com/doi/abs/10.1029/JZ064i012p02239) (_eprint:
949 <https://onlinelibrary.wiley.com/doi/pdf/10.1029/JZ064i012p02239>) doi:
950 10.1029/JZ064i012p02239
- 951 Dubyagin, S., Sergeev, V., Apatenkov, S., Angelopoulos, V., Runov, A., Nakamura,
952 R., ... Larson, D. (2011). Can flow bursts penetrate into the inner magneto-
953 sphere? *Geophysical Research Letters*, 38(8), n/a–n/a. Retrieved 2022-04-12,
954 from [https://www.academia.edu/17645753/Can_flow_bursts_penetrate](https://www.academia.edu/17645753/Can_flow_bursts_penetrate_into_the_inner_magnetosphere)
955 [_into_the_inner_magnetosphere](https://www.academia.edu/17645753/Can_flow_bursts_penetrate_into_the_inner_magnetosphere)
- 956 Ebihara, Y., & Ejiri, M. (2000). Simulation study on fundamental properties
957 of the storm-time ring current. *Journal of Geophysical Research: Space*
958 *Physics*, 105(A7), 15843–15859. Retrieved 2022-12-08, from [https://](https://onlinelibrary.wiley.com/doi/abs/10.1029/1999JA900493)
959 onlinelibrary.wiley.com/doi/abs/10.1029/1999JA900493 (_eprint:
960 <https://onlinelibrary.wiley.com/doi/pdf/10.1029/1999JA900493>) doi:
961 10.1029/1999JA900493
- 962 Erickson, G. M., & Wolf, R. A. (1980). Is steady convection possible
963 in the Earth's magnetotail? *Geophysical Research Letters*, 7(11),
964 897–900. Retrieved 2022-12-07, from [https://onlinelibrary](https://onlinelibrary.wiley.com/doi/abs/10.1029/GL007i011p00897)
965 [.wiley.com/doi/abs/10.1029/GL007i011p00897](https://onlinelibrary.wiley.com/doi/abs/10.1029/GL007i011p00897) (_eprint:
966 <https://onlinelibrary.wiley.com/doi/pdf/10.1029/GL007i011p00897>) doi:
967 10.1029/GL007i011p00897
- 968 Fok, M.-C., Buzulukova, N. Y., Chen, S.-H., Glocer, A., Nagai, T., Valek, P.,
969 & Perez, J. D. (2014). The Comprehensive Inner Magnetosphere-
970 Ionosphere Model. *Journal of Geophysical Research: Space Physics*,
971 119(9), 7522–7540. Retrieved 2021-02-19, from [https://agupubs](https://agupubs.onlinelibrary.wiley.com/doi/abs/10.1002/2014JA020239)
972 [.onlinelibrary.wiley.com/doi/abs/10.1002/2014JA020239](https://agupubs.onlinelibrary.wiley.com/doi/abs/10.1002/2014JA020239) (_eprint:
973 <https://agupubs.onlinelibrary.wiley.com/doi/pdf/10.1002/2014JA020239>) doi:
974 <https://doi.org/10.1002/2014JA020239>
- 975 Fok, M. C., Kozyra, J. U., Nagy, A. F., Rasmussen, C. E., & Khazanov,
976 G. V. (1993). Decay of equatorial ring current ions and associated
977 aeronomical consequences. *Journal of Geophysical Research: Space*
978 *Physics*, 98(A11), 19381–19393. Retrieved 2022-12-20, from [https://](https://onlinelibrary.wiley.com/doi/abs/10.1029/93JA01848)
979 onlinelibrary.wiley.com/doi/abs/10.1029/93JA01848 (_eprint:
980 <https://onlinelibrary.wiley.com/doi/pdf/10.1029/93JA01848>) doi: 10.1029/
981 93JA01848
- 982 Gabrielse, C., Angelopoulos, V., Harris, C., Artemyev, A., Kepko, L., & Runov,
983 A. (2017). Extensive electron transport and energization via mul-
984 tiple, localized dipolarizing flux bundles. *Journal of Geophysical Re-*
985 *search: Space Physics*, 122(5), 5059–5076. Retrieved 2022-08-24, from
986 <https://onlinelibrary.wiley.com/doi/abs/10.1002/2017JA023981>
987 (_eprint: <https://onlinelibrary.wiley.com/doi/pdf/10.1002/2017JA023981>)
988 doi: 10.1002/2017JA023981
- 989 Gabrielse, C., Angelopoulos, V., Runov, A., & Turner, D. L. (2012). The ef-
990 fects of transient, localized electric fields on equatorial electron accel-
991 eration and transport toward the inner magnetosphere. *Journal of Geo-*
992 *physical Research: Space Physics*, 117(A10). Retrieved 2023-02-03, from
993 <https://onlinelibrary.wiley.com/doi/abs/10.1029/2012JA017873>
994 (_eprint: <https://onlinelibrary.wiley.com/doi/pdf/10.1029/2012JA017873>)
995 doi: 10.1029/2012JA017873
- 996 Gabrielse, C., Angelopoulos, V., Runov, A., & Turner, D. L. (2014).
997 Statistical characteristics of particle injections throughout the

- 998 equatorial magnetotail. *Journal of Geophysical Research: Space*
 999 *Physics*, 119(4), 2512–2535. Retrieved 2023-01-23, from [https://](https://onlinelibrary.wiley.com/doi/abs/10.1002/2013JA019638)
 1000 onlinelibrary.wiley.com/doi/abs/10.1002/2013JA019638 (_eprint:
 1001 <https://onlinelibrary.wiley.com/doi/pdf/10.1002/2013JA019638>) doi:
 1002 10.1002/2013JA019638
- 1003 Gallagher, D. L., Craven, P. D., & Comfort, R. H. (2000, August). Global core
 1004 plasma model. *Journal of Geophysical Research*, 105, 18. Retrieved 2021-
 1005 02-27, from <http://adsabs.harvard.edu/abs/2000JGR...10518819G> doi: 10
 1006 .1029/1999JA000241
- 1007 Ganushkina, N. Y., Liemohn, M. W., & Dubyagin, S. (2018). Cur-
 1008 rent Systems in the Earth’s Magnetosphere. *Reviews of Geophysics*,
 1009 56(2), 309–332. Retrieved 2021-03-29, from [https://agupubs](https://agupubs.onlinelibrary.wiley.com/doi/abs/10.1002/2017RG000590)
 1010 [.onlinelibrary.wiley.com/doi/abs/10.1002/2017RG000590](https://agupubs.onlinelibrary.wiley.com/doi/abs/10.1002/2017RG000590) (_eprint:
 1011 <https://agupubs.onlinelibrary.wiley.com/doi/pdf/10.1002/2017RG000590>) doi:
 1012 <https://doi.org/10.1002/2017RG000590>
- 1013 Gkioulidou, M., Ukhorskiy, A. Y., Mitchell, D. G., & Lanzerotti, L. J. (2016).
 1014 Storm time dynamics of ring current protons: Implications for the long-
 1015 term energy budget in the inner magnetosphere. *Geophysical Research*
 1016 *Letters*, 43(10), 4736–4744. Retrieved 2021-09-16, from [https://](https://onlinelibrary.wiley.com/doi/abs/10.1002/2016GL068013)
 1017 onlinelibrary.wiley.com/doi/abs/10.1002/2016GL068013 (_eprint:
 1018 <https://agupubs.onlinelibrary.wiley.com/doi/pdf/10.1002/2016GL068013>) doi:
 1019 10.1002/2016GL068013
- 1020 Gkioulidou, M., Ukhorskiy, A. Y., Mitchell, D. G., Sotirelis, T., Mauk, B. H.,
 1021 & Lanzerotti, L. J. (2014). The role of small-scale ion injections in
 1022 the buildup of Earth’s ring current pressure: Van Allen Probes obser-
 1023 vations of the 17 March 2013 storm. *Journal of Geophysical Research:*
 1024 *Space Physics*, 119(9), 7327–7342. Retrieved 2021-09-24, from [https://](https://onlinelibrary.wiley.com/doi/abs/10.1002/2014JA020096)
 1025 onlinelibrary.wiley.com/doi/abs/10.1002/2014JA020096 (_eprint:
 1026 <https://onlinelibrary.wiley.com/doi/pdf/10.1002/2014JA020096>) doi:
 1027 10.1002/2014JA020096
- 1028 Glocer, A., Tóth, G., Gombosi, T., & Welling, D. (2009). Modeling iono-
 1029 spheric outflows and their impact on the magnetosphere, initial re-
 1030 sults. *Journal of Geophysical Research: Space Physics*, 114(A5).
 1031 Retrieved 2021-04-22, from [https://agupubs.onlinelibrary](https://agupubs.onlinelibrary.wiley.com/doi/abs/10.1029/2009JA014053)
 1032 [.wiley.com/doi/abs/10.1029/2009JA014053](https://agupubs.onlinelibrary.wiley.com/doi/abs/10.1029/2009JA014053) (_eprint:
 1033 <https://agupubs.onlinelibrary.wiley.com/doi/pdf/10.1029/2009JA014053>)
 1034 doi: <https://doi.org/10.1029/2009JA014053>
- 1035 Goldstein, J., Angelopoulos, V., De Pascuale, S., Funsten, H. O., Kurth, W. S.,
 1036 Llera, K., ... Wygant, J. R. (2017). Cross-scale observations of the 2015 St.
 1037 Patrick’s day storm: THEMIS, Van Allen Probes, and TWINS. *Journal of*
 1038 *Geophysical Research: Space Physics*, 122(1), 368–392. Retrieved 2023-02-23,
 1039 from <https://onlinelibrary.wiley.com/doi/abs/10.1002/2016JA023173>
 1040 (_eprint: <https://onlinelibrary.wiley.com/doi/pdf/10.1002/2016JA023173>) doi:
 1041 10.1002/2016JA023173
- 1042 Gurnett, D. A. (1970). Satellite Measurements of DC Electric Fields in the Iono-
 1043 sphere. In B. M. McCormac (Ed.), *Particles and Fields in the Magnetosphere*
 1044 (pp. 239–246). Dordrecht: Springer Netherlands. doi: 10.1007/978-94-010-3284
 1045 -1_23
- 1046 Hamilton, D. C., Gloeckler, G., Ipavich, F. M., Stüdemann, W., Wilken, B., &
 1047 Kremser, G. (1988). Ring current development during the great geomag-
 1048 netic storm of February 1986. *Journal of Geophysical Research: Space*
 1049 *Physics*, 93(A12), 14343–14355. Retrieved 2022-12-06, from [https://](https://onlinelibrary.wiley.com/doi/abs/10.1029/JA093iA12p14343)
 1050 onlinelibrary.wiley.com/doi/abs/10.1029/JA093iA12p14343 (_eprint:
 1051 <https://onlinelibrary.wiley.com/doi/pdf/10.1029/JA093iA12p14343>) doi:
 1052 10.1029/JA093iA12p14343

- 1053 Hori, T., Lui, A. T. Y., Ohtani, S., Cson Brandt, P., Mauk, B. H., McEn-
1054 tire, R. W., ... Hayakawa, H. (2005). Storm-time convection elec-
1055 tric field in the near-Earth plasma sheet. *Journal of Geophysical Re-*
1056 *search: Space Physics*, 110(A4). Retrieved 2022-12-07, from [https://](https://onlinelibrary.wiley.com/doi/abs/10.1029/2004JA010449)
1057 onlinelibrary.wiley.com/doi/abs/10.1029/2004JA010449 (_eprint:
1058 <https://onlinelibrary.wiley.com/doi/pdf/10.1029/2004JA010449>) doi:
1059 10.1029/2004JA010449
- 1060 Iijima, T., & Potemra, T. A. (1976). The amplitude distribution of
1061 field-aligned currents at northern high latitudes observed by Triad.
1062 *Journal of Geophysical Research (1896-1977)*, 81(13), 2165–2174.
1063 Retrieved 2021-03-31, from [https://agupubs.onlinelibrary](https://agupubs.onlinelibrary.wiley.com/doi/abs/10.1029/JA081i013p02165)
1064 [.wiley.com/doi/abs/10.1029/JA081i013p02165](https://agupubs.onlinelibrary.wiley.com/doi/abs/10.1029/JA081i013p02165) (_eprint:
1065 <https://agupubs.onlinelibrary.wiley.com/doi/pdf/10.1029/JA081i013p02165>)
1066 doi: <https://doi.org/10.1029/JA081i013p02165>
- 1067 Ilie, R., Skoug, R. M., Funsten, H. O., Liemohn, M. W., Bailey, J. J., & Gruntman,
1068 M. (2013, July). The impact of geocoronal density on ring current devel-
1069 opment. *Journal of Atmospheric and Solar-Terrestrial Physics*, 99, 92–103.
1070 Retrieved 2023-03-09, from [https://www.sciencedirect.com/science/](https://www.sciencedirect.com/science/article/pii/S1364682612000946)
1071 [article/pii/S1364682612000946](https://www.sciencedirect.com/science/article/pii/S1364682612000946) doi: 10.1016/j.jastp.2012.03.010
- 1072 Jaggi, R. K., & Wolf, R. A. (1973). Self-consistent calculation of the mo-
1073 tion of a sheet of ions in the magnetosphere. *Journal of Geophysical*
1074 *Research (1896-1977)*, 78(16), 2852–2866. Retrieved 2023-03-10, from
1075 <https://onlinelibrary.wiley.com/doi/abs/10.1029/JA078i016p02852>
1076 (_eprint: <https://onlinelibrary.wiley.com/doi/pdf/10.1029/JA078i016p02852>)
1077 doi: 10.1029/JA078i016p02852
- 1078 Jordanova, V. K., Farrugia, C. J., Janoo, L., Quinn, J. M., Torbert, R. B., Ogilvie,
1079 K. W., ... Belian, R. D. (1998). October 1995 magnetic cloud and ac-
1080 companying storm activity: Ring current evolution. *Journal of Geophys-*
1081 *ical Research: Space Physics*, 103(A1), 79–92. Retrieved 2022-12-20,
1082 from <https://onlinelibrary.wiley.com/doi/abs/10.1029/97JA02367>
1083 (_eprint: <https://onlinelibrary.wiley.com/doi/pdf/10.1029/97JA02367>) doi:
1084 10.1029/97JA02367
- 1085 Jordanova, V. K., Ilie, R., & Chen, M. W. (2020, January). Chapter 1 - Introduc-
1086 tion and historical background. In V. K. Jordanova, R. Ilie, & M. W. Chen
1087 (Eds.), *Ring Current Investigations* (pp. 1–13). Elsevier. Retrieved 2023-
1088 04-11, from [https://www.sciencedirect.com/science/article/pii/](https://www.sciencedirect.com/science/article/pii/B9780128155714000019)
1089 [B9780128155714000019](https://www.sciencedirect.com/science/article/pii/B9780128155714000019) doi: 10.1016/B978-0-12-815571-4.00001-9
- 1090 Jordanova, V. K., Kistler, L. M., Kozyra, J. U., Khazanov, G. V., & Nagy, A. F.
1091 (1996). Collisional losses of ring current ions. *Journal of Geophys-*
1092 *ical Research: Space Physics*, 101(A1), 111–126. Retrieved 2023-01-24,
1093 from <https://onlinelibrary.wiley.com/doi/abs/10.1029/95JA02000>
1094 (_eprint: <https://onlinelibrary.wiley.com/doi/pdf/10.1029/95JA02000>) doi:
1095 10.1029/95JA02000
- 1096 Jordanova, V. K., & Miyoshi, Y. (2005). Relativistic model of ring cur-
1097 rent and radiation belt ions and electrons: Initial results. *Geophys-*
1098 *ical Research Letters*, 32(14). Retrieved 2023-04-14, from [https://](https://onlinelibrary.wiley.com/doi/abs/10.1029/2005GL023020)
1099 onlinelibrary.wiley.com/doi/abs/10.1029/2005GL023020 (_eprint:
1100 <https://onlinelibrary.wiley.com/doi/pdf/10.1029/2005GL023020>) doi:
1101 10.1029/2005GL023020
- 1102 Jordanova, V. K., Yu, Y., Niehof, J. T., Skoug, R. M., Reeves, G. D., Klet-
1103 zing, C. A., ... Spence, H. E. (2014). Simulations of inner mag-
1104 netosphere dynamics with an expanded RAM-SCB model and com-
1105 parisons with Van Allen Probes observations. *Geophysical Research*
1106 *Letters*, 41(8), 2687–2694. Retrieved 2021-12-04, from [https://](https://onlinelibrary.wiley.com/doi/abs/10.1002/2014GL059533)
1107 onlinelibrary.wiley.com/doi/abs/10.1002/2014GL059533 (_eprint:

- 1108 <https://onlinelibrary.wiley.com/doi/pdf/10.1002/2014GL059533>) doi:
1109 10.1002/2014GL059533
- 1110 Keesee, A. M., Buzulukova, N., Mouikis, C., & Scime, E. E. (2021). Mesoscale Structures in Earth's Magnetotail Observed Using Energetic Neutral Atom Imaging.
1111 *Geophysical Research Letters*, 48(3), e2020GL091467. Retrieved 2023-01-25,
1112 from <https://onlinelibrary.wiley.com/doi/abs/10.1029/2020GL091467>
1113 (_eprint: <https://onlinelibrary.wiley.com/doi/pdf/10.1029/2020GL091467>) doi:
1114 10.1029/2020GL091467
- 1115
1116 Keika, K., Nosé, M., Ohtani, S., Takahashi, K., Christon, S. P., & McEntire,
1117 R. W. (2005). Outflow of energetic ions from the magnetosphere and its
1118 contribution to the decay of the storm time ring current. *Journal of Geo-*
1119 *physical Research: Space Physics*, 110(A9). Retrieved 2022-12-20, from
1120 <https://onlinelibrary.wiley.com/doi/abs/10.1029/2004JA010970>
1121 (_eprint: <https://onlinelibrary.wiley.com/doi/pdf/10.1029/2004JA010970>)
1122 doi: 10.1029/2004JA010970
- 1123 Keika, K., Seki, K., Nosé, M., Miyoshi, Y., Lanzerotti, L. J., Mitchell, D. G.,
1124 ... Manweiler, J. W. (2018). Three-Step Buildup of the 17 March
1125 2015 Storm Ring Current: Implication for the Cause of the Unex-
1126 pected Storm Intensification. *Journal of Geophysical Research: Space*
1127 *Physics*, 123(1), 414–428. Retrieved 2021-07-14, from [https://agupubs](https://agupubs.onlinelibrary.wiley.com/doi/abs/10.1002/2017JA024462)
1128 [.onlinelibrary.wiley.com/doi/abs/10.1002/2017JA024462](https://agupubs.onlinelibrary.wiley.com/doi/abs/10.1002/2017JA024462) (_eprint:
1129 <https://agupubs.onlinelibrary.wiley.com/doi/pdf/10.1002/2017JA024462>) doi:
1130 10.1002/2017JA024462
- 1131 Kistler, L. M. (2020). Ionospheric and Solar Wind Contributions to the
1132 Storm-Time Near-Earth Plasma Sheet. *Geophysical Research Let-*
1133 *ters*, 47(23), e2020GL090235. Retrieved 2023-01-09, from [https://](https://onlinelibrary.wiley.com/doi/abs/10.1029/2020GL090235)
1134 onlinelibrary.wiley.com/doi/abs/10.1029/2020GL090235 (_eprint:
1135 <https://onlinelibrary.wiley.com/doi/pdf/10.1029/2020GL090235>) doi:
1136 10.1029/2020GL090235
- 1137 Kistler, L. M., Ipavich, F. M., Hamilton, D. C., Gloeckler, G., Wilken, B., Kremser,
1138 G., & Stüdemann, W. (1989). Energy spectra of the major ion species in
1139 the ring current during geomagnetic storms. *Journal of Geophysical Re-*
1140 *search: Space Physics*, 94(A4), 3579–3599. Retrieved 2022-12-20, from
1141 <https://onlinelibrary.wiley.com/doi/abs/10.1029/JA094iA04p03579>
1142 (_eprint: <https://onlinelibrary.wiley.com/doi/pdf/10.1029/JA094iA04p03579>)
1143 doi: 10.1029/JA094iA04p03579
- 1144 Korth, A., Friedel, R. H. W., Mouikis, C. G., Fennell, J. F., Wygant, J. R., & Korth,
1145 H. (2000). Comprehensive particle and field observations of magnetic storms
1146 at different local times from the CRRES spacecraft. *Journal of Geophysi-*
1147 *cal Research: Space Physics*, 105(A8), 18729–18740. Retrieved 2023-04-14,
1148 from <https://onlinelibrary.wiley.com/doi/abs/10.1029/1999JA000430>
1149 (_eprint: <https://onlinelibrary.wiley.com/doi/pdf/10.1029/1999JA000430>) doi:
1150 10.1029/1999JA000430
- 1151 Kozyra, J. U., Jordanova, V. K., Borovsky, J. E., Thomsen, M. F., Knipp,
1152 D. J., Evans, D. S., ... Cayton, T. E. (1998). Effects of a high-
1153 density plasma sheet on ring current development during the Novem-
1154 ber 2–6, 1993, magnetic storm. *Journal of Geophysical Research: Space*
1155 *Physics*, 103(A11), 26285–26305. Retrieved 2022-12-08, from [https://](https://onlinelibrary.wiley.com/doi/abs/10.1029/98JA01964)
1156 onlinelibrary.wiley.com/doi/abs/10.1029/98JA01964 (_eprint:
1157 <https://onlinelibrary.wiley.com/doi/pdf/10.1029/98JA01964>) doi: 10.1029/
1158 98JA01964
- 1159 Krimigis, S. M., Gloeckler, G., McEntire, R. W., Potemra, T. A., Scarf, F. L., &
1160 Shelley, E. G. (1985). Magnetic storm of September 4, 1984: A synthesis
1161 of ring current spectra and energy densities measured with AMPTE/CCE.
1162 *Geophysical Research Letters*, 12(5), 329–332. Retrieved 2023-03-06, from

- 1163 <https://onlinelibrary.wiley.com/doi/abs/10.1029/GL012i005p00329>
 1164 (_eprint: <https://onlinelibrary.wiley.com/doi/pdf/10.1029/GL012i005p00329>)
 1165 doi: 10.1029/GL012i005p00329
- 1166 Lemon, C., Wolf, R. A., Hill, T. W., Sazykin, S., Spiro, R. W., Toffoletto, F. R.,
 1167 ... Hesse, M. (2004). Magnetic storm ring current injection modeled
 1168 with the Rice Convection Model and a self-consistent magnetic field. *Geo-*
 1169 *physical Research Letters*, 31(21). Retrieved 2022-12-08, from [https://](https://onlinelibrary.wiley.com/doi/abs/10.1029/2004GL020914)
 1170 onlinelibrary.wiley.com/doi/abs/10.1029/2004GL020914 (_eprint:
 1171 <https://onlinelibrary.wiley.com/doi/pdf/10.1029/2004GL020914>) doi:
 1172 10.1029/2004GL020914
- 1173 Liemohn, M. W. (2003). Yet another caveat to using the Dessler-Parker-
 1174 Skopke relation. *Journal of Geophysical Research: Space Physics*,
 1175 108(A6). Retrieved 2023-01-17, from [https://onlinelibrary](https://onlinelibrary.wiley.com/doi/abs/10.1029/2003JA009839)
 1176 [.wiley.com/doi/abs/10.1029/2003JA009839](https://onlinelibrary.wiley.com/doi/abs/10.1029/2003JA009839) (_eprint:
 1177 <https://onlinelibrary.wiley.com/doi/pdf/10.1029/2003JA009839>) doi:
 1178 10.1029/2003JA009839
- 1179 Liemohn, M. W., & Khazanov, G. V. (2005). Parameterization of Ring
 1180 Current Adiabatic Energization. In *Particle Acceleration in Astro-*
 1181 *physical Plasmas: Geospace and Beyond* (pp. 215–229). American
 1182 Geophysical Union (AGU). Retrieved 2022-12-06, from [https://](https://onlinelibrary.wiley.com/doi/abs/10.1029/156GM24)
 1183 onlinelibrary.wiley.com/doi/abs/10.1029/156GM24 (_eprint:
 1184 <https://onlinelibrary.wiley.com/doi/pdf/10.1029/156GM24>) doi: 10.1029/
 1185 156GM24
- 1186 Lin, D., Sorathia, K., Wang, W., Merkin, V., Bao, S., Pham, K., ... Ander-
 1187 son, B. (2021). The Role of Diffuse Electron Precipitation in the For-
 1188 mation of Subauroral Polarization Streams. *Journal of Geophysical Re-*
 1189 *search: Space Physics*, 126(12), e2021JA029792. Retrieved 2022-05-13,
 1190 from <https://onlinelibrary.wiley.com/doi/abs/10.1029/2021JA029792>
 1191 (_eprint: <https://onlinelibrary.wiley.com/doi/pdf/10.1029/2021JA029792>) doi:
 1192 10.1029/2021JA029792
- 1193 Lindsay, B. G., & Stebbings, R. F. (2005). Charge transfer cross sections for
 1194 energetic neutral atom data analysis. *Journal of Geophysical Research:*
 1195 *Space Physics*, 110(A12). Retrieved 2021-03-30, from [https://agupubs](https://agupubs.onlinelibrary.wiley.com/doi/abs/10.1029/2005JA011298)
 1196 [.onlinelibrary.wiley.com/doi/abs/10.1029/2005JA011298](https://agupubs.onlinelibrary.wiley.com/doi/abs/10.1029/2005JA011298) (_eprint:
 1197 <https://agupubs.onlinelibrary.wiley.com/doi/pdf/10.1029/2005JA011298>) doi:
 1198 <https://doi.org/10.1029/2005JA011298>
- 1199 Liu, J., Angelopoulos, V., Runov, A., & Zhou, X.-Z. (2013). On the cur-
 1200 rent sheets surrounding dipolarizing flux bundles in the magneto-
 1201 tail: The case for wedgelets. *Journal of Geophysical Research: Space*
 1202 *Physics*, 118(5), 2000–2020. Retrieved 2023-01-23, from [https://](https://onlinelibrary.wiley.com/doi/abs/10.1002/jgra.50092)
 1203 onlinelibrary.wiley.com/doi/abs/10.1002/jgra.50092 (_eprint:
 1204 <https://onlinelibrary.wiley.com/doi/pdf/10.1002/jgra.50092>) doi: 10.1002/
 1205 jgra.50092
- 1206 Liu, J., Angelopoulos, V., Zhang, X.-J., Turner, D. L., Gabrielse, C., Runov,
 1207 A., ... Spence, H. E. (2016). Dipolarizing flux bundles in the cis-
 1208 gesynchronous magnetosphere: Relationship between electric fields and
 1209 energetic particle injections. *Journal of Geophysical Research: Space*
 1210 *Physics*, 121(2), 1362–1376. Retrieved 2023-02-03, from [https://](https://onlinelibrary.wiley.com/doi/abs/10.1002/2015JA021691)
 1211 onlinelibrary.wiley.com/doi/abs/10.1002/2015JA021691 (_eprint:
 1212 <https://onlinelibrary.wiley.com/doi/pdf/10.1002/2015JA021691>) doi:
 1213 10.1002/2015JA021691
- 1214 Livadiotis, G., & McComas, D. J. (2013, June). Understanding Kappa Distributions:
 1215 A Toolbox for Space Science and Astrophysics. *Space Science Reviews*, 175(1),
 1216 183–214. Retrieved 2023-01-26, from [https://doi.org/10.1007/s11214-013-](https://doi.org/10.1007/s11214-013-9982-9)
 1217 [9982-9](https://doi.org/10.1007/s11214-013-9982-9) doi: 10.1007/s11214-013-9982-9

- 1218 Lui, A. T. Y. (1993). Radial transport of storm time ring current ions. *Journal of*
 1219 *Geophysical Research: Space Physics*, 98(A1), 209–214. Retrieved 2023-04-
 1220 14, from <https://onlinelibrary.wiley.com/doi/abs/10.1029/92JA02079>
 1221 (_eprint: <https://onlinelibrary.wiley.com/doi/pdf/10.1029/92JA02079>) doi:
 1222 10.1029/92JA02079
- 1223 Lyon, J. G., Fedder, J. A., & Mobarry, C. M. (2004, October). The
 1224 Lyon–Fedder–Mobarry (LFM) global MHD magnetospheric simulation code.
 1225 *Journal of Atmospheric and Solar-Terrestrial Physics*, 66(15), 1333–1350.
 1226 Retrieved 2021-03-17, from [https://www.sciencedirect.com/science/](https://www.sciencedirect.com/science/article/pii/S1364682604001439)
 1227 [article/pii/S1364682604001439](https://www.sciencedirect.com/science/article/pii/S1364682604001439) doi: 10.1016/j.jastp.2004.03.020
- 1228 Lyons, L. R. (1977). Adiabatic evolution of trapped particle pitch angle dis-
 1229 tributions during a storm main phase. *Journal of Geophysical Research*
 1230 (1896-1977), 82(16), 2428–2432. Retrieved 2023-04-14, from [https://](https://onlinelibrary.wiley.com/doi/abs/10.1029/JA082i016p02428)
 1231 onlinelibrary.wiley.com/doi/abs/10.1029/JA082i016p02428 (_eprint:
 1232 <https://onlinelibrary.wiley.com/doi/pdf/10.1029/JA082i016p02428>) doi:
 1233 10.1029/JA082i016p02428
- 1234 Lyons, L. R., Gallardo-Lacourt, B., Zou, S., Weygand, J. M., Nishimura, Y.,
 1235 Li, W., ... Nishitani, N. (2016). The 17 March 2013 storm: Syn-
 1236 ergy of observations related to electric field modes and their ionospheric
 1237 and magnetospheric Effects. *Journal of Geophysical Research: Space*
 1238 *Physics*, 121(11), 10,880–10,897. Retrieved 2022-09-08, from [https://](https://onlinelibrary.wiley.com/doi/abs/10.1002/2016JA023237)
 1239 onlinelibrary.wiley.com/doi/abs/10.1002/2016JA023237 (_eprint:
 1240 <https://onlinelibrary.wiley.com/doi/pdf/10.1002/2016JA023237>) doi:
 1241 10.1002/2016JA023237
- 1242 Lyons, L. R., & Schulz, M. (1989). Access of energetic particles to storm time
 1243 ring current through enhanced radial “diffusion”. *Journal of Geophysical*
 1244 *Research: Space Physics*, 94(A5), 5491–5496. Retrieved 2023-04-14, from
 1245 <https://onlinelibrary.wiley.com/doi/abs/10.1029/JA094iA05p05491>
 1246 (_eprint: <https://onlinelibrary.wiley.com/doi/pdf/10.1029/JA094iA05p05491>)
 1247 doi: 10.1029/JA094iA05p05491
- 1248 Lyons, L. R., & Williams, D. J. (1976). Storm-associated variations
 1249 of equatorially mirroring ring current protons, 1–800 keV, at con-
 1250 stant first adiabatic invariant. *Journal of Geophysical Research*
 1251 (1896-1977), 81(1), 216–220. Retrieved 2023-04-14, from [https://](https://onlinelibrary.wiley.com/doi/abs/10.1029/JA081i001p00216)
 1252 onlinelibrary.wiley.com/doi/abs/10.1029/JA081i001p00216 (_eprint:
 1253 <https://onlinelibrary.wiley.com/doi/pdf/10.1029/JA081i001p00216>) doi:
 1254 10.1029/JA081i001p00216
- 1255 McComas, D. J., Allegrini, F., Baldonado, J., Blake, B., Brandt, P. C., Burch, J.,
 1256 ... Zoennchen, J. (2009, February). The Two Wide-angle Imaging Neutral-
 1257 atom Spectrometers (TWINS) NASA Mission-of-Opportunity. *Space Science*
 1258 *Reviews*, 142(1), 157–231. Retrieved 2023-05-01, from [https://doi.org/](https://doi.org/10.1007/s11214-008-9467-4)
 1259 [10.1007/s11214-008-9467-4](https://doi.org/10.1007/s11214-008-9467-4) doi: 10.1007/s11214-008-9467-4
- 1260 Menz, A. M., Kistler, L. M., Mouikis, C. G., Spence, H. E., Skoug, R. M., Funsten,
 1261 H. O., ... Gkioulidou, M. (2017). The role of convection in the buildup of
 1262 the ring current pressure during the 17 March 2013 storm. *Journal of Geo-*
 1263 *physical Research: Space Physics*, 122(1), 475–492. Retrieved 2022-11-09,
 1264 from <https://onlinelibrary.wiley.com/doi/abs/10.1002/2016JA023358>
 1265 (_eprint: <https://onlinelibrary.wiley.com/doi/pdf/10.1002/2016JA023358>) doi:
 1266 10.1002/2016JA023358
- 1267 Merkin, V. G., & Lyon, J. G. (2010). Effects of the low-latitude ionospheric bound-
 1268 ary condition on the global magnetosphere. *Journal of Geophysical Research:*
 1269 *Space Physics*, 115(A10). Retrieved 2020-03-30, from [https://agupubs](https://agupubs.onlinelibrary.wiley.com/doi/abs/10.1029/2010JA015461)
 1270 [.onlinelibrary.wiley.com/doi/abs/10.1029/2010JA015461](https://agupubs.onlinelibrary.wiley.com/doi/abs/10.1029/2010JA015461) (_eprint:
 1271 <https://agupubs.onlinelibrary.wiley.com/doi/pdf/10.1029/2010JA015461>) doi:
 1272 10.1029/2010JA015461

- 1273 Merkin, V. G., Panov, E. V., Sorathia, K. A., & Ukhorskiy, A. Y. (2019).
 1274 Contribution of Bursty Bulk Flows to the Global Dipolarization of the
 1275 Magnetotail During an Isolated Substorm. *Journal of Geophysical Re-*
 1276 *search: Space Physics*, 124(11), 8647–8668. Retrieved 2022-04-13, from
 1277 <https://onlinelibrary.wiley.com/doi/abs/10.1029/2019JA026872>
 1278 (_eprint: <https://onlinelibrary.wiley.com/doi/pdf/10.1029/2019JA026872>)
 1279 doi: 10.1029/2019JA026872
- 1280 Mitchell, D. G., Lanzerotti, L. J., Kim, C. K., Stokes, M., Ho, G., Cooper, S., ...
 1281 Kerem, S. (2013, November). Radiation Belt Storm Probes Ion Composition
 1282 Experiment (RBSPICE). *Space Science Reviews*, 179(1), 263–308. Retrieved
 1283 2022-05-13, from <https://doi.org/10.1007/s11214-013-9965-x> doi:
 1284 10.1007/s11214-013-9965-x
- 1285 Nakamura, R., Baumjohann, W., Moukikis, C., Kistler, L. M., Runov,
 1286 A., Volwerk, M., ... Balogh, A. (2004). Spatial scale of high-
 1287 speed flows in the plasma sheet observed by Cluster. *Geophysi-*
 1288 *cal Research Letters*, 31(9). Retrieved 2023-01-23, from [https://](https://onlinelibrary.wiley.com/doi/abs/10.1029/2004GL019558)
 1289 onlinelibrary.wiley.com/doi/abs/10.1029/2004GL019558 (_eprint:
 1290 <https://onlinelibrary.wiley.com/doi/pdf/10.1029/2004GL019558>) doi:
 1291 10.1029/2004GL019558
- 1292 Ohtani, S., Singer, H. J., & Mukai, T. (2006). Effects of the fast plasma
 1293 sheet flow on the geosynchronous magnetic configuration: Geotail
 1294 and GOES coordinated study. *Journal of Geophysical Research:*
 1295 *Space Physics*, 111(A1). Retrieved 2022-07-27, from [https://](https://onlinelibrary.wiley.com/doi/abs/10.1029/2005JA011383)
 1296 onlinelibrary.wiley.com/doi/abs/10.1029/2005JA011383 (_eprint:
 1297 <https://onlinelibrary.wiley.com/doi/pdf/10.1029/2005JA011383>) doi:
 1298 10.1029/2005JA011383
- 1299 Panov, E. V., Nakamura, R., Baumjohann, W., Angelopoulos, V., Petrukovich,
 1300 A. A., Retinò, A., ... Larson, D. (2010). Multiple overshoot and rebound of a
 1301 bursty bulk flow. *Geophysical Research Letters*, 37(8). Retrieved 2022-11-28,
 1302 from <https://onlinelibrary.wiley.com/doi/abs/10.1029/2009GL041971>
 1303 (_eprint: <https://onlinelibrary.wiley.com/doi/pdf/10.1029/2009GL041971>) doi:
 1304 10.1029/2009GL041971
- 1305 Pembroke, A., Toffoletto, F., Sazykin, S., Wiltberger, M., Lyon, J., Merkin,
 1306 V., & Schmitt, P. (2012). Initial results from a dynamic coupled
 1307 magnetosphere-ionosphere-ring current model. *Journal of Geophysical Re-*
 1308 *search: Space Physics*, 117(A2). Retrieved 2021-12-21, from [https://](https://onlinelibrary.wiley.com/doi/abs/10.1029/2011JA016979)
 1309 onlinelibrary.wiley.com/doi/abs/10.1029/2011JA016979 (_eprint:
 1310 <https://onlinelibrary.wiley.com/doi/pdf/10.1029/2011JA016979>) doi:
 1311 10.1029/2011JA016979
- 1312 Pontius, D. H., & Wolf, R. A. (1990). Transient flux tubes in the
 1313 terrestrial magnetosphere. *Geophysical Research Letters*, 17(1),
 1314 49–52. Retrieved 2022-09-15, from [https://onlinelibrary](https://onlinelibrary.wiley.com/doi/abs/10.1029/GL017i001p00049)
 1315 [.wiley.com/doi/abs/10.1029/GL017i001p00049](https://onlinelibrary.wiley.com/doi/abs/10.1029/GL017i001p00049) (_eprint:
 1316 <https://onlinelibrary.wiley.com/doi/pdf/10.1029/GL017i001p00049>) doi:
 1317 10.1029/GL017i001p00049
- 1318 Raeder, J., Cramer, W. D., Jensen, J., Fuller-Rowell, T., Maruyama, N., Toffoletto,
 1319 F., & Vo, H. (2016, November). Sub-Auroral Polarization Streams: A complex
 1320 interaction between the magnetosphere, ionosphere, and thermosphere. *Journal*
 1321 *of Physics: Conference Series*, 767(1), 012021. Retrieved 2023-03-01, from
 1322 <https://dx.doi.org/10.1088/1742-6596/767/1/012021> (Publisher: IOP
 1323 Publishing) doi: 10.1088/1742-6596/767/1/012021
- 1324 Roeder, J. L., Fennell, J. F., Chen, M. W., Schulz, M., Grande, M., & Livi, S. (1996,
 1325 January). CRRES observations of the composition of the ring-current ion
 1326 populations. *Advances in Space Research*, 17(10), 17–24. Retrieved 2023-
 1327 03-10, from <https://www.sciencedirect.com/science/article/pii/>

- 1328 027311779500689C doi: 10.1016/0273-1177(95)00689-C
 1329 Roederer, J. G. (1967). On the adiabatic motion of energetic parti-
 1330 cles in a model magnetosphere. *Journal of Geophysical Research*
 1331 (1896-1977), 72(3), 981–992. Retrieved 2023-03-09, from [https://](https://onlinelibrary.wiley.com/doi/abs/10.1029/JZ072i003p00981)
 1332 onlinelibrary.wiley.com/doi/abs/10.1029/JZ072i003p00981 (_eprint:
 1333 <https://onlinelibrary.wiley.com/doi/pdf/10.1029/JZ072i003p00981>) doi:
 1334 10.1029/JZ072i003p00981
- 1335 Rowland, D. E., & Wygant, J. R. (1998). Dependence of the large-scale, inner
 1336 magnetospheric electric field on geomagnetic activity. *Journal of Geophysi-
 1337 cal Research: Space Physics*, 103(A7), 14959–14964. Retrieved 2023-04-21,
 1338 from <https://onlinelibrary.wiley.com/doi/abs/10.1029/97JA03524>
 1339 (_eprint: <https://onlinelibrary.wiley.com/doi/pdf/10.1029/97JA03524>) doi:
 1340 10.1029/97JA03524
- 1341 Runov, A., Angelopoulos, V., Henderson, M. G., Gabrielse, C., & Artemyev,
 1342 A. (2021). Magnetotail Dipolarizations and Ion Flux Variations Dur-
 1343 ing the Main Phase of Magnetic Storms. *Journal of Geophysical Re-
 1344 search: Space Physics*, 126(5), e2020JA028470. Retrieved 2022-08-24, from
 1345 <https://onlinelibrary.wiley.com/doi/abs/10.1029/2020JA028470>
 1346 (_eprint: <https://onlinelibrary.wiley.com/doi/pdf/10.1029/2020JA028470>)
 1347 doi: 10.1029/2020JA028470
- 1348 Runov, A., Angelopoulos, V., Zhou, X.-Z., Zhang, X.-J., Li, S., Plaschke, F.,
 1349 & Bonnell, J. (2011). A THEMIS multicase study of dipolarization
 1350 fronts in the magnetotail plasma sheet. *Journal of Geophysical Re-
 1351 search: Space Physics*, 116(A5). Retrieved 2022-10-27, from [https://](https://onlinelibrary.wiley.com/doi/abs/10.1029/2010JA016316)
 1352 onlinelibrary.wiley.com/doi/abs/10.1029/2010JA016316 (_eprint:
 1353 <https://onlinelibrary.wiley.com/doi/pdf/10.1029/2010JA016316>) doi:
 1354 10.1029/2010JA016316
- 1355 Sciola, A., Merkin, V., Sorathia, K., Gkioulidou, M., Bao, S., Toffoletto, F., ...
 1356 Ukhorskiy, A. (2023). *The contribution of plasma sheet bubbles to stormtime*
 1357 *ring current buildup and evolution of the energy composition*. Retrieved from
 1358 <https://doi.org/10.5281/zenodo.7921979> doi: 10.5281/zenodo.7921979
- 1359 Sckopke, N. (1966). A general relation between the energy of trapped parti-
 1360 cles and the disturbance field near the Earth. *Journal of Geophysical*
 1361 *Research (1896-1977)*, 71(13), 3125–3130. Retrieved 2022-09-15, from
 1362 <https://onlinelibrary.wiley.com/doi/abs/10.1029/JZ071i013p03125>
 1363 (_eprint: <https://onlinelibrary.wiley.com/doi/pdf/10.1029/JZ071i013p03125>)
 1364 doi: 10.1029/JZ071i013p03125
- 1365 Sergeev, V., Yahnin, D., Liou, K., Thomsen, M., & Reeves, G. (2005). Nar-
 1366 row Plasma Streams as a Candidate to Populate the Inner Magneto-
 1367 sphere. In *The Inner Magnetosphere: Physics and Modeling* (pp. 55–
 1368 60). American Geophysical Union (AGU). Retrieved 2023-02-03, from
 1369 <https://onlinelibrary.wiley.com/doi/abs/10.1029/155GM07> (_eprint:
 1370 <https://onlinelibrary.wiley.com/doi/pdf/10.1029/155GM07>) doi: 10.1029/
 1371 155GM07
- 1372 Sheldon, R. B., & Hamilton, D. C. (1993). Ion transport and loss in the Earth’s
 1373 quiet ring current: 1. Data and standard model. *Journal of Geophysi-
 1374 cal Research: Space Physics*, 98(A8), 13491–13508. Retrieved 2023-04-14,
 1375 from <https://onlinelibrary.wiley.com/doi/abs/10.1029/92JA02869>
 1376 (_eprint: <https://onlinelibrary.wiley.com/doi/pdf/10.1029/92JA02869>) doi:
 1377 10.1029/92JA02869
- 1378 Smith, P. H., & Bewtra, N. K. (1978, August). Charge exchange lifetimes for ring
 1379 current ions. *Space Science Reviews*, 22(3), 301–318. Retrieved 2022-12-20,
 1380 from <https://doi.org/10.1007/BF00239804> doi: 10.1007/BF00239804
- 1381 Smith, P. H., & Hoffman, R. A. (1973). Ring current particle distributions dur-
 1382 ing the magnetic storms of December 16–18, 1971. *Journal of Geophysi-*

- 1383 *cal Research (1896-1977)*, 78(22), 4731–4737. Retrieved 2023-03-06, from
 1384 <https://onlinelibrary.wiley.com/doi/abs/10.1029/JA078i022p04731>
 1385 (_eprint: <https://onlinelibrary.wiley.com/doi/pdf/10.1029/JA078i022p04731>)
 1386 doi: 10.1029/JA078i022p04731
- 1387 Sorathia, K. A., Merkin, V. G., Panov, E. V., Zhang, B., Lyon, J. G., Garretson,
 1388 J., ... Wiltberger, M. (2020). Ballooning-Interchange Instability in the
 1389 Near-Earth Plasma Sheet and Auroral Beads: Global Magnetospheric Mod-
 1390 eling at the Limit of the MHD Approximation. *Geophysical Research Let-*
 1391 *ters*, 47(14), e2020GL088227. Retrieved 2021-01-12, from <https://agupubs>
 1392 [.onlinelibrary.wiley.com/doi/abs/10.1029/2020GL088227](https://onlinelibrary.wiley.com/doi/abs/10.1029/2020GL088227) (_eprint:
 1393 <https://agupubs.onlinelibrary.wiley.com/doi/pdf/10.1029/2020GL088227>) doi:
 1394 <https://doi.org/10.1029/2020GL088227>
- 1395 Sorathia, K. A., Michael, A., Merkin, V., Ukhorskiy, A., Turner, D. L., Lyon, J., ...
 1396 Toffoletto, F. (2021). The Role of Mesoscale Plasma Sheet Dynamics in Ring
 1397 Current Formation. *Frontiers in Astronomy and Space Sciences*, 8.
- 1398 Sorathia, K. A., Ukhorskiy, A. Y., Merkin, V. G., Fennell, J. F., & Claude-
 1399 pierre, S. G. (2018). Modeling the Depletion and Recovery of the
 1400 Outer Radiation Belt During a Geomagnetic Storm: Combined MHD
 1401 and Test Particle Simulations. *Journal of Geophysical Research: Space*
 1402 *Physics*, 123(7), 5590–5609. Retrieved 2023-03-09, from <https://>
 1403 onlinelibrary.wiley.com/doi/abs/10.1029/2018JA025506 (_eprint:
 1404 <https://onlinelibrary.wiley.com/doi/pdf/10.1029/2018JA025506>) doi:
 1405 10.1029/2018JA025506
- 1406 Takada, T., Nakamura, R., Baumjohann, W., Asano, Y., Volwerk, M., Zhang,
 1407 T. L., ... Carr, C. (2006). Do BBFs contribute to inner magnetosphere
 1408 dipolarizations: Concurrent Cluster and Double Star observations. *Geo-*
 1409 *physical Research Letters*, 33(21). Retrieved 2023-03-02, from <https://>
 1410 onlinelibrary.wiley.com/doi/abs/10.1029/2006GL027440 (_eprint:
 1411 <https://onlinelibrary.wiley.com/doi/pdf/10.1029/2006GL027440>) doi:
 1412 10.1029/2006GL027440
- 1413 Tang, J., Yao, Y., Kong, J., & Zhang, L. (2016, July). Large-scale traveling iono-
 1414 spheric disturbances using ionospheric imaging at storm time: A case study
 1415 on 17 march 2013. *Journal of Atmospheric and Solar-Terrestrial Physics*,
 1416 145, 12–20. Retrieved 2023-03-01, from [https://www.sciencedirect.com/](https://www.sciencedirect.com/science/article/pii/S1364682616301006)
 1417 [science/article/pii/S1364682616301006](https://www.sciencedirect.com/science/article/pii/S1364682616301006) doi: 10.1016/j.jastp.2016.04.006
- 1418 Toffoletto, F., Sazykin, S., Spiro, R., & Wolf, R. (2003, April). Inner magneto-
 1419 spheric modeling with the Rice Convection Model. *Space Science Reviews*,
 1420 107(1), 175–196. Retrieved 2020-08-19, from [https://doi.org/10.1023/A:](https://doi.org/10.1023/A:1025532008047)
 1421 1025532008047 doi: 10.1023/A:1025532008047
- 1422 Tsyganenko, N. A., & Mukai, T. (2003). Tail plasma sheet models de-
 1423 rived from Geotail particle data. *Journal of Geophysical Research:*
 1424 *Space Physics*, 108(A3). Retrieved 2023-01-26, from <https://>
 1425 onlinelibrary.wiley.com/doi/abs/10.1029/2002JA009707 (_eprint:
 1426 <https://onlinelibrary.wiley.com/doi/pdf/10.1029/2002JA009707>) doi:
 1427 10.1029/2002JA009707
- 1428 Turner, D. L., Fennell, J. F., Blake, J. B., Claudepierre, S. G., Clemmons, J. H.,
 1429 Jaynes, A. N., ... Reeves, G. D. (2017). Multipoint Observations of Ener-
 1430 getic Particle Injections and Substorm Activity During a Conjunction Between
 1431 Magnetospheric Multiscale (MMS) and Van Allen Probes. *Journal of Geophys-*
 1432 *ical Research: Space Physics*, 122(11), 11,481–11,504. Retrieved 2022-07-28,
 1433 from <https://onlinelibrary.wiley.com/doi/abs/10.1002/2017JA024554>
 1434 (_eprint: <https://onlinelibrary.wiley.com/doi/pdf/10.1002/2017JA024554>) doi:
 1435 10.1002/2017JA024554
- 1436 Turner, N. E., Baker, D. N., Pulkkinen, T. I., Roeder, J. L., Fennell, J. F.,
 1437 & Jordanova, V. K. (2001). Energy content in the storm time

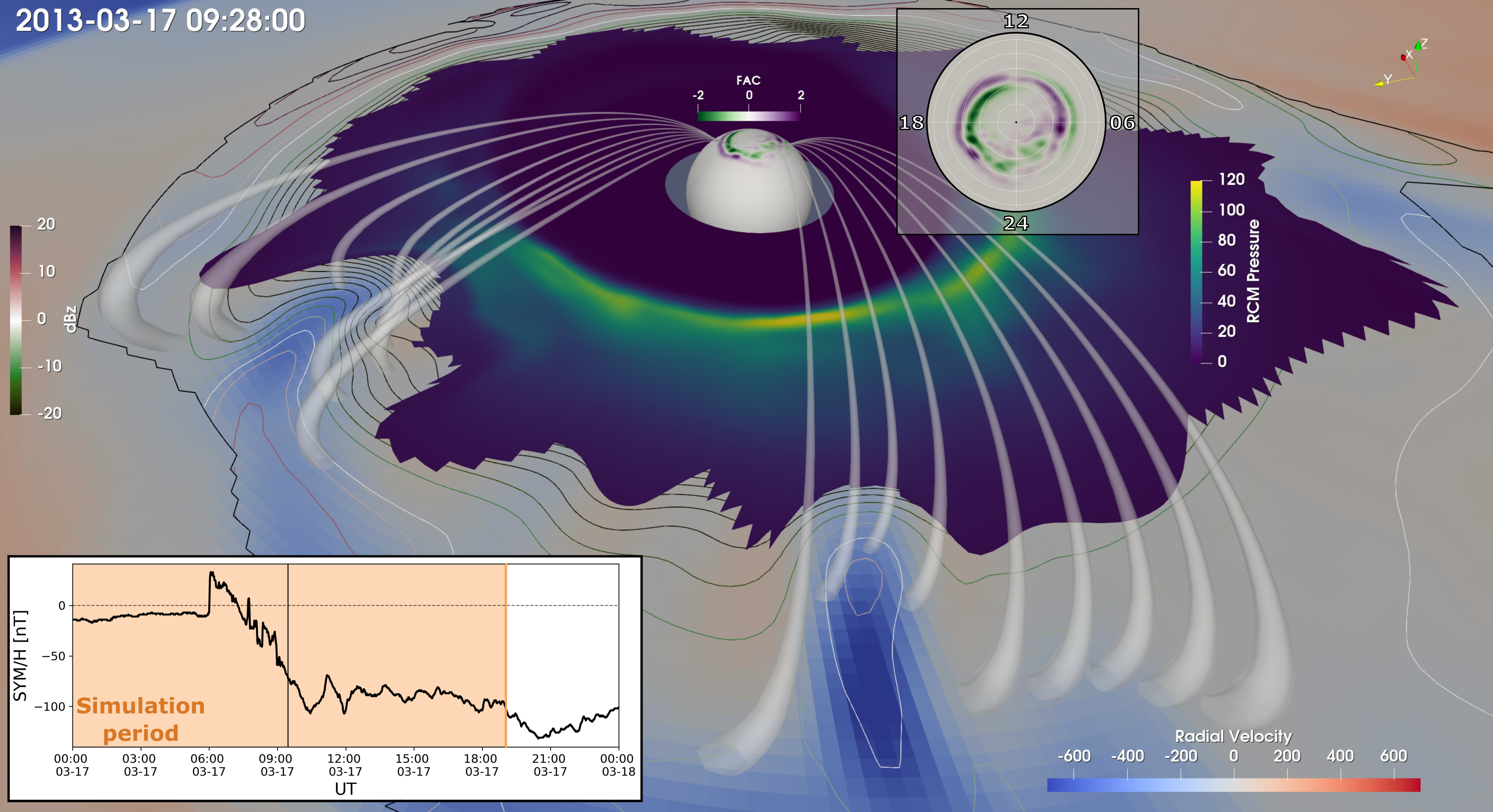
- ring current. *Journal of Geophysical Research: Space Physics*,
 106(A9), 19149–19156. Retrieved 2022-12-01, from [https://
 onlinelibrary.wiley.com/doi/abs/10.1029/2000JA003025](https://onlinelibrary.wiley.com/doi/abs/10.1029/2000JA003025) (_eprint:
<https://onlinelibrary.wiley.com/doi/pdf/10.1029/2000JA003025>) doi:
 10.1029/2000JA003025
- Ukhorskiy, A. Y., Sorathia, K. A., Merkin, V. G., Sitnov, M. I., Mitchell, D. G.,
 & Gkioulidou, M. (2018). Ion Trapping and Acceleration at Dipolarization
 Fronts: High-Resolution MHD and Test-Particle Simulations. *Journal of Geo-
 physical Research: Space Physics*, 123(7), 5580–5589. Retrieved 2022-12-20,
 from <https://onlinelibrary.wiley.com/doi/abs/10.1029/2018JA025370>
 (_eprint: <https://onlinelibrary.wiley.com/doi/pdf/10.1029/2018JA025370>) doi:
 10.1029/2018JA025370
- Varney, R. H., Wiltberger, M., Zhang, B., Lotko, W., & Lyon, J. (2016). Influ-
 ence of ion outflow in coupled geospace simulations: 1. Physics-based ion
 outflow model development and sensitivity study. *Journal of Geophysical
 Research: Space Physics*, 121(10), 9671–9687. Retrieved 2023-03-14, from
<https://onlinelibrary.wiley.com/doi/abs/10.1002/2016JA022777>
 (_eprint: <https://onlinelibrary.wiley.com/doi/pdf/10.1002/2016JA022777>) doi:
 10.1002/2016JA022777
- Vasyliunas, V. M. (1970). Mathematical Models of Magnetospheric Convection and
 its Coupling to the Ionosphere. In B. M. McCormac (Ed.), *Particles and Fields
 in the Magnetosphere* (pp. 60–71). Dordrecht: Springer Netherlands. doi: 10
 .1007/978-94-010-3284-1_6
- Welling, D. T., Jordanova, V. K., Zaharia, S. G., Glocer, A., & Toth, G. (2011).
 The effects of dynamic ionospheric outflow on the ring current. *Journal
 of Geophysical Research: Space Physics*, 116(A2). Retrieved 2023-05-03,
 from <https://onlinelibrary.wiley.com/doi/abs/10.1029/2010JA015642>
 (_eprint: <https://onlinelibrary.wiley.com/doi/pdf/10.1029/2010JA015642>) doi:
 10.1029/2010JA015642
- Williams, D. J. (1985, December). Dynamics of the earth’s ring current: Theory and
 observation. *Space Science Reviews*, 42(3), 375–396. Retrieved 2023-02-15,
 from <https://doi.org/10.1007/BF00214994> doi: 10.1007/BF00214994
- Wiltberger, M., Merkin, V., Lyon, J. G., & Ohtani, S. (2015). High-resolution
 global magnetohydrodynamic simulation of bursty bulk flows. *Journal of Geo-
 physical Research: Space Physics*, 120(6), 4555–4566. Retrieved 2022-08-01,
 from <https://onlinelibrary.wiley.com/doi/abs/10.1002/2015JA021080>
 (_eprint: <https://onlinelibrary.wiley.com/doi/pdf/10.1002/2015JA021080>) doi:
 10.1002/2015JA021080
- Wiltberger, M., Merkin, V., Zhang, B., Toffoletto, F., Oppenheim, M.,
 Wang, W., ... Stephens, G. K. (2017). Effects of electrojet tur-
 bulence on a magnetosphere-ionosphere simulation of a geomag-
 netic storm. *Journal of Geophysical Research: Space Physics*,
 122(5), 5008–5027. Retrieved 2021-01-25, from [https://agupubs
 .onlinelibrary.wiley.com/doi/abs/10.1002/2016JA023700](https://agupubs.onlinelibrary.wiley.com/doi/abs/10.1002/2016JA023700) (_eprint:
<https://agupubs.onlinelibrary.wiley.com/doi/pdf/10.1002/2016JA023700>) doi:
<https://doi.org/10.1002/2016JA023700>
- Wing, S., Johnson, J. R., Chaston, C. C., Echim, M., Escoubet, C. P., Lavraud, B.,
 ... Wang, C.-P. (2014, November). Review of Solar Wind Entry into and
 Transport Within the Plasma Sheet. *Space Science Reviews*, 184(1), 33–86.
 Retrieved 2023-03-11, from <https://doi.org/10.1007/s11214-014-0108-9>
 doi: 10.1007/s11214-014-0108-9
- Wolf, R. A., Spiro, R. W., Sazykin, S., Toffoletto, F. R., & Yang, J. (2016). Forty-
 Seven Years of the Rice Convection Model. In *Magnetosphere-Ionosphere
 Coupling in the Solar System* (pp. 215–225). American Geophysical Union
 (AGU). Retrieved 2020-09-17, from <https://agupubs.onlinelibrary>

- 1493 .wiley.com/doi/abs/10.1002/9781119066880.ch17 (Section: 17 _eprint:
1494 <https://agupubs.onlinelibrary.wiley.com/doi/pdf/10.1002/9781119066880.ch17>)
1495 doi: 10.1002/9781119066880.ch17
- 1496 Wolf, R. A., Wan, Y., Xing, X., Zhang, J.-C., & Sazykin, S. (2009). En-
1497 tropy and plasma sheet transport. *Journal of Geophysical Research:*
1498 *Space Physics*, 114(A9). Retrieved 2022-10-26, from [https://](https://onlinelibrary.wiley.com/doi/abs/10.1029/2009JA014044)
1499 onlinelibrary.wiley.com/doi/abs/10.1029/2009JA014044 (_eprint:
1500 <https://onlinelibrary.wiley.com/doi/pdf/10.1029/2009JA014044>) doi:
1501 10.1029/2009JA014044
- 1502 Yang, J., Toffoletto, F. R., & Wolf, R. A. (2016). Comparison study of ring cur-
1503 rent simulations with and without bubble injections. *Journal of Geophysi-*
1504 *cal Research: Space Physics*, 121(1), 374–379. Retrieved 2022-12-06, from
1505 <https://onlinelibrary.wiley.com/doi/abs/10.1002/2015JA021901>
1506 (_eprint: <https://onlinelibrary.wiley.com/doi/pdf/10.1002/2015JA021901>)
1507 doi: 10.1002/2015JA021901
- 1508 Yang, J., Toffoletto, F. R., Wolf, R. A., & Sazykin, S. (2015). On the contribution
1509 of plasma sheet bubbles to the storm time ring current. *Journal of Geo-*
1510 *physical Research: Space Physics*, 120(9), 7416–7432. Retrieved 2022-09-28,
1511 from <https://onlinelibrary.wiley.com/doi/abs/10.1002/2015JA021398>
1512 (_eprint: <https://onlinelibrary.wiley.com/doi/pdf/10.1002/2015JA021398>) doi:
1513 10.1002/2015JA021398
- 1514 Yang, J., Wolf, R., Toffoletto, F., Sazykin, S., Wang, W., & Cui, J. (2019).
1515 The Inertialized Rice Convection Model. *Journal of Geophysical Re-*
1516 *search: Space Physics*, 124(12), 10294–10317. Retrieved 2023-04-11, from
1517 <https://onlinelibrary.wiley.com/doi/abs/10.1029/2019JA026811>
1518 (_eprint: <https://onlinelibrary.wiley.com/doi/pdf/10.1029/2019JA026811>)
1519 doi: 10.1029/2019JA026811
- 1520 Yu, Y., Jordanova, V., Welling, D., Larsen, B., Claudepierre, S. G., & Kletzing,
1521 C. (2014). The role of ring current particle injections: Global simulations
1522 and Van Allen Probes observations during 17 March 2013 storm. *Geo-*
1523 *physical Research Letters*, 41(4), 1126–1132. Retrieved 2023-03-01, from
1524 <https://onlinelibrary.wiley.com/doi/abs/10.1002/2014GL059322>
1525 (_eprint: <https://onlinelibrary.wiley.com/doi/pdf/10.1002/2014GL059322>)
1526 doi: 10.1002/2014GL059322
- 1527 Yu, Y., Jordanova, V., Zou, S., Heelis, R., Ruohoniemi, M., & Wygant,
1528 J. (2015). Modeling subauroral polarization streams during the
1529 17 March 2013 storm. *Journal of Geophysical Research: Space*
1530 *Physics*, 120(3), 1738–1750. Retrieved 2023-03-01, from [https://](https://onlinelibrary.wiley.com/doi/abs/10.1002/2014JA020371)
1531 onlinelibrary.wiley.com/doi/abs/10.1002/2014JA020371 (_eprint:
1532 <https://onlinelibrary.wiley.com/doi/pdf/10.1002/2014JA020371>) doi:
1533 10.1002/2014JA020371
- 1534 Yue, X., Wan, W., Liu, L., Liu, J., Zhang, S., Schreiner, W. S., ... Hu, L. (2016).
1535 Mapping the conjugate and corotating storm-enhanced density during 17
1536 March 2013 storm through data assimilation. *Journal of Geophysical Re-*
1537 *search: Space Physics*, 121(12), 12,202–12,210. Retrieved 2023-03-01, from
1538 <https://onlinelibrary.wiley.com/doi/abs/10.1002/2016JA023038>
1539 (_eprint: <https://onlinelibrary.wiley.com/doi/pdf/10.1002/2016JA023038>)
1540 doi: 10.1002/2016JA023038
- 1541 Zhang, B., Sorathia, K. A., Lyon, J. G., Merkin, V. G., Garretson, J. S., & Wilt-
1542 berger, M. (2019, September). GAMERA: A three-dimensional finite-
1543 volume MHD solver for non-orthogonal curvilinear geometries. *The As-*
1544 *trophysical Journal Supplement Series*, 244(1), 20. Retrieved 2020-03-
1545 25, from <http://arxiv.org/abs/1810.10861> (arXiv: 1810.10861) doi:
1546 10.3847/1538-4365/ab3a4c
- 1547 Zhao, H., Li, X., Baker, D. N., Fennell, J. F., Blake, J. B., Larsen, B. A., ...

- 1548 Rodriguez, J. V. (2015). The evolution of ring current ion energy
1549 density and energy content during geomagnetic storms based on Van
1550 Allen Probes measurements. *Journal of Geophysical Research: Space*
1551 *Physics*, 120(9), 7493–7511. Retrieved 2021-10-18, from [https://](https://onlinelibrary.wiley.com/doi/abs/10.1002/2015JA021533)
1552 onlinelibrary.wiley.com/doi/abs/10.1002/2015JA021533 (_eprint:
1553 <https://onlinelibrary.wiley.com/doi/pdf/10.1002/2015JA021533>) doi:
1554 10.1002/2015JA021533
- 1555 Østgaard, N., Mende, S. B., Frey, H. U., Gladstone, G. R., & Lauche,
1556 H. (2003). Neutral hydrogen density profiles derived from
1557 geocoronal imaging. *Journal of Geophysical Research: Space*
1558 *Physics*, 108(A7). Retrieved 2021-03-30, from [https://agupubs](https://agupubs.onlinelibrary.wiley.com/doi/abs/10.1029/2002JA009749)
1559 [.onlinelibrary.wiley.com/doi/abs/10.1029/2002JA009749](https://agupubs.onlinelibrary.wiley.com/doi/abs/10.1029/2002JA009749) (_eprint:
1560 <https://agupubs.onlinelibrary.wiley.com/doi/pdf/10.1029/2002JA009749>) doi:
1561 <https://doi.org/10.1029/2002JA009749>

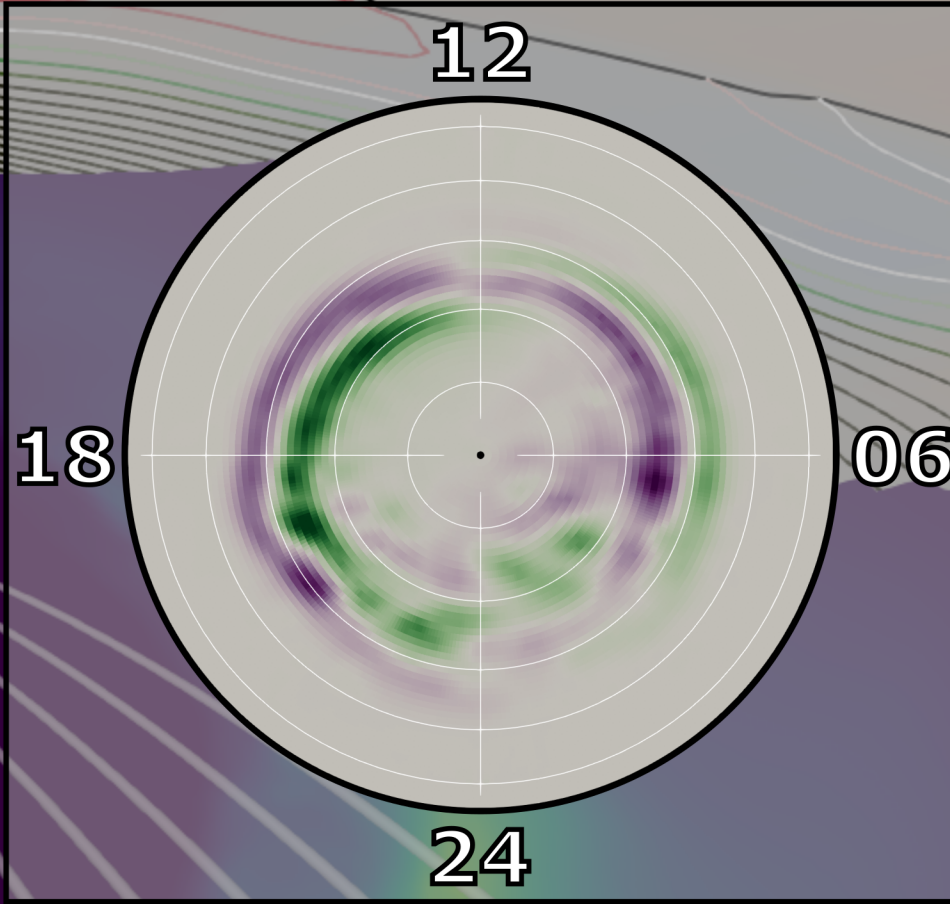
Figure 1.

2013-03-17 09:28:00



20
10
0
dBz
-10
-20

FAC
-2 0 2



120
100
80
60
RCM Pressure
40
20
0

Radial Velocity
-600 -400 -200 0 200 400 600

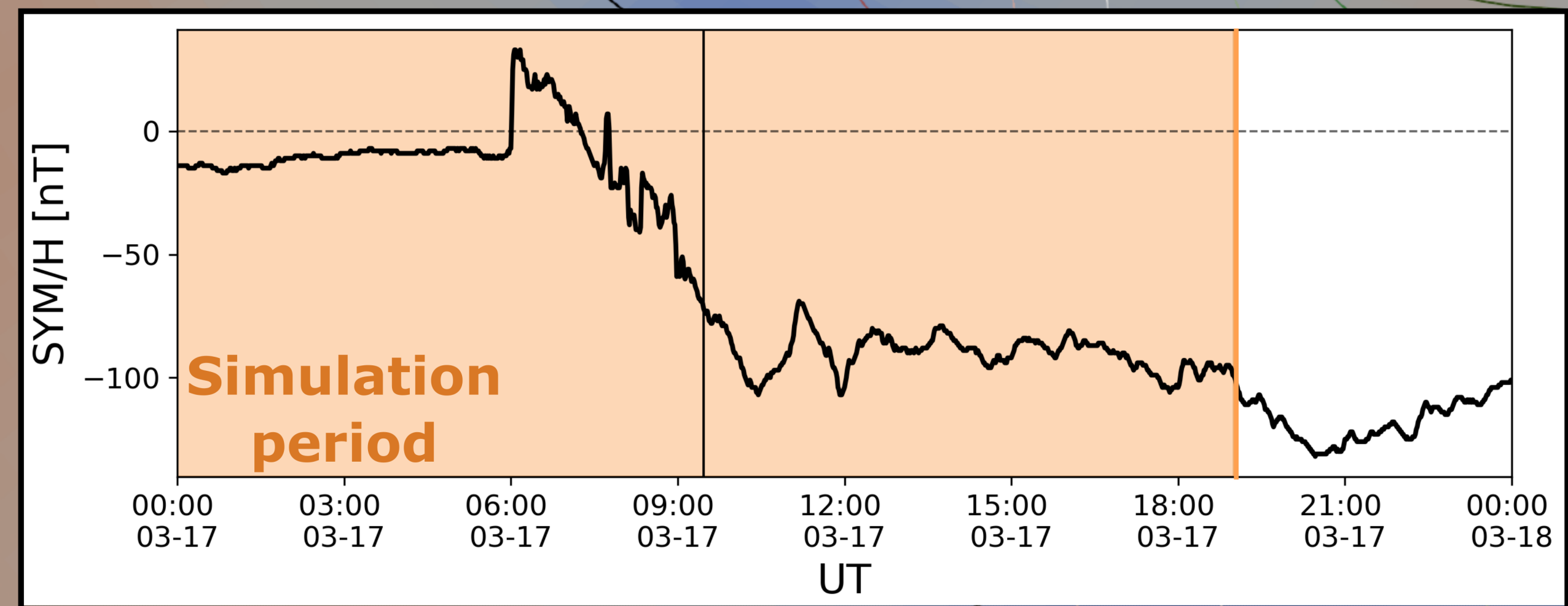


Figure 2.

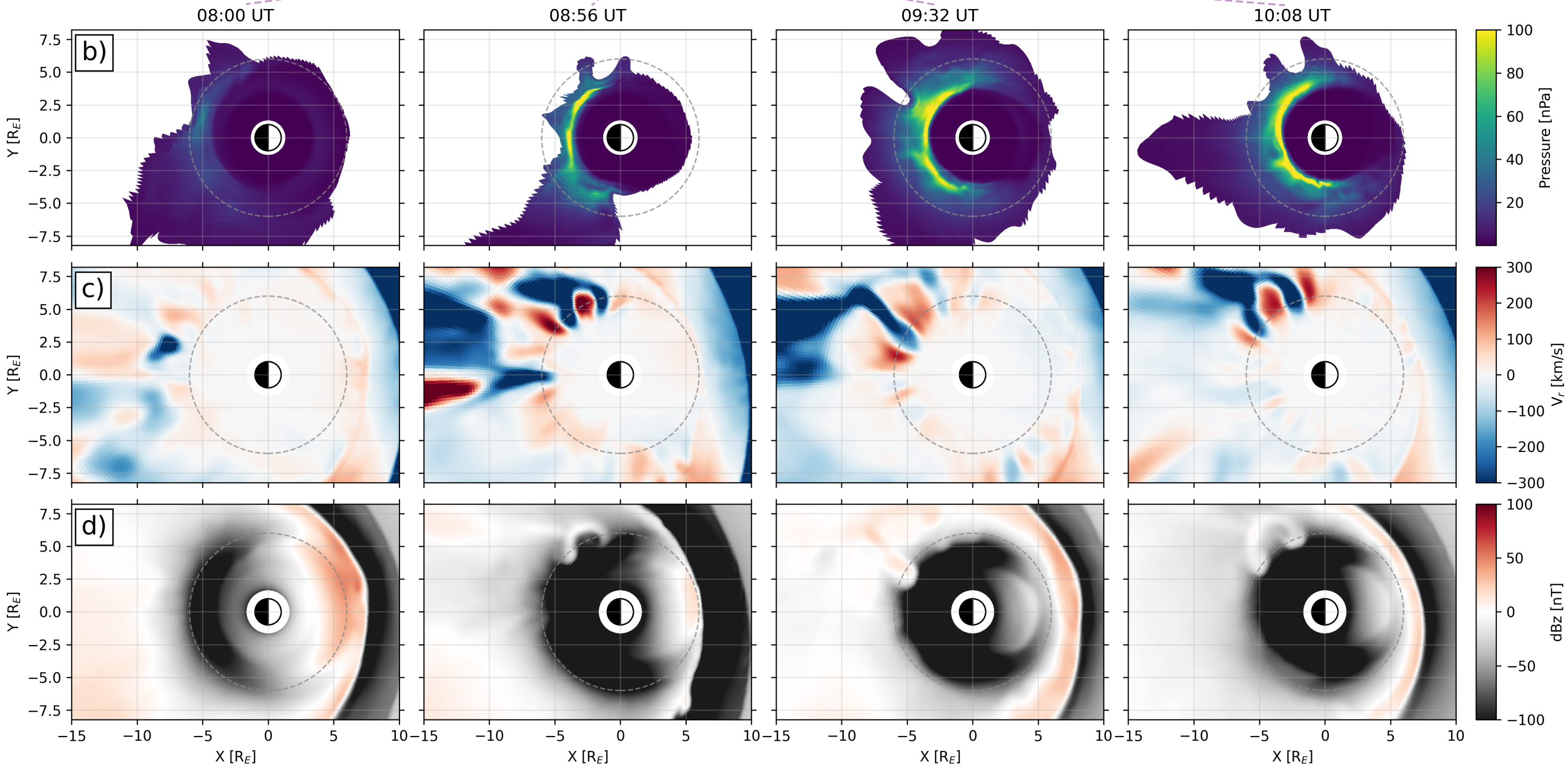
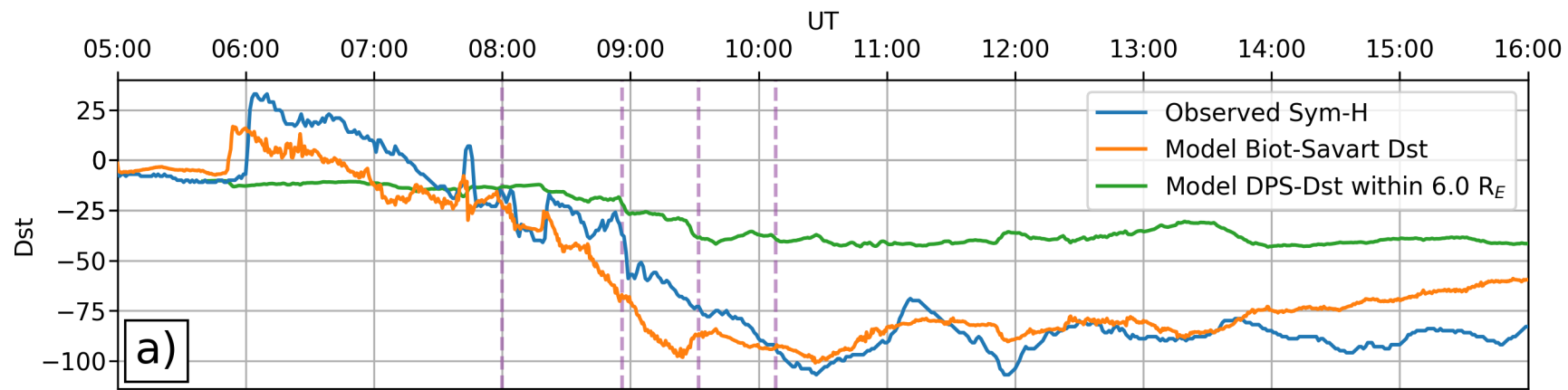


Figure 3.

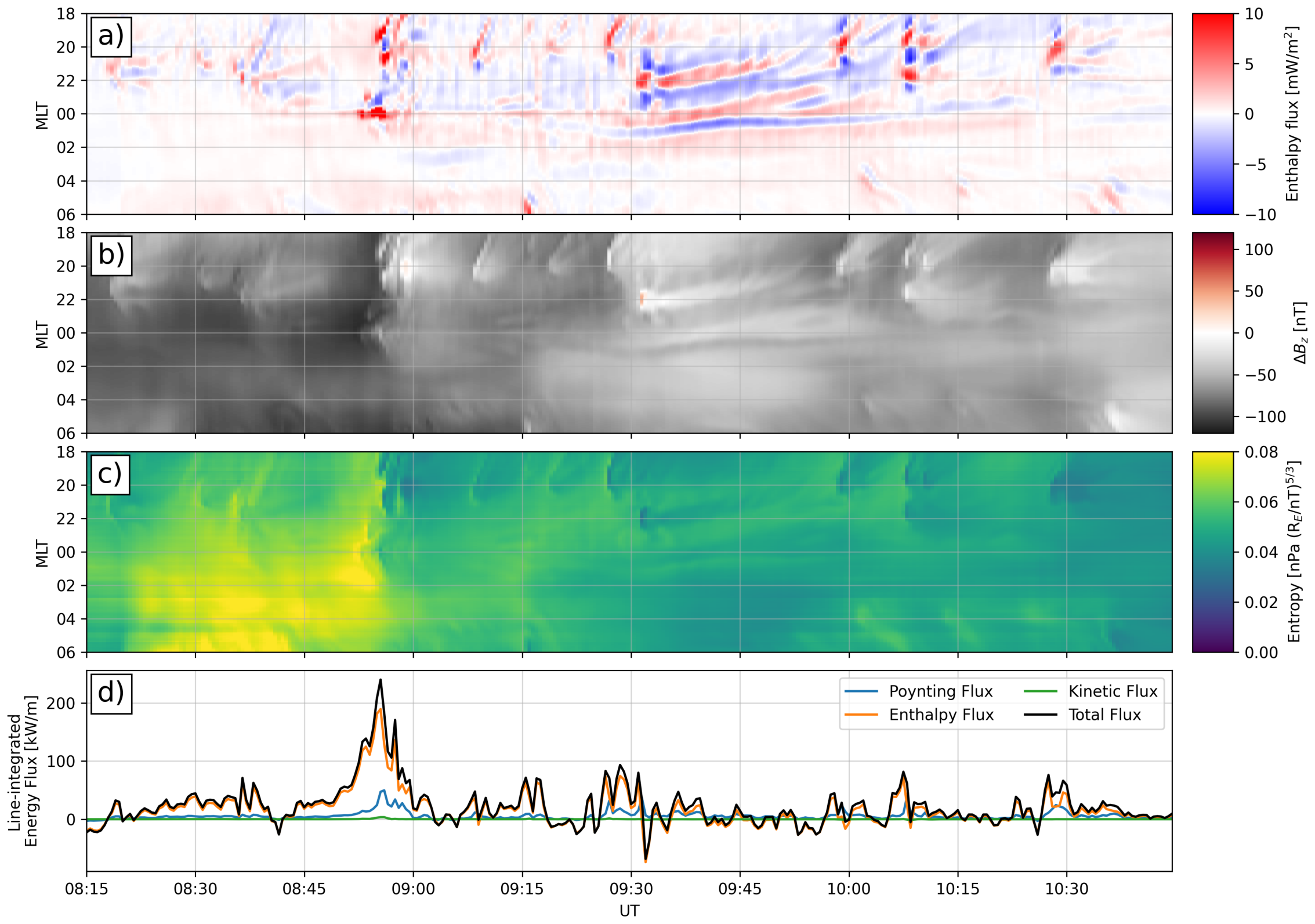


Figure 4.

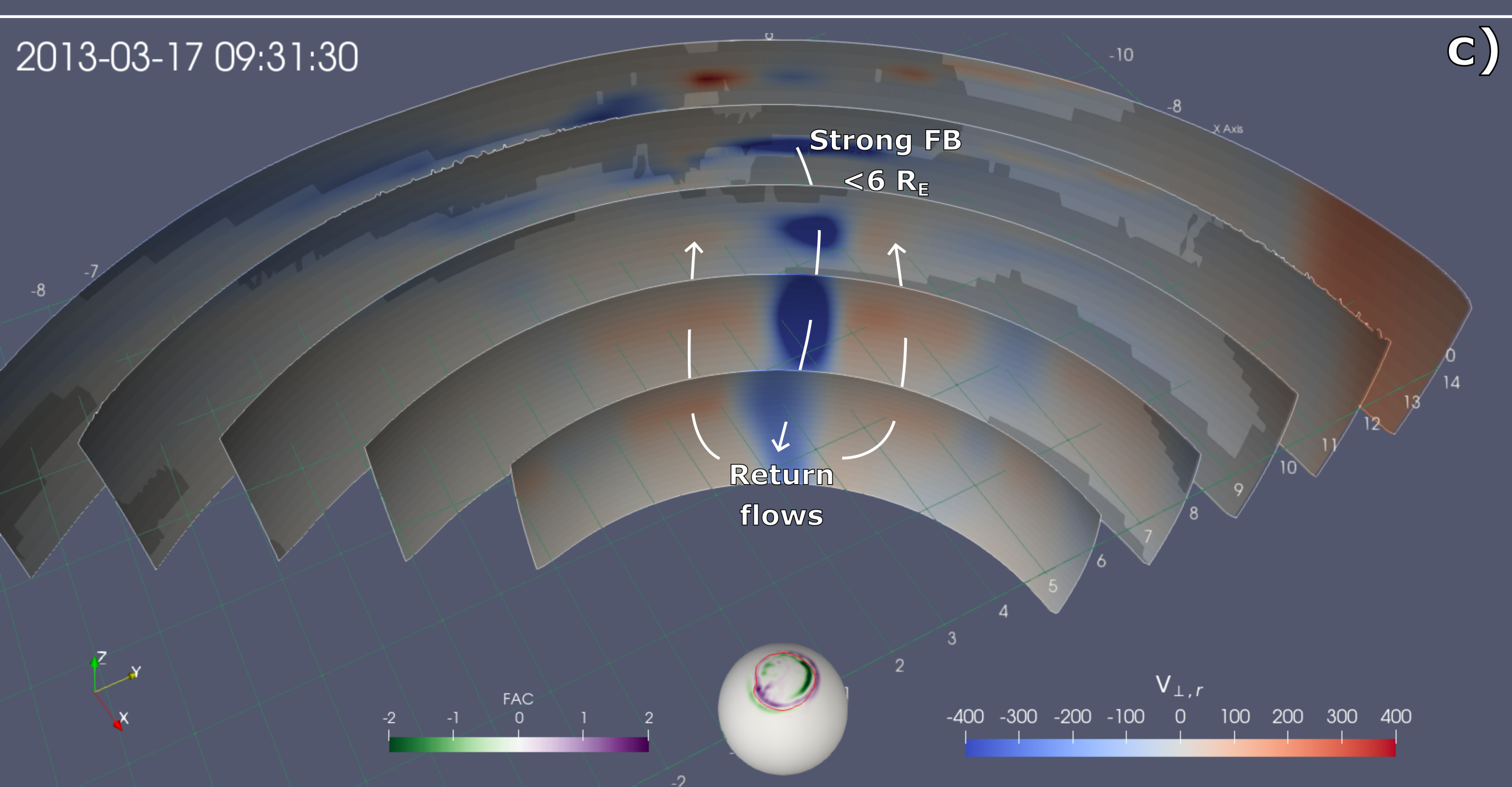
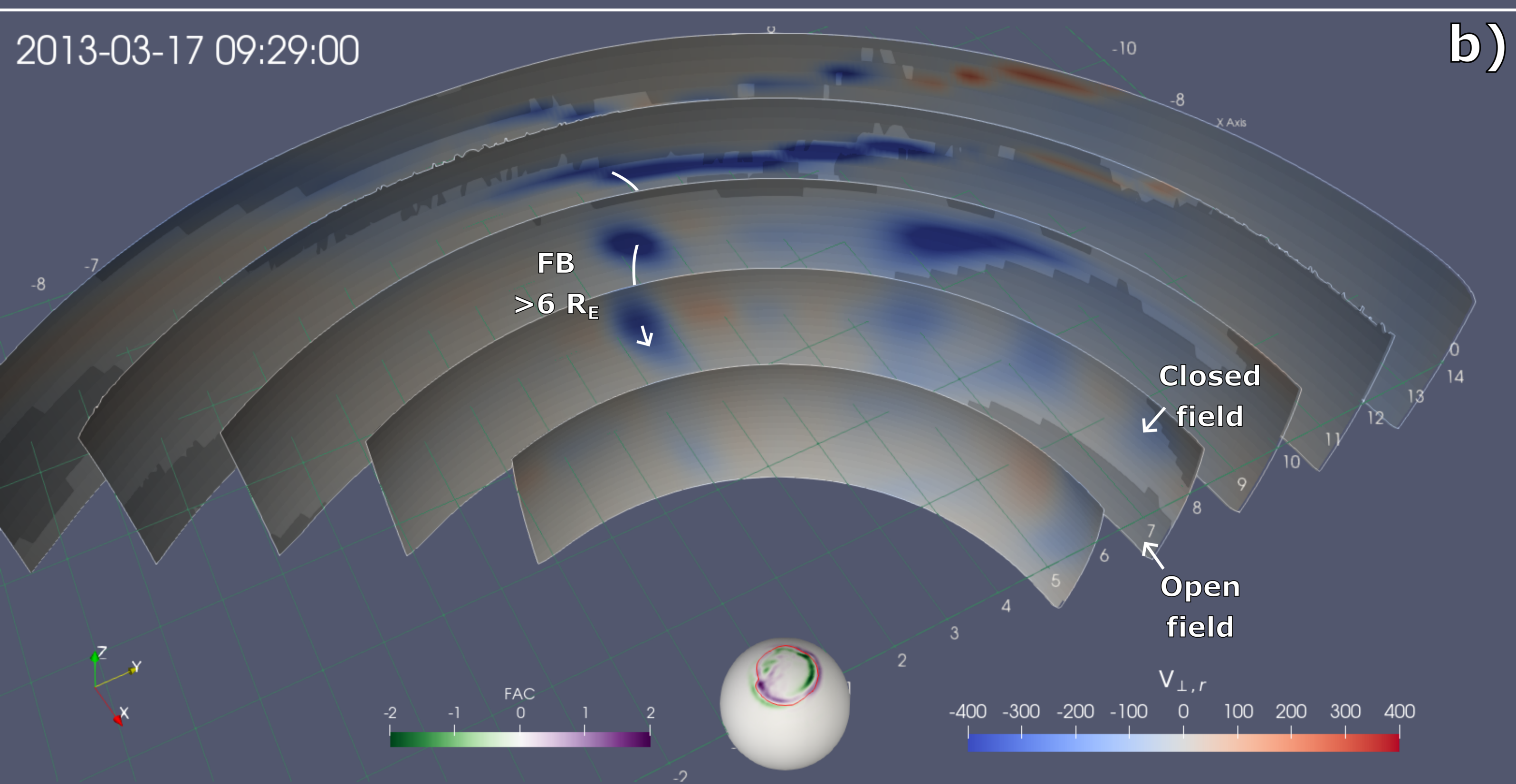
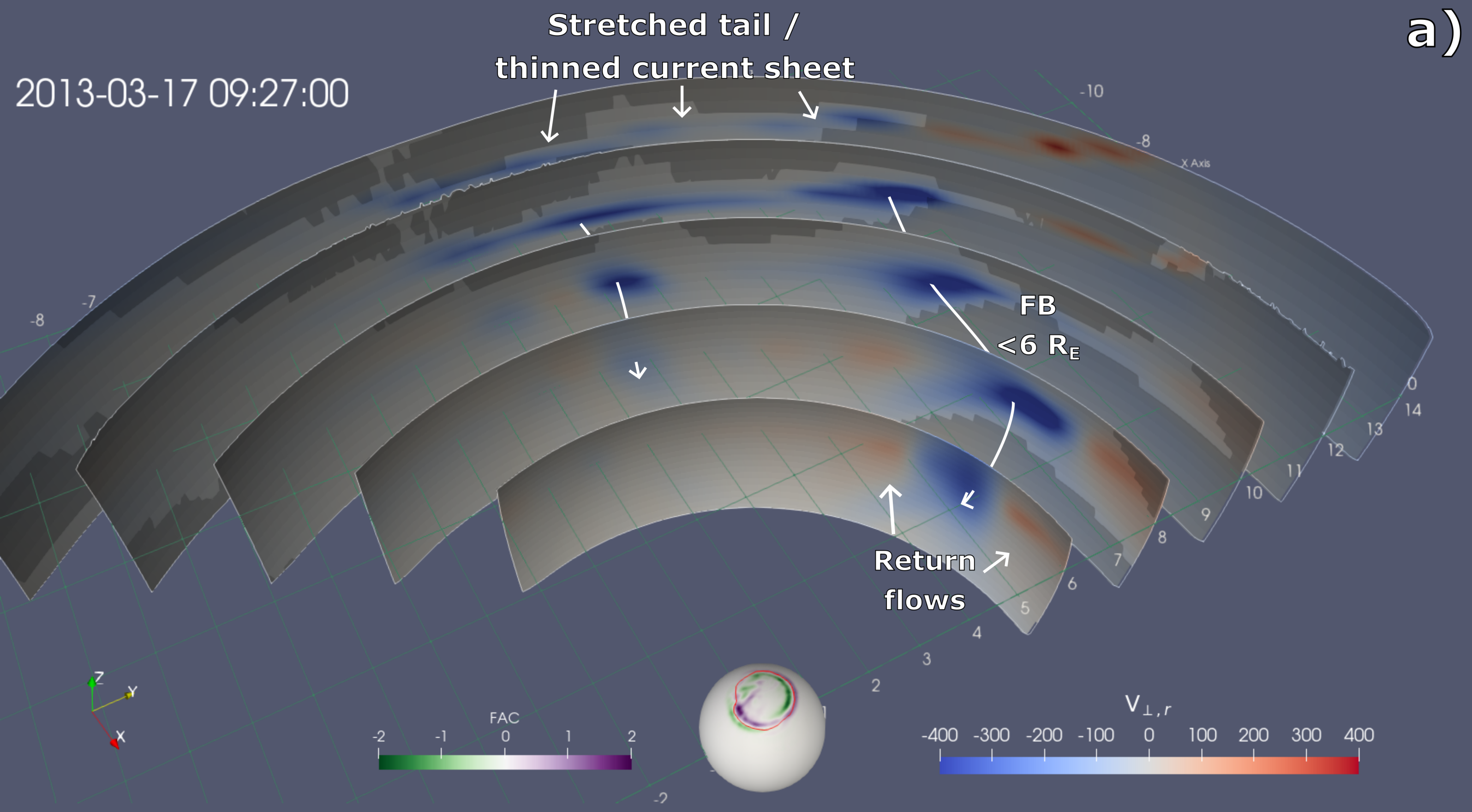


Figure 5.

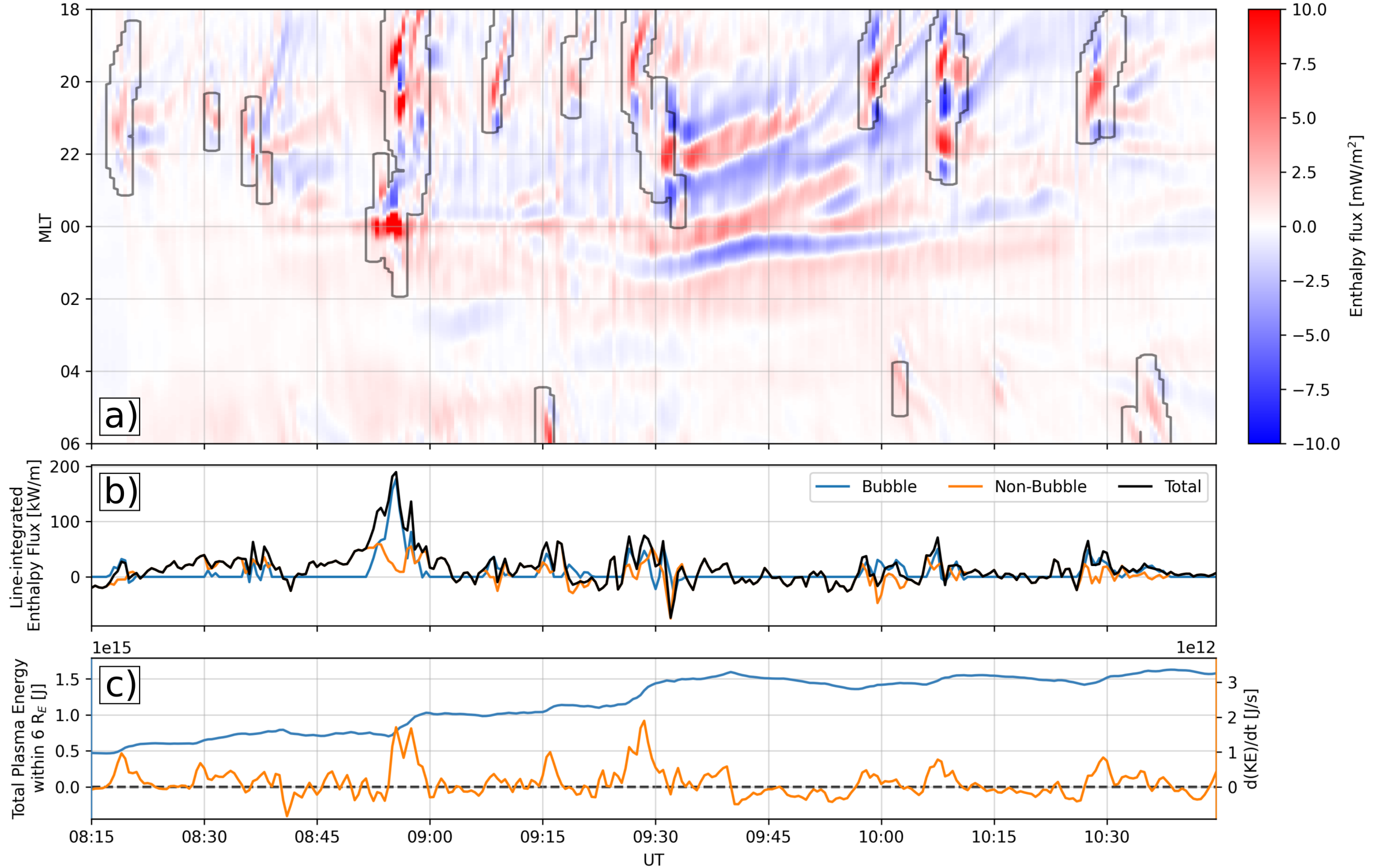


Figure 6.

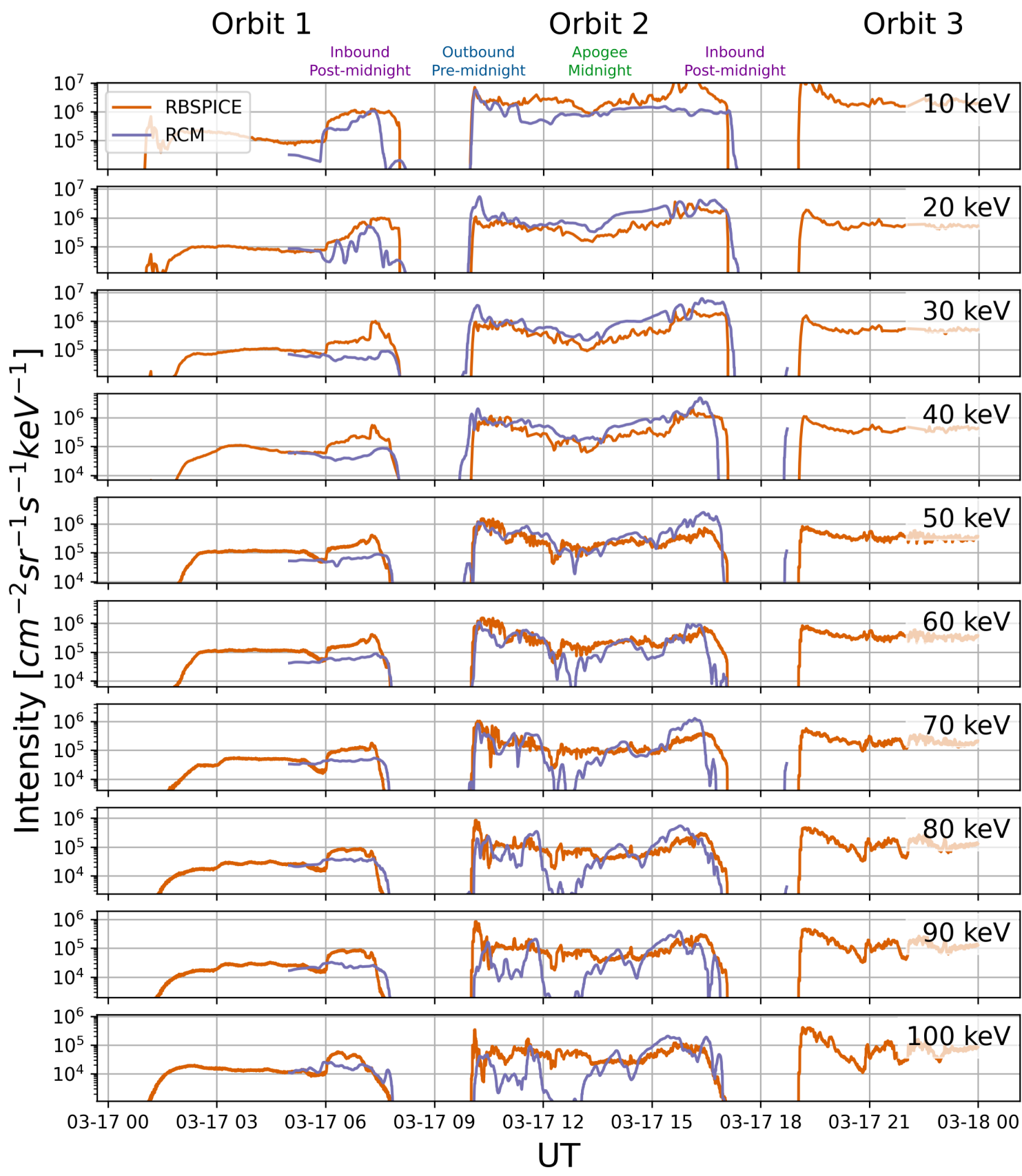


Figure 7.

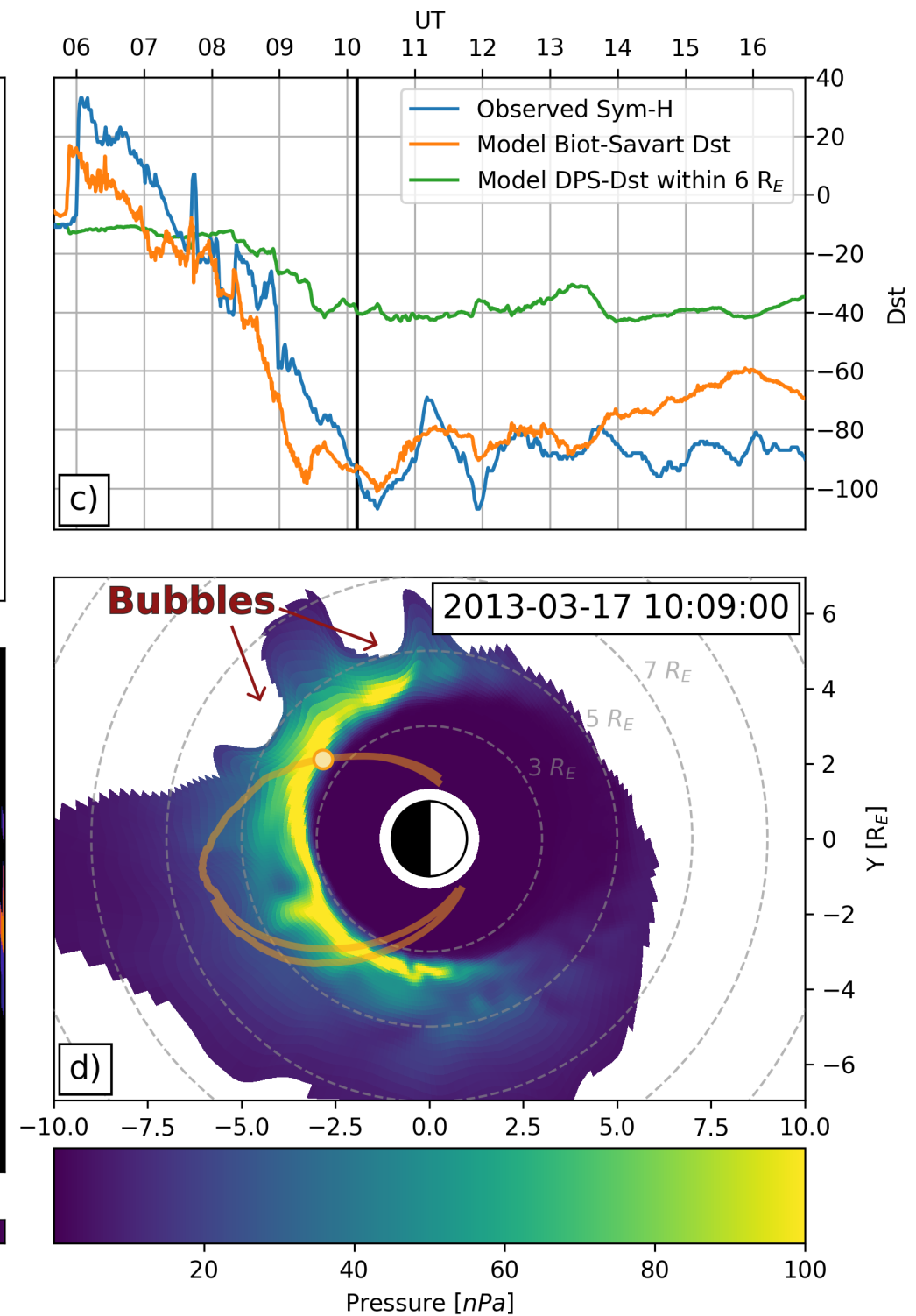
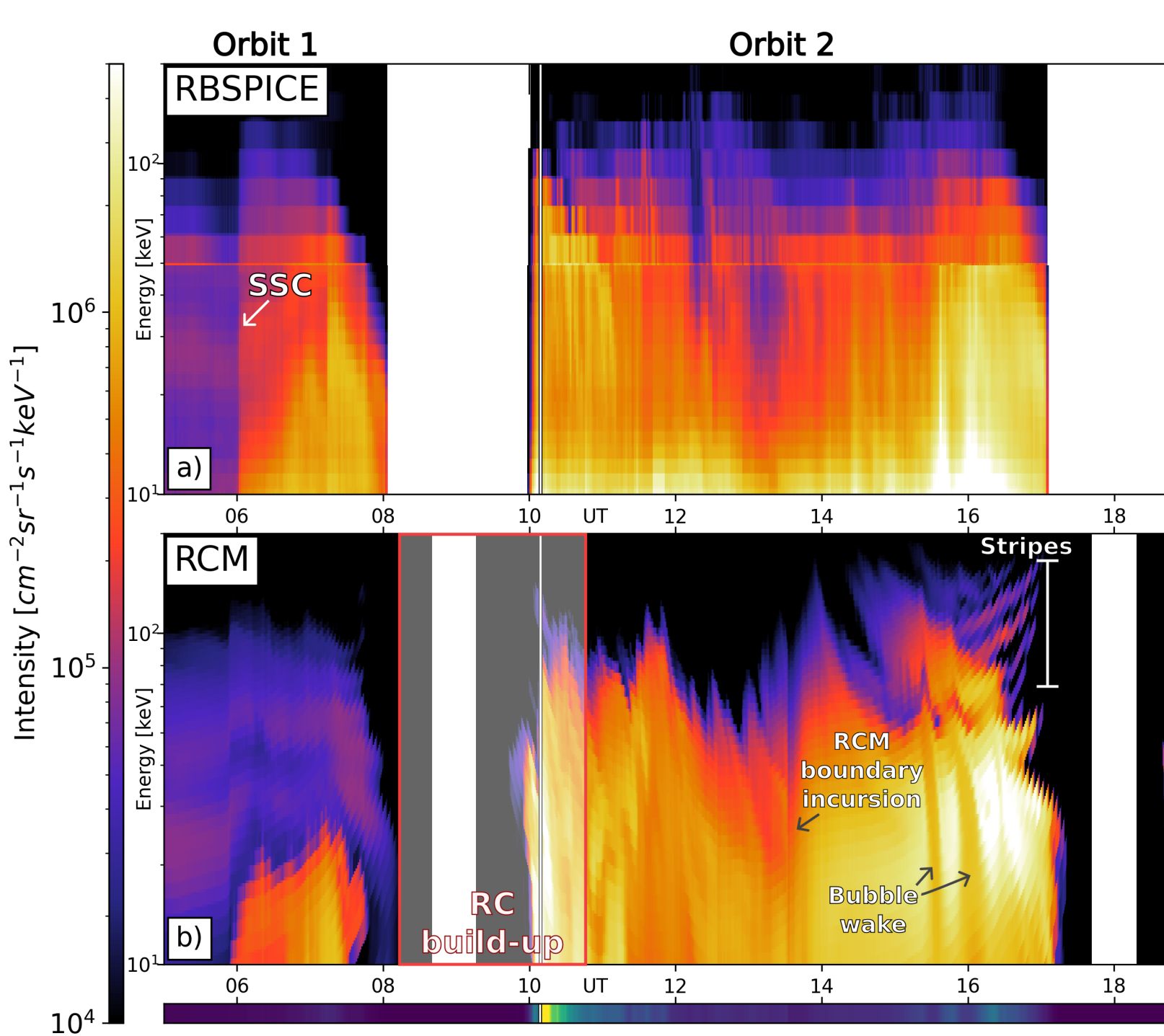


Figure 8.

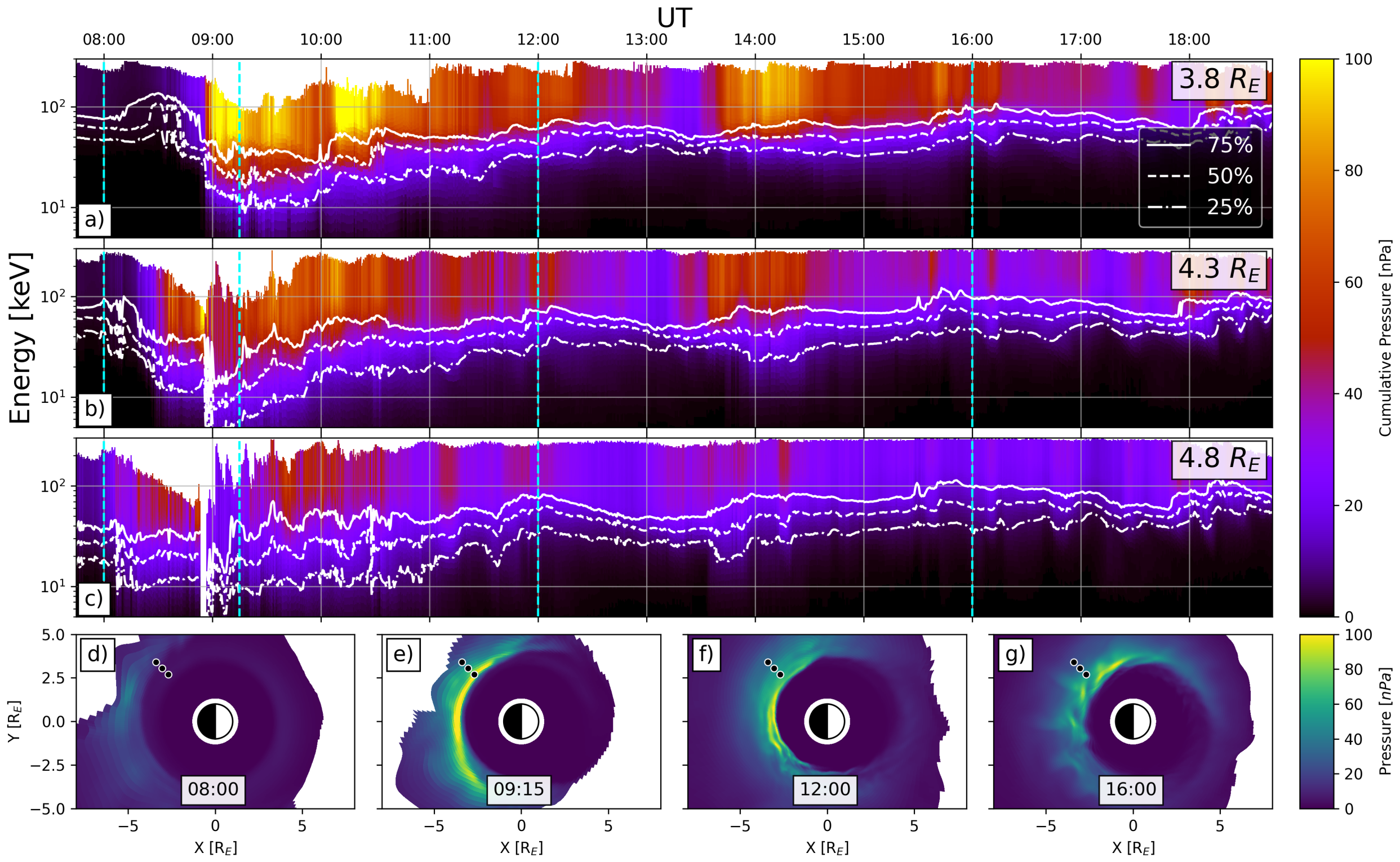


Figure 9.

